Single ion - single photon interactions in free space

Dissertation

zur Erlangung des Doktorgrades an der
Fakultät für Mathematik, Informatik und Physik
der Leopold-Franzens-Universität Innsbruck

vorgelegt von

Lukáš Slodička

durchgeführt am Institut für Experimentalphysik
unter der Leitung von
Univ.-Prof. Dr. Rainer Blatt

Mai 2013

Abstract

Trapped ion crystals have proved to be one of the most viable physical implementations of quantum bits due to the excellent possibilities to control their motion, achieve long coherence times between internal levels, and efficiently couple the electronic states of ions through their common motion. These properties make trapped ion systems very good candidates for a scalable realization of quantum networks. However, such a realization would require the development of an efficient interface between trapped ions and photons.

This thesis reports on the realization of atom-light coupling schemes in free space. Using the system of a single or two trapped $^{138}Ba^{+}$ ions in the focus of a high numerical aperture lens, we study two possible approaches to the distribution of quantum information based on deterministic and probabilistic interactions between single atoms and light fields.

We realize an absorption spectroscopy experiment and demonstrate the extinction of a weak coherent beam by a single ion in free space. We measure the suppression of the observed extinction by tuning the frequency of a strong control laser to a two-photon resonance in a three-level Λ-type system. Furthermore, we prove that the measured extinction corresponds to a coherent process by observing the phase interference between the light fields in a Fabry-Pérot-like cavity setup, where one of the mirrors is replaced by a single-atom reflector. The change of the amplitude of the laser field due to a modification of the electromagnetic mode structure around the atom is observed in a novel regime, in which the probe-laser beam intensity is already changed by the atom alone.

We demonstrate heralded generation of entanglement between two ions using quantum interference and detection of a single photon scattered from two effectively one meter distant ions. The detection of a single photon projects the internal states of the trapped ions onto an entangled state at a high rate and with a fidelity limited by atomic motion. We show the ability to control the entangled state phase by changing the path length of the single-photon interferometer.

Zusammenfassung

Gefangene Ionenkristalle gelten als eine der vielversprechendsten physikalischen Implementierungen von Quantenbits aufgrund der exzellenten Möglichkeiten ihre Bewegung zu kontrollieren, lange Kohärenzzeiten der elektronischen Niveaus zu erreichen und die elektronischen Zustände der Ionen durch ihre gemeinsame Bewegung effizient zu koppeln. Diese Eigenschaften machen gefangenen Ionen zu einem idealen System um ein skalierbares Quantennetzwerk zu realisieren. Hierfür muss eine effiziente Schnittstelle zwischen gefangenen Ionen und Photonen entwickelt werden.

Diese Dissertation beschreibt die Realisierung von Atom-Licht Kopplungsschemen im freien Raum. Unser System besteht aus ein oder zwei gefangenen $^{138}Ba^{+}$ Ionen im Fokus einer Linse mit hoher numerischer Apertur. Wir untersuchen experimentell zwei Möglichkeiten der Verteilung von Quanteninformation, basierend auf deterministischen und probabilistischen Wechselwirkungen zwischen einzelnen Atomen und Lichtfeldern.

Dazu realisieren wir ein Absorptionsspektroskopie-Experiment und demonstrieren die Auslöschung eines schwachen, kohärenten Strahls durch ein einzelnes Atom im freien Raum. Durch Anpassen der Frequenz eines starken Kontrollstrahls auf eine Zwei-Photonen-Resonanz in einem Dreiniveausystem vom Λ-Typ beobachten wir eine Unterdrückung der Auslöschung. Durch Beobachten der Interferenz der Lichtstrahlen in einem Fabry-Pérot Interferometer, in dem einer der Spiegel durch ein einzelnen-Atom-Reflektor ersetzt ist, zeigen wir dass die gemessene Auslöschung einem kohärenten Prozess entspricht. Die Änderung der Amplitude eines Laserfelds aufgrund einer Modifikation der elektromagnetischen Struktur in der Umgebung eines Atoms wird in einem neuartigen Regime beobachtet, in dem die Intensität des Probelaserstrahls bereits durch das Atom allein verändert wird.

Wir zeigen ein Protokoll zur vorhergesagten Erzeugung von Verschränkung zweier Ionen, das auf Quanteninterferenz und Detektion eines einzelnen Photons basiert. Durch Detektion eines einzelnen Photons, das an beiden, effektiv einen Meter enfernten Ionen gestreut wurde, wird der Zustand der Ionen auf den verschränkten Zustand projiziert. Dieses Protokol zeichnet sich durch eine hohe Erzeugungsrate aus. Die Güte des erzeugten Zustands ist durch die Bewegung der Ionen beschränkt. Wir zeigen die Kontrolle der Phase des verschränkten Zustands durch Veränderung der Weglänge eines Einzel-Photon-Interferometers.

Contents

1 Introduction

Quantum mechanics has the great distinction of being one of the most successful and at the same time one of the most mysterious physical theories. It was developed at the beginning of 20th century and came to its current form in the late 1920s. During the following decades, physicists had an impressive success in applying quantum mechanics for understanding a wide range of phenomena at atomic length scales. This understanding led to many breakthrough inventions which are nowadays routinely used in our everyday life, among the most important the invention of the laser [1, 2] and transistor [3], which not only found applications in a large variety of modern devices, but still contribute as essential tools to fundamental research in many scientific areas. In the last two decades we have witnessed the emergence of the field of quantum information which represents a synthesis of quantum physics with information theory and computer science. It makes direct use of quantum phenomena, such as superposition and entanglement, to perform tasks that are computationally demanding or even impossible using classical information networks and computers [4]. Impressive progress in this field has been achieved due to the development of experimental techniques providing good isolation of individual quantum systems from the environment and enabling their control and manipulation with very high precision. Examples of such systems include trapped neutral or charged atoms, photons, superconducting qubits and color centers in diamonds. In a number of these physical systems, quantum bits (qubits) have been successfully implemented and used to demonstrate proof-of-principle logical operations including universal quantum gates [5,6], realizations of quantum error correction protocols [7,8] and efficient simulations of various quantum phenomena [9, 10]. Several demonstrations of Shor's fast factorization and Grover's search algorithms with different physical systems [11–14] and the development of practical quantum communication links over distances of more than hundred kilometers [15, 16] have been realized. These implementations are now stimulating an enormous effort towards overcoming the limited scalability imposed by the current technology. These limitations apply to both the effective number of qubits and number of controlled consecutive operations in a quantum computation, and to achievable physical distances in quantum communication networks. One possible solution to the scalability restrictions in quantum information processing is the use of quantum systems consisting

of several physical implementations of qubits, such that the advantageous physical properties of the different qubits can be matched in a way which allows the overall system to overcome the intrinsic limitations of its individual constituents.

The most elementary example of such a hybrid quantum system consists of the combination of qubits implemented in the physical degrees of freedom of electromagnetic radiation and matter particles. This combination has several inherent advantages related to the coherence properties of the flying (light) and static (matter) qubits. It allows the construction of quantum networks, in which static qubits serve for storage and local manipulation of quantum information and flying qubits enable fast transfer of this information between distant physical locations. Coupled light and matter encoded qubits provide a basis for most of the quantum communication and computation protocols. These include the idea of distributed quantum computation which overcomes the limited computational power of a local quantum processor by entangling large numbers of spatially distant processors [17–19]. Light-matter quantum interfaces correspond to the basic building block of quantum repeater devices designed to overcome the problem of exponential decay of photon pulses due to absorption and scattering losses in communication channels [20–22]. For these reasons, implementation of efficient interfaces between matter and light qubits has recently become one of the most investigated directions in experimental quantum information science. They are not only promising solutions to current scalability problems, but to a large extent help to stimulate fundamental research of light-matter interaction and quantum-electrodynamic theories.

There are two possible approaches to the realization of light-matter quantum interfaces [23]. The first is based on achieving the required strong interaction between the light and matter by means of enhancing the photon absorption and directional emission using high finesse cavities [24–26] or optically dense atomic ensembles [27–29]. Recent technological advances in the construction of high numerical-aperture optics stimulated the studies and realization of such deterministic interaction also in a free space simply by strong focusing of the light field onto a single quantum particle [30–36]. This approach aims for near-deterministic generation of matter-light entanglement and quantum state transfer from a flying to static qubit and vice-versa. The second approach is purely probabilistic and leads to quantum information schemes based on the generation and distribution of distant entanglement using interference processes and projective detection [21, 37, 38]. It also profits from efficient coupling between light and matter particles as the rate and fidelity of the generated states directly depend on the collection efficiency of the emitted photons, however the technological requirements on the strength of this coupling are much less restrictive.

A number of fundamental questions about the efficiency and technical feasibility of these basic quantum networks building blocks arise, here we present their short summary:

- What is the maximum achievable absorption probability with a high numerical aperture optical system for a single quantum emitter in a free space?
- Can such systems be employed for observing the phenomena usually associated with coherent processes in optically thick media, like electromagnetically-induced-transparency (EIT) or Faraday rotation of polarization of light?
- Can a single quantum emitter coupled to light in free space serve as an efficient quantum memory and to what extent is the process of light scattering in the regime of strong focusing coherent?
- How does the motion of the matter particle limit the interaction with light, and could the temperature of the quantum object be precisely estimated from the change of the matter-light interaction strength?
- How can we achieve the generation of the heralded entangled states between distant matter qubits with high rate and possibility of controlled single-qubit rotations necessary for distributed quantum computation?
- Which scheme for the probabilistic generation of distant entanglement is most efficient and feasible with respect to the given technological limitations and how do the rate and fidelity of the produced states scale with various experimental parameters?

In this thesis we attempt to provide an answer to these questions by realizing several experiments, in which we trap and optically cool one or two quantum particles - Barium ions in an ultrahigh vacuum to suppress their coupling to the environment. The ions are positioned at the focus of high numerical aperture lenses which mediate the strong interaction with the light. Together with a single boundary condition imposed on the electromagnetic field along the direction of the lenses mimicked by a single dielectric mirror [39], our setup offers various regimes to study the atom-light interaction in free space. Figure 1.1 shows schematic depictions of different experimental regimes studied in this thesis. By focusing a weak coherent beam onto a single ion using the high numerical aperture lenses we can look at the effects related to extinction or absorption, see figure 1.1-a). A single plane mirror imposes a boundary condition on the electromagnetic field modes and allows us to study the quantum-electrodynamics effects due to the change of the vacuum mode density at the position of the ion, see figure b). In addition, the fluorescence self-interference signal provides us with lot of information about the motional state of an ion, since phase-modulation of the fluorescence emitted by a moving ion translates here into the intensity modulation at given motional frequencies due to the interferometric setup. By combining the two experimental configurations from figures a) and b) we obtain the setup which represents a first step towards merging the

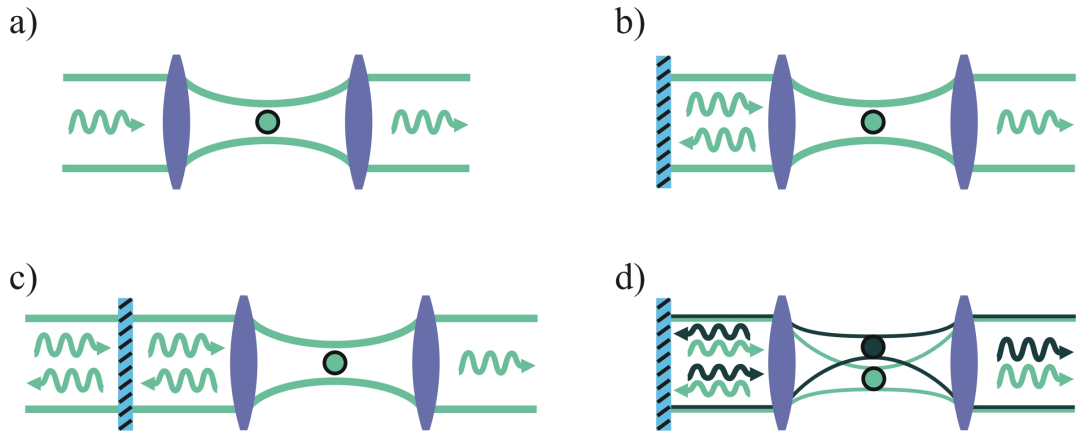

Figure 1.1: Various regimes of interaction between the ions and the electromagnetic field mode in free space investigated in our experiments.

fields of cavity-QED with free-space atom-light coupling, see figure c). Here, the coupling of the atom to the probe beam is modified by a single mirror in a regime where the probe intensity can be already significantly suppressed by the atom without the mirror. Last, we consider a system of two ions positioned in the focus of the high numerical aperture lens, see figure d). They can be aligned within the same optical mode using the distant mirror. This configuration allows us to examine the effect of mutually coherent emission between the two atoms corresponding to super/subradiance processes due to their interaction through the radiation field. Furthermore, spatial indistinguishability of the atomic fluorescence along this mode enables interference experiments with fluorescence photons coming from the two atoms.

The thesis is structured as follows: chapter 2 is dedicated to a basic description of our experimental setup. In its first part we briefly summarize the principles of ion trapping using Paul traps and describe the light-atom interaction including the motional degrees of freedom of the atom, which is necessary for understanding the presented experiments. In the second part of chapter 2, we summarize the crucial parameters of our two Barium traps experimental setups and laser systems. Chapter 3 is concerned with the experimental realization of $^{138}Ba^{+}$ qubits on the optical and radio-frequency transitions, respectively. The measurements of excitation spectra and realizations of coherent qubit rotations are presented. In chapter 4 we apply the self-interference setup (fig. 1.1-b) to the measurement of the ion's temperature close to its motional ground state. These measurements together with the developed theoretical description are not just a new single-atom thermometry tool, but present an important step towards understanding how atomic motion limits the efficiency of atom-light quantum interfaces. Chapter 5 deals with different experiments based on observation of an extinction of a weak coherent beam from an single atom in a free space. It is divided into three parts

where we present the qualitative theoretical description and experimental results of the free-space extinction, EIT and atom-mirror-cavity experiments, respectively. Chapter 7 describes the experimental realization of the two-atom entanglement by single photon interference and detection. The summary in chapter 8 proposes the future extensions of our experimental setup and suggests possible improvements and solutions to inefficiencies in the presented experiments.

2 Trapping and manipulation of single Barium ions

This chapter first briefly summarizes the theoretical background for understanding the ion trapping in Paul traps and the interaction of the two-level system with laser light including the motional degrees of freedom. The overview of our experimental apparatus including the particular trapping and laser alignment configurations relevant for the experiments realized in this thesis is then presented.

2.1 Barium Ion

Barium has played historically a very important role in ion trapping experiments. Single ionized $^{138}Ba^{+}$ was one of the first ions trapped and observed. Many pioneering experiments studying the single-atom single-photon interactions were conducted on the Barium, including the first observation of quantum jumps, sideband cooling, or the experiment where the first image of a single atom has been taken [40–42].

Neutral Barium is a soft silvery alkaline earth metal. It occurs in nature in a form of seven stable isotopes, where the most common ones, ^{138}Ba and ^{137}Ba, have natural abundances of 71.7% and 11.3%, respectively [43]. Both isotopes are nowadays extensively used in experiments which aim to study the fundamental processes of atom-light interaction in quantum optics and quantum information science [44–49]. Furthermore, the $^{137}Ba^{+}$ seems to be also a good candidate for realization of precision frequency standards [50]. The lifetime of the metastable $5D_{3/2}$ state of 80 s [51, 52] is among the longest of currently used ions resulting in a very high quality factor at the quadrupolar $6S_{1/2} \leftrightarrow 5D_{3/2}$ transition of more than 10^{16}.

2.1.1 Electronic level scheme

For the experiments presented in this thesis only $^{138}Ba^{+}$ is used. Several properties make this element very convenient for ion trapping. It has no nuclear spin, which simplifies

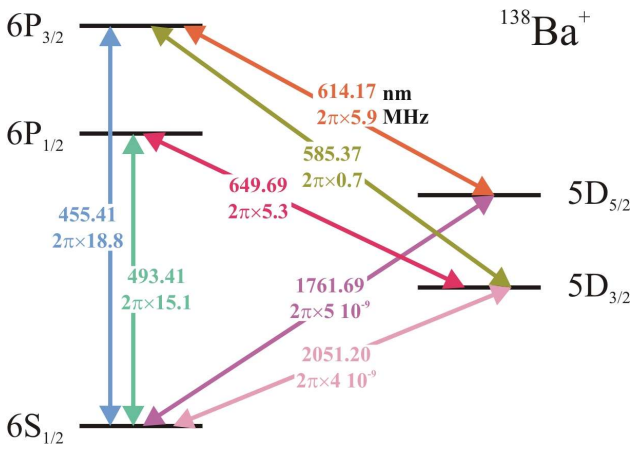

Figure 2.1: Electronic level scheme of $^{138}Ba^{+}$. Wavelengths are given in nm and decay rates are in MHz.

the laser cooling scheme. Furthermore, all the relevant electronic transitions for Doppler-cooling are in the visible range, thus easy to handle and to detect, and the corresponding wavelengths of 493 nm and 650 nm are obtainable with conventional laser diode setups. The high atomic mass of Barium also makes it more resistant to background collisions in a vacuum environment, which allows for longer storage times. The lowest electronic states of $^{138}Ba^{+}$ are shown in figure 2.1. The dipole transition $6S_{1/2} \leftrightarrow 6P_{1/2}$ with transition wavelength 493.41 nm and decay rate $2\pi \times 15.1$ MHz is essential for all the experiments presented in this thesis. It is used for laser cooling, optical pumping, readout of the qubit states, and the light scattered from it serves for studies of quantum-electrodynamic effects in various interference experiments. Furthermore, the wavelength of the emitted photons is very close to the peak sensitivity of the human eye (498 nm) under low light intensity conditions, where scotopic vision applies. This enables experiments, where single Barium ions can be seen by bare eyes using simple optical imaging systems. Particularly in our experiment, we trap and laser-cool a single Barium ion and collect about 2% of its fluorescence by a macroscope (Leica/Wild M400), which under optimal driving conditions allows us to observe a single atom directly with our eyes without any amplifying electronic setups.

In about one out of four cases, the population of the $6P_{1/2}$ state decays into the metastable $5D_{3/2}$ level, from where it is transferred back to the cooling transition using a 649.69 nm laser. The $5D_{3/2} \leftrightarrow 6P_{1/2}$ transition has a decay rate of $2\pi \times 5.3$ MHz. The $6S_{1/2} \leftrightarrow 5D_{3/2}$ and $6S_{1/2} \leftrightarrow 5D_{5/2}$ transitions are dipole-forbidden but quadrupole-allowed with natural lifetimes of 80 and 64 seconds, respectively. They correspond to obvious choices for the realization of qubits in $^{138}Ba^{+}$. The initialization of one of the qubit states can be done conveniently using a σ-polarized 493 nm laser beam, which optically pumps the ion into one of the $6S_{1/2}$ Zeeman substates. Qubit manipulations

can then be carried out by narrow-linewidth lasers with the wavelengths of 2051 nm and 1762 nm, that are nowadays commercially available with free-running linewidths of several tens of kilohertz.

2.2 Basic theoretical description

2.2.1 Paul trap

An important condition for the realization of experiments with single-atom systems is the ability to confine them in a well defined spatial region and to isolate them from unwanted coupling to the environment. In the case of charged particles, the natural way to achieve this is to exploit the interaction between them and electro-magnetic fields. Strong confinement of charged particles in all three dimensions can be provided by Paul traps, which employ a combination of static and dynamical electric potentials [53]. Paul traps are extensively studied for example in [54,55] and a detailed description of the most common traps used in Innsbruck can be found in [56–59]. Here we summarize only the main terms and parameters related to the motion of a charged particle in a Paul trap.

Paul traps create potentials of quadrupolar spatial shape consisting of static and time-dependent components. The motion is decoupled in spatial eigenmodes and thus we can further consider only motion along one direction i. If we assume a sinusoidally varying time-dependent part with frequency ω_{RF}, the solution of the classical equations of motion of a charged particle with mass m and charge $Z|e|$ in the lowest order approximation and for stability parameters $(a_i, q_i) \ll 1$ can be found [55]

$$r_i(t) \propto \cos(\beta_i \frac{\omega_{\mathrm{RF}}}{2} t)(1 - \frac{q_i}{2}\cos(\omega_{\mathrm{rf}} t)), \tag{2.1}$$

where $\beta_i \approx \sqrt{a_i + q_i^2/2}$. The parameters $a_i \sim U_{\mathrm{DC}}$ and $q_i \sim U_{\mathrm{RF}}$ are usually called stability parameters and are related to the geometry of the trap, the amplitude the applied static U_{DC} and radio-frequency U_{RF} voltages, frequency ω_{rf}, charge and mass of the ion [55]. As can be seen in equation (2.1), the solution for the trajectory r_i corresponds to the superposition of two oscillatory motions, one with an oscillation frequency $\nu_i = \beta_i \frac{\omega_{\mathrm{RF}}}{2}$ called *secular motion* and motion with an oscillation period equal to the trap driving frequency ω_{RF} called *micromotion*. The amplitude of the micromotion is smaller than the amplitude of secular motion by a factor $q_i/2$. The micromotion amplitude can usually be made very small by shifting the ion to the exact minimum of the radio-frequency potential and for many calculations it can be neglected [55]. The trajectory of an ion trapped in a Paul trap can then be approximated by the one of a classical harmonic oscillator with frequency ν_i, what corresponds to the so-called *secular approximation*. This comes from the fact that one averages over one period of micromotion. Typical well depths associated

with the corresponding potential are in the range from several hundred meV to tens of eV [60].

2.2.2 Light-matter interaction

In this section we briefly introduce the description of the interaction of a two-level system with a classical light field including the motional degrees of freedom of an atom trapped in a Paul trap. The two-level approximation can be justified by the fact that fields coupling to the atom are close to the resonance of the considered transition and off-resonant interactions with other transitions are negligibly small. This is the case for the interactions considered in this thesis, because the coupling strengths of the electromagnetic fields to the employed transitions are much smaller than the detunings relevant for the possible off-resonant couplings.

The total Hamiltonian of the trapped-atom-light system can be written as

$$\hat{H} = \hat{H}^{(e)} + \hat{H}^{(m)} + \hat{H}^{(i)}, \tag{2.2}$$

where $\hat{H}^{(e)}$, $\hat{H}^{(m)}$ and $\hat{H}^{(i)}$ correspond to the Hamiltonian of a two-level system, the motional Hamiltonian along one trap axis and the Hamiltonian describing the interaction with the applied electromagnetic field, respectively.

The two-level Hamiltonian $\hat{H}^{(e)}$ can be conveniently expressed in the spin-1/2 operator basis as

$$\hat{H}^{(e)} = \hbar\omega_0/2(|e\rangle\langle e| - |g\rangle\langle g|) = \hbar\omega_0\hat{\sigma}_z/2, \tag{2.3}$$

where $|g\rangle$ and $|e\rangle$ correspond to the ground and excited states of the two-level system and ω_0 is the frequency corresponding to the energy difference between them. The Hamiltonian corresponding to the ion's motion in the harmonic potential is

$$\hat{H}^{(m)} = \hbar\nu(\hat{a}^\dagger\hat{a} + 1/2), \tag{2.4}$$

where creation $\hat{a}^\dagger$ and annihilation $\hat{a}$ operators are defined for the quantum harmonic motion of the ion with a frequency ν. Since the wavelength of the light-field interacting with the atom is typically much greater than the extension of its electronic wave function, it is sufficient to treat the light field in the lowest order of its multipole expansion. Electric dipole and quadrupole-allowed transitions can be jointly described by associating them with a certain strength of the on-resonance coupling expressed by the Rabi frequency Ω. For travelling electromagnetic waves with the wave-vector k, frequency ω and phase ϕ at the position of the atom, the coupling Hamiltonian has the form [55],

$$\hat{H}^{(i)} = \frac{\hbar\Omega}{2}(|g\rangle\langle e| + |e\rangle\langle g|)(e^{i(k\hat{x}-\omega t+\phi)} + e^{-i(k\hat{x}-\omega t+\phi)}). \tag{2.5}$$

Here $\hat{x}$ is the position operator of the ion and we assumed that laser is pointing along the x-axis of the ion's motion. After transformation into the interaction picture corresponding to $\hat{H}_{\text{int}}(t) = \hat{U}^{\dagger}\hat{V}(t)\hat{U}$ with $\hat{U} = e^{i\hat{H}_0 t/\hbar}$, interaction part $\hat{V}(t) = \hat{H}^{(i)}$ and the free Hamiltonian $\hat{H}_0 = \hat{H}^{(e)} + \hat{H}^{(m)}$, we perform a rotating-wave approximation by dropping the fast oscillation terms with frequency $(\omega + \omega_0)$. We obtain the transformed interaction Hamiltonian

$$\hat{H}_{\text{int}}(t) = \frac{\hbar\Omega}{2}\hat{\sigma}^{+} \exp i(\eta(\hat{a}e^{-i\nu t} + \hat{a}^{\dagger}e^{i\nu t}) - \delta t + \phi) + \text{H.c.}, \tag{2.6}$$

where η is the Lamb-Dicke parameter

$$\eta = kx_0 = k\sqrt{\hbar/(2m\nu)}. \tag{2.7}$$

Here x_0 is the atomic motional ground state wave-packet extension. The detuning $\delta = \omega - \omega_0$ corresponds to the difference of the light field from the two-level system resonance frequency. Equation (2.9) describes the selective coupling between certain motional and electronic states of a trapped ion induced by the interaction with a light field depending on the detuning δ. The Rabi frequency for the transitions with motional quantum numbers n and $n + m$ corresponds to,

$$\Omega_{n,n+m} = \Omega|\langle n + m|e^{i\eta(\hat{a}+\hat{a}^{\dagger})}|n\rangle|. \tag{2.8}$$

Equation (2.9) can be expanded in η to obtain a general form of the coupling strength between the motional states of the atom with various phonon numbers [55,56,61] and can be further simplified if the extension of the ion's motional wave-function is much smaller than wavelength of the light field interacting with it, what corresponds to the so-called *Lamb-Dicke regime*, i.e. $\eta \ll 1$. Expansion to lowest order in η gives

$$\hat{H}_{\text{int}}(t) = \frac{\hbar\Omega}{2}\hat{\sigma}^{+}(1 + i\eta(\hat{a}e^{-i\nu t} + \hat{a}^{\dagger}e^{i\nu t})e^{i(\phi-\delta t)} + \text{H.c.} \tag{2.9}$$

This Hamiltonian contains three resonances, which correspond to the *carrier transition*, the *red* and *blue sideband transitions* for the laser detunings $\delta = 0$, $\delta = -\nu$ and $\delta = \nu$, respectively. The corresponding Rabi frequencies for the red and blue sideband couplings are

$$\Omega_{n,n-1} = \Omega\sqrt{n}\eta \quad \text{and} \quad \Omega_{n,n+1} = \Omega\sqrt{n+1}\eta, \tag{2.10}$$

where Ω is the Rabi frequency on the carrier transition and n is the phonon number in the relevant motional mode of the ion.

2.3 Experimental setup

2.3.1 General overview

The main part of our experimental setup consists of two Paul traps enclosed in two separate vacuum chambers. In both chambers the vacuum at the order of 10^{-10} to 10^{-11} mbar is maintained using ion pumps and Titanium-sublimation pumps and both systems are equipped with vacuum gauges able to measure the pressure down to the 10^{-11} mbar range. Installed electron emitters (BaO-disc ES-015, Kimble-physics) allow us to achieve ionization of an atomic beam by electron impact-ionization process. However due to the higher ionization efficiency, isotope selectivity and absence of production of stray fields at the trap electrodes we use solely a photo-ionization process for the experiments presented here.

The lab is equipped with five laser systems. A photo-ionization laser at 413 nm, lasers to excite dipole transitions at 493 nm, 650 nm, 614 nm and a 1.762 μm laser used for driving the narrow quadrupolar transition, see figure 2.1 for the corresponding atomic transitions. The beams from all the lasers are distributed to both ion traps. Laser light at 413 nm used for photo-ionization of neutral Barium by a resonant two-photon process [57] is generated using a commercially available diode laser (Toptica DL100). This laser delivers 2.5 mW of optical power and is used in a free running regime, that means its frequency is not actively stabilized but it is only manually adjusted according to the measurement result on a wavemeter (High Finesse, WS7). The laser systems at 493 nm and 650 nm are used for excitation of Barium ions on the dipole transitions $6S_{1/2} \leftrightarrow 6P_{1/2}$ and $6P_{1/2} \leftrightarrow 5D_{3/2}$, respectively. Light at 650 nm is obtained directly from a laser diode (Toptica, DL100) which is locked to an optical resonator using a Pound-Drever-Hall lock (PDH) to improve its frequency stability. The maximum available power of the 650 nm beam at the output of the laser is 8 mW. The 493 nm beam is generated by frequency doubling of the 986 nm laser light coming from a diode laser system (Toptica, DL Pro) at 986 nm, which is locked using a PDH-lock to an optical cavity. About 20 mW of the 493 nm light is available at the output of the doubling cavity. Part of the 493 nm beam is used for a modulation-transfer-spectroscopy (MTS) lock to a Tellurium Te_2 transition. The error signal from the MTS serves for the long-term stabilization of the 986 nm cavity resonance frequency by shifting the position of one of the cavity mirrors using a piezoelectric transducer. In this way long-term and short-term frequency stability of the 493 nm light is achieved. A more detailed description of the 493 nm laser system and its locking scheme can be found in [62]. Laser systems with the output wavelengths of 1.762 μm and 614 nm for driving the quadrupole $6S_{1/2} \leftrightarrow 5D_{5/2}$ transition and the dipole $5D_{5/2} \leftrightarrow 6P_{3/2}$ transition were developed within the experiments presented in this thesis, and their detailed description can be found in chapter 3.2.2.

An essential part of all experiments presented in this thesis is the detection of single fluorescence photons with a good time resolution and high detection efficiency. Photon counting in our laboratory is done mostly with photomultipliers (PMT, Hamamatsu H7421-40), which have been partially replaced by fiber-coupled avalanche photodiodes (APD, Laser Components, COUNT blue). The measured detection efficiencies of our APDs at 493 nm are in the range of 60 to 70 %, providing us with the gain of almost of factor of two compared to the electron-photomultipliers. Together with a very low dark-count rate of less than 10 Hz, they became very crucial for the atom-photon correlation measurements presented in chapter 6. In our detection setup every single photon detection event generates a TTL pulse at the output of the detector which is then further processed in NIM logic electronics consisting of a TTL to NIM pulse converter, discrimination stage (LeCroy 821), pulse-counter (LeCroy 3615), time-to-digital converter (TDC, LeCroy 4204) and histogram memory (LeCroy 3588). Continuous photon counting with a fixed time interval is usually realized using the pulse-counter (LeCroy 3615) and monitored by LabVIEW (National Instruments) software. In the pulsed regime, where precise time definition of the detection time interval is required, photon counting is done using a time-tagging device (PicoHarp 300, PicoQuant) which records the arrival times of detected photons with a resolution of up to 4 ps for two input channels. The detected count rate in the defined time window can then be read out by summing the number of detection events between two triggering pulses.

To generate the sequences of laser pulses and various triggering signals, we implemented a programmable pulse generator (PPG) with 16 digital TTL output channels and a single radio frequency output [63]. Fast switching of the laser beams is then realized by switching the RF-signals sent to acousto-optical modulators. These signals are in the case of our dipole transition lasers generated by voltage-controlled-oscillators and switched by TTL pulses generated by the PPG digital outputs using a series of RF-switches. For the 1.76 μm laser, the RF-signal is generated by a direct-digital synthesizer, which allows for phase-coherent switching necessary for the qubit manipulations. The PPG system is controlled using computer software TrICS (Trapped Ion Control Software) currently being developed in our group.

2.3.2 Ring trap setup

Here we will briefly describe the experimental setup containing the ring Paul trap. A schematic overview of the experimental apparatus including the directions of the cooling lasers, the coils generating the static magnetic field at the position of an ion and the fluorescence detection setup is shown in the figure 2.2-a). A detailed description of this setup including the particular parameters of the vacuum chamber, Barium ovens and resonance circuits can be found in reference [58].

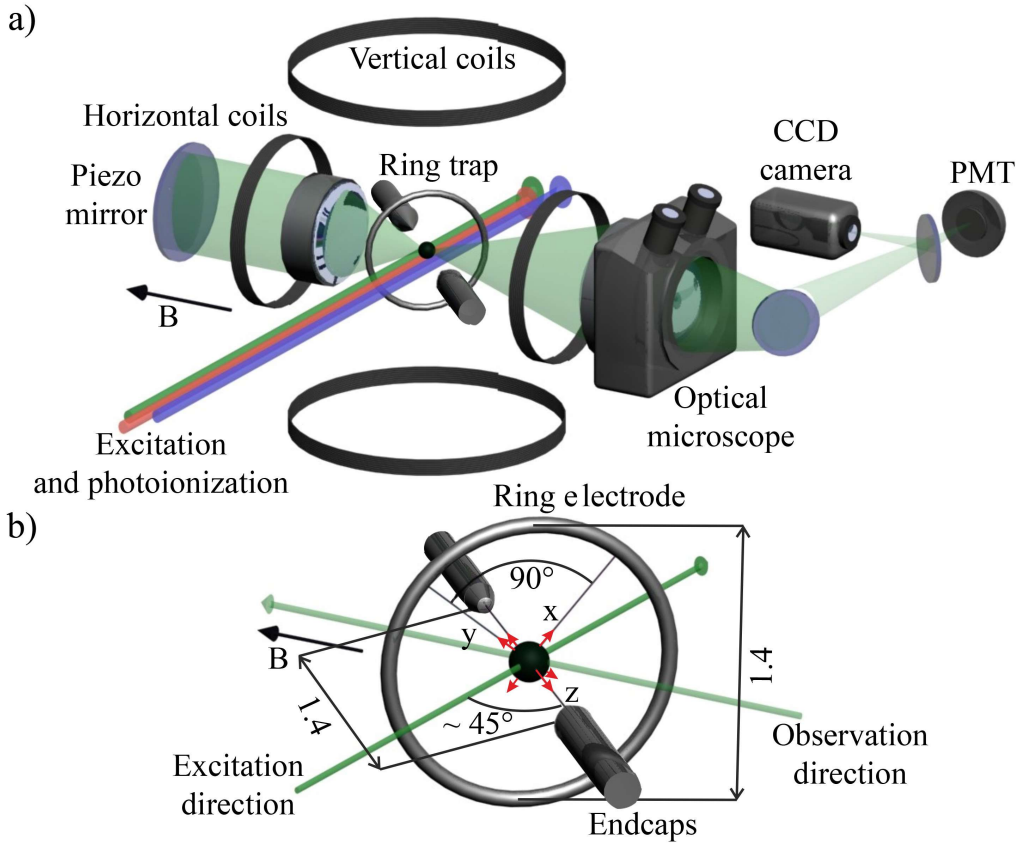

Figure 2.2: Experimental setup with the ring Paul trap. a) Configuration of the excitation lasers, detection channels, high numerical aperture optics and the coils for magnetic field generation. b) Depiction of the orientation of cooling lasers with respect to the observation direction and normal modes of motion. All dimensions are in mm.

Our ring trap corresponds to one of the most typical realizations of a Paul trap. It consists of a single ring electrode and two endcaps aligned along its symmetry axis. The ring electrode is made out of 0.2 mm molybdenum wire with inner radius of 0.7 mm and two endcap electrodes with the same thickness separated by a distance of 1.4 mm, see figure 2.2-b). Two additional wires positioned perpendicularly with respect to the endcap electrodes are used for micromotion compensation [58]. The ring electrode is connected to a radio-frequency source at $\nu_{\mathrm{RF}} \sim 19.4$ MHz and the endcap electrodes are grounded. The electric field creates a pseudopotential with a depth of around 50 eV and single ion storage times can reach several months even in the absence of cooling lasers. The motional modes can be decomposed into three normal modes along the axes x, y and z as depicted in the figure 2.2-b) with motional frequencies of $\nu_x = 0.9$ MHz, $\nu_y = 1.1$ MHz and $\nu_z = 2$ MHz, respectively, for a radio-frequency power of 5 W transmitted to the ring

electrode via helical resonator. Secular motions in the plane of the ring are called radial motions and oscillation along the symmetry axis is usually referred to as axial motion.

Two pairs of Helmholtz coils are sufficient to precisely define a magnetic field collinear with the observation direction and perpendicular to the cooling and excitation laser beams. The fluorescence of the ion is collected in two opposite directions. A macroscope objective (Leica/Wild M400) with numerical aperture NA $\sim$ 0.24 collects 1.5 % of fluorescence light which is after additional spatial and frequency filtering focused on the photomultiplier (PMT, Hamamatsu H7421-40) or an intensified CCD camera (Andor Luca) depending on the position of a flip-mirror. In the opposite observation channel the light is collected and collimated by a high quality custom-made high-NA lens (Linos, Halo 25/04) with an NA = 0.4 positioned inside the vacuum chamber. The lens has a working distance of 12 mm and collects the light from a 4 % fraction of the full solid angle.

The main advantage of the ring-trap setup is the high contrast of the interference in the single-mirror phase interference setup, which is mainly due to the high quality of the employed imaging optics, its alignment and good Doppler cooling conditions. However, there is a strong limitation in this setup in the possibility of individual addressing of ions in a multi-ion crystal using one of the mentioned high-NA lenses imposed by the design and the particular positioning of the ring-trap, which makes some particular experiments with more ions difficult to realize. Experiments with more ions would be limited also by the residual micromotion which can be well minimized only in the center of the trap.

2.3.3 Linear trap setup

In the following paragraph, we will summarize the experimental alignment and main trapping parameters of the experimental setup employing a linear Paul trap. The figure 2.3-a) shows a schematic depiction of the setup including the directions of exciting lasers, the detection optics and the magnetic field coils. A detailed description of the vacuum chamber and exact dimensions of the trap electrodes can be found in reference [57]. Our linear trap consists of four blades, with one diagonal pair of electrodes connected to ground-potential and the second pair to a radio-frequency signal with frequency $\nu_{\mathrm{RF}} \sim 15.1$ MHz. The trap is operated with radio-frequency powers ranging from 2 to 7 Watts sent to the helical resonator depending on the number of ions stored and particular experimental requirements. This configuration creates a dynamical potential in the two radial directions of the trap. Additionally, a DC-voltage is applied to two endcap electrodes positioned at each end of the symmetry axis of the trap to create confinement in the axial direction. The important dimensions of our linear trap are depicted in figure 2.3-b). The half-distances between the diagonal pairs of electrodes and between the endcaps are 0.7 mm and 2.2 mm, respectively. Three pairs of micromotion compensation

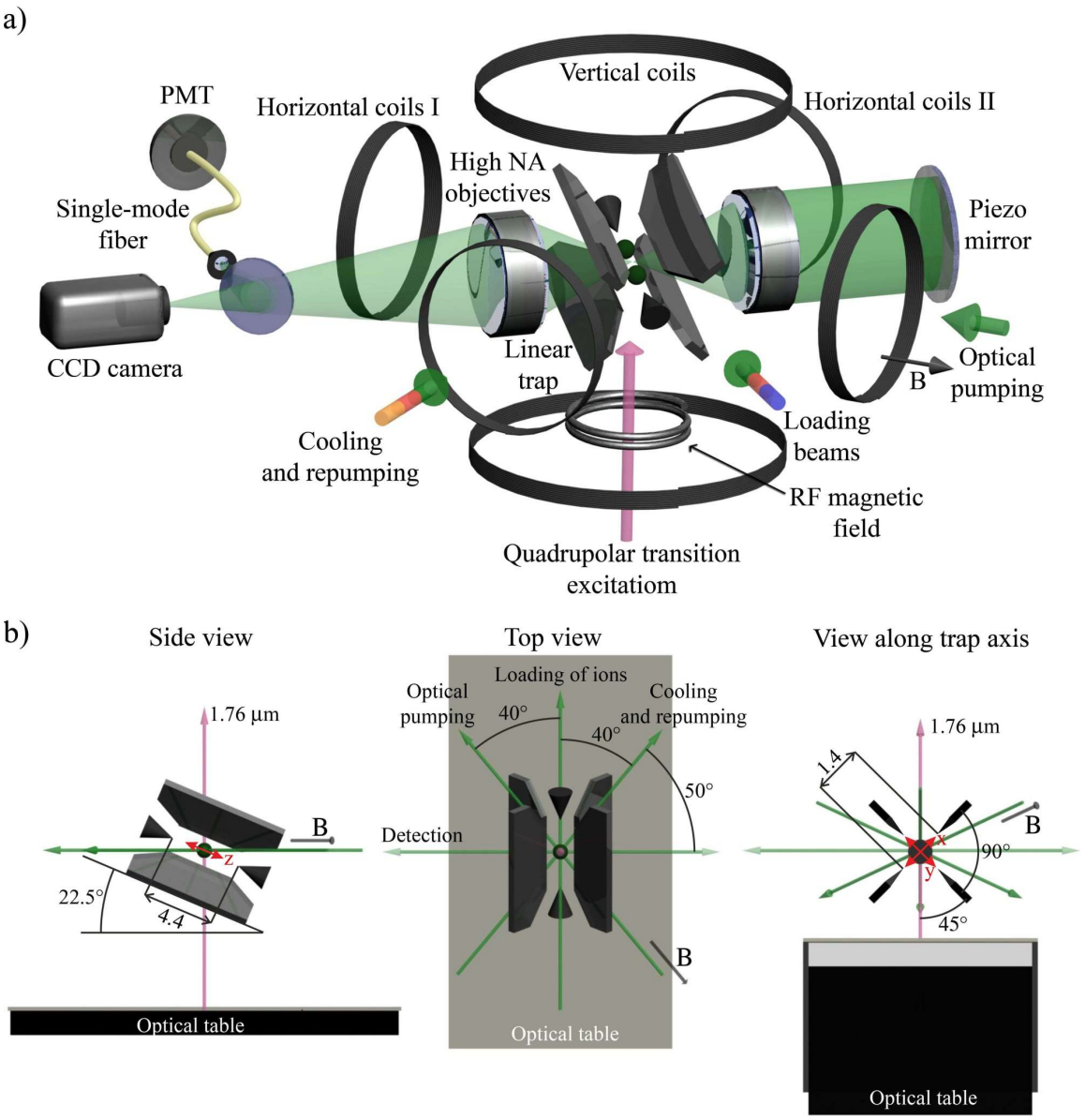

Figure 2.3: Sketch of the experimental setup employing the linear Paul trap. a) Scheme of the overall configuration of the laser beams, static and radio-frequency magnetic fields and observation channels. b) Orientation of the linear trap with respect to the plane of the optical table and directions of the laser beams, including the relevant dimensions of trapping electrodes and directions of the normal modes of motion. All dimensions are in mm.

electrodes are positioned along the trap axis to compensate for effects caused by stray fields leading to a displacement of the ion from the radio-frequency potential minimum. The corresponding Lamb-Dicke parameters for the Doppler cooling $6S_{1/2} \leftrightarrow 6P_{1/2}$ and

quadrupolar $6S_{1/2} \leftrightarrow 5D_{5/2}$ transitions and for the directions of the laser beams as presented in the figure 2.3 are summarized in table 2.1. The trap is positioned at an angle of

Motional mode	x	y	z
ν (MHz)	1.62	1.66	0.91
η for 493 nm *cooling beam*	0.0275	0.0271	0.0571
η for 1.76 μm *exciting beam*	0.0111	0.0109	0.0086

Table 2.1: Summary of Lamb-Dicke parameters η relevant for Doppler cooling on the $6S_{1/2} \leftrightarrow 6P_{1/2}$ transition and excitation of the $6S_{1/2} \leftrightarrow 5D_{5/2}$ quadrupolar transition of the Barium ion in the linear Paul trap setup. Frequencies ν correspond to the measured frequencies of secular motion for typical trapping parameters corresponding to an applied RF-power $P_{RF} = 6.5$ W and constant tip voltages of $U_{tip} = 500$ V.

22.5 ° out of the horizontal plane corresponding to the plane of the optical table, which enables cooling of the radial modes with the 493 nm beam propagating almost along the direction of the two endcaps. This beam is very convenient for loading of ions due to its simple spatial alignment procedure.

The essential parts of this experimental setup are two high numerical aperture lenses (Linos Halo 25/04) used for collection of the fluorescence emitted by the ion. These lenses are positioned inside the vacuum can at a distance of approximately 12 mm from the ion. The numerical aperture of each lens is 0.4, which corresponds to about 4 % of the full solid angle and gives the possibility to collect altogether about 12 % of the emitted fluorescence for the case of a linear dipole oriented perpendicular to the observation direction. The peak-to-valley wavefront abberations of a comparable lens were measured to be below $\lambda/10$ at 493 nm [64], sufficient for high-contrast interference experiments with fluorescence light [65, 66]. One of the lenses focuses the ion's fluorescence to a fiber-coupled avalanche photodiode (Laser Components, COUNT blue) or to an intensified CCD camera (Andor iXon), the other lens is used for collimation of the collected fluorescence and its reflection back onto an ion to demonstrate the self-interference [39]. A magnetic field with an amplitude of a few Gauss at the position of the ion is generated by three pairs of Helmholtz coils, two in the horizontal plane and one in the vertical direction. This configuration allows for compensation of the earth magnetic field and setting of an arbitrary static magnetic field direction. In all the experiments presented in this thesis, the magnetic field is oriented along the direction opposite to the propagation of the optical pumping beam at 493 nm. The coil of approximately 10 cm diameter is positioned at the distance of 6 cm from the trap center for the purpose of driving magnetic dipole transitions with a frequency splitting of several MHz, see chapter 3.3 for details.

3 Coherent quantum manipulations on Barium

3.1 Introduction

This chapter is dedicated to the description of qubits realized with $^{138}Ba^{+}$ ions. We have realized two different qubits, one on the quadrupolar transition $6S_{1/2} \leftrightarrow 5D_{5/2}$ with a frequency splitting of 1701.3 THz and a second on the magnetic dipole transition between the two Zeeman sublevels of the $6S_{1/2}$ state with frequency splitting of 11.5 MHz at a static magnetic field of 4.1 G, see figure 3.1. Throughout the thesis we will refer to these qubits as optical and radio-frequency (RF) qubits, respectively.

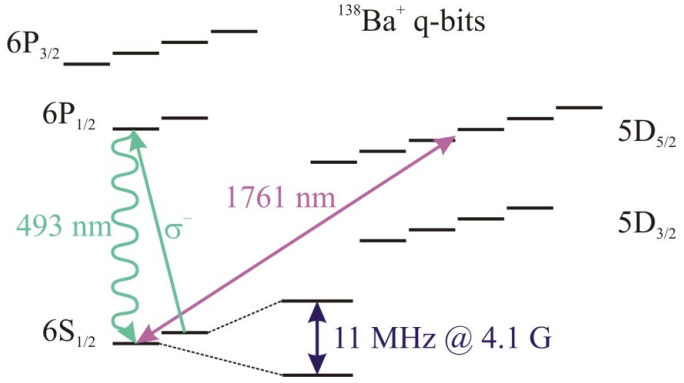

Figure 3.1: Electronic level scheme of the Barium ion including the level splitting due to the Zeeman effect. We realize efficient initialization and control of a qubit using operations on the narrow RF and optical transitions. Initialization of both qubits is achieved by optical pumping using σ-polarized 493 nm laser beam.

Precise control and manipulation of quantum states on these transitions is an important step towards the realization of quantum communication schemes and precise studies of quantum electrodynamics effects in our experiments. Furthermore, the interaction of the narrow laser on the motional sidebands of quadrupolar transition enables cooling the ion

close to its motional ground state by means of sideband cooling which further increases the efficiency of all studied interference effects, as demonstrated in chapter 4. Most of the experimental techniques described here are already well established in experiments concerned with the realization of quantum algorithms [67], quantum simulations [68] or precision spectroscopy [69] with trapped ion systems. The theoretical background describing the qubit operations is well developed and can be found in a number of theses and articles. For this reason, we will focus here only on the main experimental results and important parameters of our qubit realizations with $^{138}Ba^{+}$.

3.1.1 Quantum bits

The quantum state of a two-level system can be expressed as $|\psi\rangle = \alpha|0\rangle + \beta|1\rangle$, where α and β are complex coefficients satisfying the normalization condition $|\alpha|^2 + |\beta|^2 = 1$. An important distinction with respect to classical bits is that qubits can form any linear combination of states $|0\rangle$ and $|1\rangle$. They can be visualized in a useful way in a unit three-dimensional sphere by a vector pointing from the center of the sphere with its direction given in polar coordinates by angles ϕ and θ, usually referred to as Bloch sphere representation. In this picture, the state of the qubit can be written as

$$|\psi\rangle = \cos(\theta/2)|0\rangle + e^{i\phi}\sin(\theta/2)|1\rangle, \tag{3.1}$$

where we have omitted a global phase factor. Then the rotation of the state about the x, y or z axes by angle ζ can be written as

$$\hat{R}_{x,y,z}(\zeta) = \exp(-i(\zeta/2)\hat{\sigma}_{x,y,z}), \tag{3.2}$$

respectively, where σ_x, σ_y and σ_z are the Pauli operators. Pulses of length t, phase ϕ and Rabi frequency Ω resonant with the carrier transitions realize single qubit unitary rotations corresponding to

$$\hat{R}(\theta,\phi) = \exp(\frac{i}{\hbar}\hat{H}_{\text{carr}}t) = \exp(i\frac{\theta}{2}(\hat{\sigma}^{+}e^{i\phi} + \hat{\sigma}^{-}e^{-i\phi})), \tag{3.3}$$

where H_{carr} is the interaction Hamiltonian for the carrier transition ($\delta = 0$) in the Lamb-Dicke regime (eq. 2.9) and $\theta = \Omega t$ is the corresponding angle of rotation or pulse area [55]. The expression (3.3) corresponds to a rotation of a state around the axis lying in the $x-y$-plane of the Bloch sphere

$$\hat{R}(\theta,\phi) = \exp(i\frac{\theta}{2}(\cos\phi\hat{\sigma}_x + \sin\phi\hat{\sigma}_y)), \tag{3.4}$$

and a sequence of such rotations is sufficient for the realization of arbitrary single qubit operations [70].

3.2 Barium quadrupole transition

The main advantage of using an electric dipole-forbidden transition for implementing the qubit is the long lifetime of the excited metastable state, by which means the decoherence caused by spontaneous emission is strongly suppressed. However, other limitations for the coherence of qubits implemented on these transitions, such as fluctuations of the laser frequency or the amplitude of the applied magnetic field must be taken into an account. The necessary condition for the useful implementation of any atomic qubit is that the Rabi frequency of the applied laser field on the transition must be much faster than any decoherence process, but small enough for neglecting the off-resonant excitation of any other transition. In our experiment we employ the quadrupole transition $6S_{1/2} \leftrightarrow 5D_{5/2}$ with transition wavelength 1.76 μm and lifetime of 64 seconds. This transition has been extensively studied in [71, 72], where the authors demonstrated Rabi oscillations with the $^{137}Ba^{+}$ isotope.

Interaction between the electric quadrupole moment Q and the electric field E occurs via its gradient ∇E and the corresponding interaction Hamiltonian is

$$H^{(i)} = Q\nabla E. \tag{3.5}$$

This Hamiltonian takes the form of equation (2.5) if the Rabi frequency is defined as [73, 74]

$$\Omega = \left| \frac{eE_0}{2\hbar} \langle S_{1/2}, m | (\boldsymbol{\epsilon} \cdot \mathbf{r})(\mathbf{k} \cdot \mathbf{r}) | D_{5/2}, m' \rangle \right|. \tag{3.6}$$

Here E_0 is the amplitude of the electric field, $\mathbf{r}$ is the position operator of the electron with respect to the center of mass of the atom and (m, m') are the magnetic quantum numbers. For the interaction on the quadrupole transition, the selection rules allow transitions with a change of the magnetic quantum number of $|m - m'| = \{0, 1, 2\}$. Using expression (3.6) the strength of the coupling on the quadrupole transition can be evaluated for different geometrical configurations and for particular changes of the magnetic quantum number expressed by different Clebsch-Gordan coefficients $C(m, m')$ [73]. In our linear Paul trap experimental setup, the direction of the applied magnetic field $\mathbf{B}$ is perpendicular to the wave vector $\mathbf{k}$ of the driving laser, therefore it is impossible to excite the $\triangle m = 0$ transitions for any direction of the optical polarization vector $\boldsymbol{\epsilon}$ [56], see figure 3.2.

3.2.1 Pulsed spectroscopy

The quadrupole transition is investigated using a pulsed manipulation. The sequence of pulses can be divided into cooling, state initialization, state manipulation and detection periods, see fig. 3.3 a).

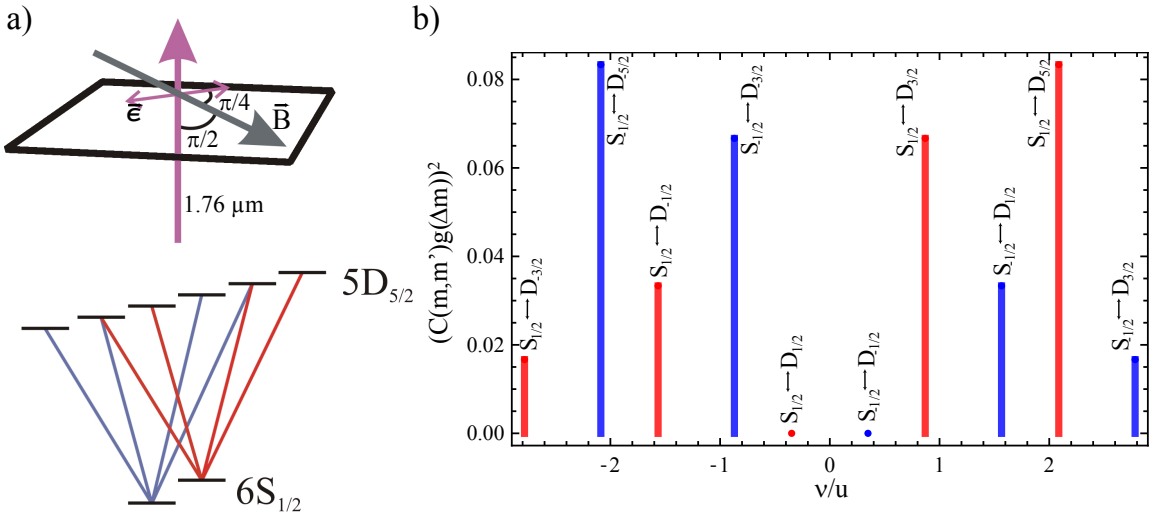

Figure 3.2: a) The geometrical configuration of the magnetic field $\vec{B}$, wave vector $\vec{k}$ and polarization $\vec{\epsilon}$ in our experimental setup allows us to drive transitions where the change of the magnetic quantum number $|\triangle m| = \{1, 2\}$. b) The theoretical prediction of the spectrum of our quadrupole transition. Height of the individual spectral lines is given by the square of the product of geometrical factor $g(\Delta m)$ and Clebsch-Gordan coefficient $C(m, m')$. The frequency splitting is plotted in units of $u = \mu_b B/h$.

During the cooling period, the ion is first optically pumped to the electronic ground state $6S_{1/2}$ by near-resonant excitation of the $5D_{5/2} \leftrightarrow 6P_{3/2}$ transition using 614 nm laser light. From the $6P_{3/2}$ state it can, however, spontaneously decay with a probability of 3.6 % also to the metastable $5D_{3/2}$ level, which is then depopulated using 650 nm laser light. Doppler cooling on the $6S_{1/2} \leftrightarrow 6P_{1/2}$ transition lasting about 2 ms results in a mean phonon number of $\overline{n} \sim 10$ in each motional mode. A single 493 nm σ^+ laser pulse propagating along the direction of the magnetic field with duration of several tens of μs is then applied to move the population into the $6S_{1/2}(m = -1/2)$ state. By comparing the detected fluorescence intensity on the dipole $6S_{1/2} \leftrightarrow 6P_{1/2}$ transition during excitation with σ^+ and linearly polarized beams we estimated the probability of finding the ion in the desired Zeeman sublevel after optical pumping to be more than 99.7 %. In the next step, sideband cooling can be optionally used to cool the ion close to its motional ground state, see chapter 4.2.

During the quantum state manipulation period, the electronic state of the ion on the qubit transition is manipulated by applying a sequence of 1.76 μm pulses with various frequencies, phase and durations. These operations can be used both for the preparation of the qubit state and for its tomographic reconstruction. The state of the qubit is read

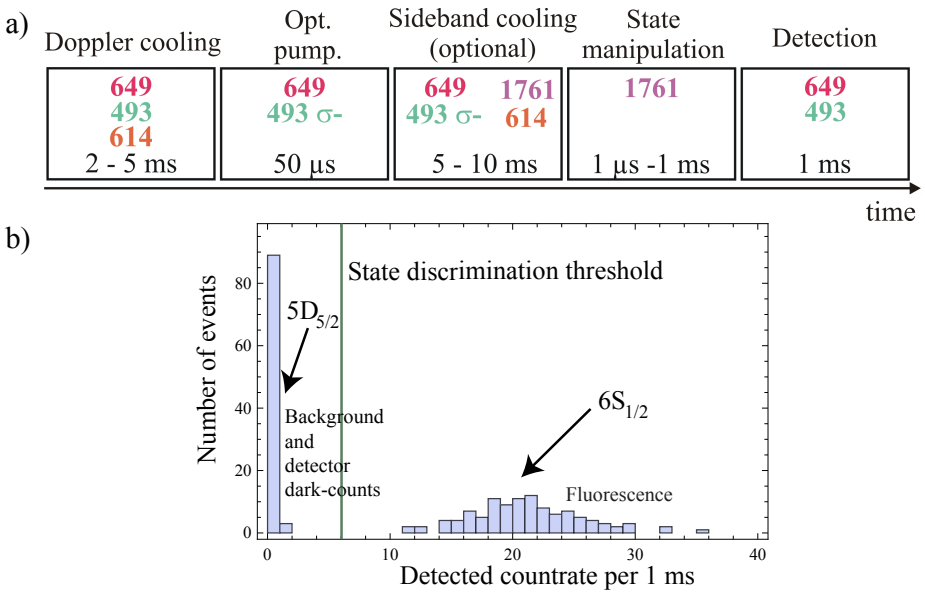

Figure 3.3: a) Typical pulse sequence for investigating the quadrupole transition. b) Example of the excitation probability measurement by electron shelving method. The presented data are the result of 200 experiments.

out using the electron-shelving technique. By continuous excitation of the $6S_{1/2} \leftrightarrow 6P_{1/2}$ transition using the 493 nm laser for about 1 ms and detection of the scattered fluorescence, the state of the electron is projected on the ground $6S_{1/2}$ or excited $5D_{5/2}$ electronic states. Projection on the S or D states is resolved by observation of the fluorescence count-rate above or below a certain threshold, respectively. The threshold corresponds to the count rate value which unambiguously separates the Poissonian distribution of the detected fluorescence photon number from the background noise peak with a small mean photon-number value.

The result of a single pulse sequence which ends with a projective measurement is a binary output reporting on finding the ion in the electronic ground or excited state. The experiment is repeated typically 200 times with the same parameters and the resulting normalized rates of finding the atom in the ground or excited state are used for an estimation of the probability P_e of the atom being in the excited $5D_{5/2}$ state. An example of the generated histogram of detected count rates is given in the fig. 3.3-b). The normalized sum of the number of detection events separated by the threshold-line corresponds to the excitation probability.

3.2.2 1.76 μm and 614 nm laser setups

We implemented two new laser setups at 1.76 μm and 614 nm and a reference optical cavity for realization of their frequency stabilization to demonstrate qubit operations and sideband cooling on the Barium quadrupolar $6S_{1/2} \leftrightarrow 5D_{5/2}$ transition.

Optical cavity

The optical cavity is made of a 10 cm long ultra-low expansion (ULE) spacer (thermal expansion coefficient of less than 10^{-9}/mK) that corresponds to the free spectral range of 1.5 GHz. As shown in figure 3.4, the spacer in fact comprises four cavities that enable the simultaneous stabilization of four different lasers (493 nm, 650 nm, 614 nm, 1760 nm). The cavity for the 1.76 μm laser is made out of high reflectivity mirrors which, in order to improve the length stability, are not mounted on piezo-electric transducers, as is the case for the three dipole laser reference cavities. The cavity is surrounded by an aluminium enclosure and placed in a stainless steel vacuum can. The vacuum chamber is kept at a constant pressure of 10^{-8} mbar using an ion getter pump. This provides thermal isolation from the environment and prevents pressure changes. For further stabilization, the vacuum can is enclosed in another aluminium housing to which four Peltier elements are connected. Temperature is then stabilized using a digital controller and the feedback-independent temperature measurements show long-term variation of the temperature inside the aluminium box of less than ± 1 mK. Measurement of the 1.76 μm cavity frequency drift as a function of its temperature reveals that the minimal sensitivity of the cavity resonant frequency to the ULE spacer temperature change corresponding to its zero expansion point is around 4°C. The metal housing is surrounded by a 5 cm thick layer of polystyrene and a plastic box for thermal and acoustic isolation. The whole cavity setup is mounted on a vibration isolation platform (Minus K Technology, BM-1). Ring down measurements show 1.76 μm cavity finesse of 1.94×10^5, which corresponds to a linewidth of 7.7 kHz (FWHM).

1.76 μm laser setup

An ion is excited on the quadrupole transition using a Thulium doped (Tm^{3+}) fiber laser (Koheras Adjustik^{TM}) with a wavelength of 1.762 μm. The laser frequency is actively stabilized to a high finesse cavity. A similar laser system has been used and described in reference [72]. The laser delivers 60 mW of power and the measured free running linewidth is about 20 kHz. It is pumped by a 1600 nm laser diode and feedback is provided by a distributed feedback mechanism, where a 5 cm long Bragg grating is incorporated in the Thulium doped fiber. The wavelength of the fiber laser is tunable within 2 nm with tuning sensitivity of about 40 pm/K by controlling the temperature of the substrate which holds

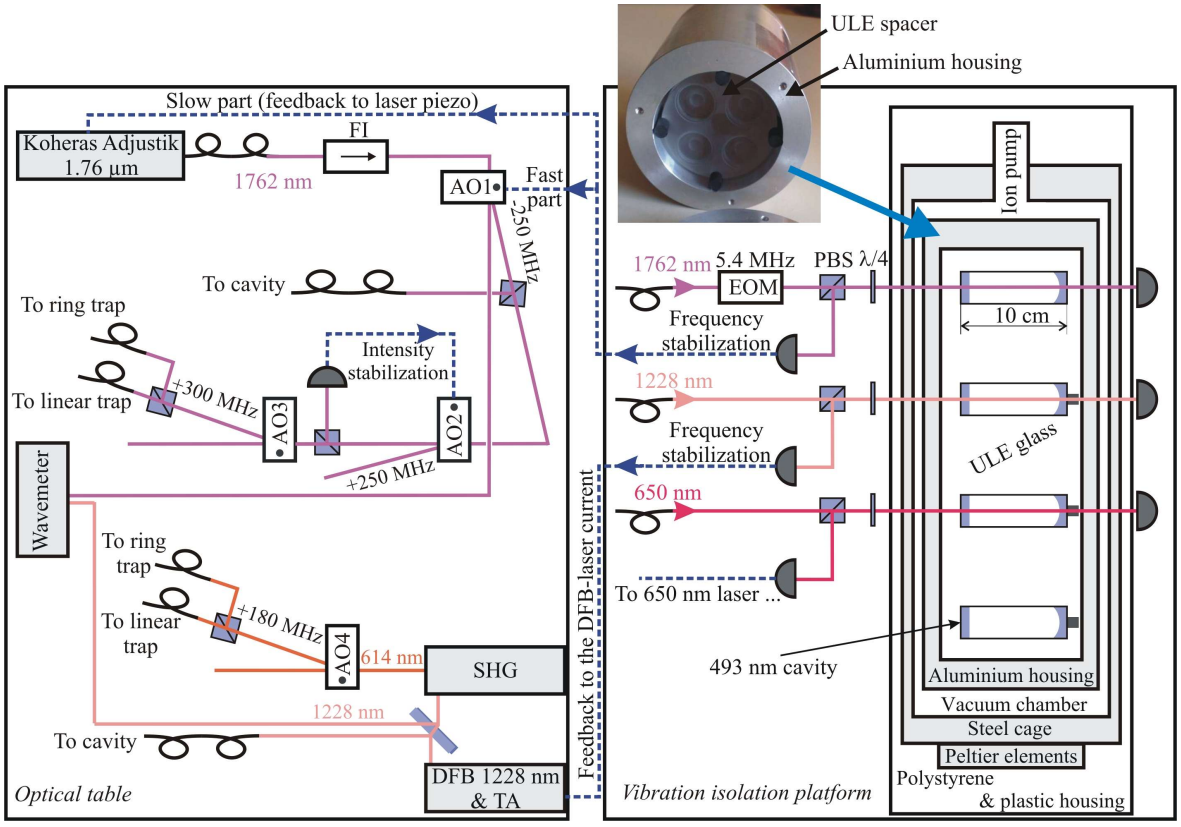

Figure 3.4: Schematic experimental setup of the 1.76 μm and 614 nm laser systems. Both lasers are frequency stabilized to Fabry-Pérot cavities placed in the same four-hole spacer using the Pound-Drever-Hall locking technique.

the fiber. For faster tuning applications, a piezoelectric component is used for straining the fiber and changing the laser frequency within a range of 30 pm with the sensitivity of about 0.2 pm/V. In order to reach a wavelength close to the resonance of our quadrupole transition we operate the fiber laser at a temperature of 43.6°C.

The emitted laser light comes out of the single mode fiber and passes through a 60 dB Faraday isolator (FI) to avoid the optical feedback from optical components back to the laser, see figure 3.4. An acousto-optic modulator AO1 shifts the laser frequency by -250 MHz and the remaining 0-th order beam is used for estimation of the laser wavelength by a wavemeter (Bristol Instruments, Model 621A-IR). The diffracted minus 1st order beam is split into two parts by a polarizing beam splitter (PBS). The part with an optical power of 2 mW is fiber guided to the optical cavity for frequency stabilization. The other part is intensity stabilized by measurement of a small fraction of the light on a photodiode and feedback of the generated error-signal to the AO2 [75]. The intensity of the beam and the additional frequency offset are then set by frequency modulation using AO3. The power and frequency of the radio-frequency signal driving AO3 is controlled using a

programmable pulse generator. The resulting light frequency is set to be near-resonant with the ion's transition and can be tuned within a frequency range of about 100 MHz. The first order diffraction from AO3 is distributed to both ring-trap and linear-trap setups by sending it through single mode polarization maintaining fibers. In the linear-trap setup, light passes a high numerical aperture objective (NA=0.15) positioned about 5 cm from the trap center and about 4 mW of laser power is available for the excitation of an ion. We coupled the 1.76 μm laser light to the ions also in the ring-trap setup where we excited them through the macroscope objective, see figure 2.2. However, all the results presented in this thesis concerning the quadrupolar transition investigations were obtained solely in the linear-trap experiment, which is more convenient for realization of the measurements with two-ion crystals presented in chapter 6 due to the better control of their motion and position.

The frequency of the 1.76 μm fiber laser is stabilized to the optical cavity by the Pound-Drever-Hall technique, see schematic diagram in figure 3.4. The beam is phase modulated by an electro-optical modulator (LINOS, PM-C-BB) at a frequency of 5.4 MHz and its back-reflected part from the cavity is detected by the photodiode. The error signal is derived by mixing the photodiode output signal with the reference oscillator and sent to two PI-servo circuits. The low frequency part of the generated error signal is filtered by a 15 kHz low-pass filter and is fed back to the piezo-electric actuator inside the fiber-laser. The error signal without any frequency filtering is sent to the AO1 to compensate for the changes of the laser frequency faster than the piezo response. The bandwidth of the fast circuit is limited only by the signal delay due to the speed of sound in the acousto-optical crystal AO1 to about 1 MHz, which is much beyond the measured free-running linewidth of the fiber laser. By performing high resolution spectroscopy of the $6S_{1/2} \leftrightarrow 5D_{5/2}$ transition with a single trapped Barium ion we estimate the upper limit for the laser linewidth to be 630 ± 80 Hz, see section 3.2.4.

614 nm laser setup

In order to perform efficient sideband cooling and spectroscopy on the quadrupole $6S_{1/2} \leftrightarrow 5D_{5/2}$ transition, it is necessary to move the population of the $5D_{5/2}$ level back to the $6S_{1/2}$ manifold with high rate. For this purpose we set up a diode laser system consisting of a master laser (Toptica, DL-DFB) and a doubling cavity (Toptica, DL-SHG) with output that is resonant with the $5D_{5/2} \leftrightarrow 6P_{3/2}$ dipole transition.

The output beam of the master laser with a wavelength of 1228 nm passes through an optical isolator and is coupled into an amplifier with a tapered gain region. The measured output power is 15 mW. The reflections from an uncoated glass plate are then used to generate two beams, each with an optical power of about 0.5 mW, see figure 3.4. These beams are used for locking the master laser frequency to an optical cavity and

for measurement of its wavelength on the wavemeter, respectively. A Pound-Drever-Hall error signal is derived from the back-reflected cavity signal and fed back to the laser current. The rest of the 1228 nm laser beam pumps a second harmonic generator that provides 2 mW of light at wavelength 614 nm. 300 μW of this beam is guided to the experimental table by a single-mode polarization-maintaining fiber, where it is overlapped with the 650 nm and 493 nm laser beams and focused on the ion.

3.2.3 Quadrupolar transition spectroscopy

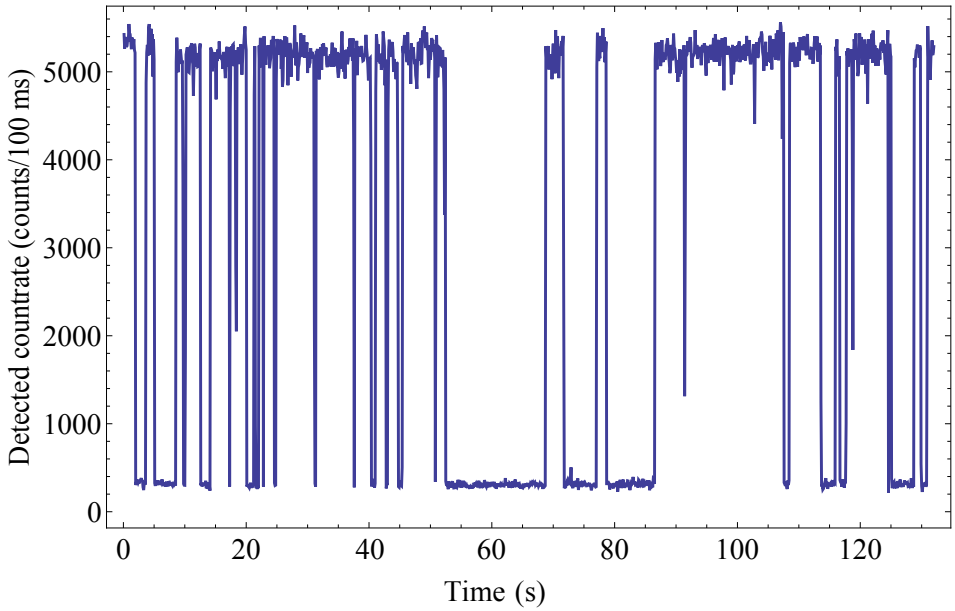

Figure 3.5: Quantum jumps on the quadrupolar transition measured on a single Barium ion.

Here we investigate the quadrupolar transition with spectroscopy methods. We first observe quantum jumps of the atomic valence electron between the metastable $5D_{5/2}$ and $6S_{1/2}$ states. Quantum jumps are usually manifested by the abrupt cessation and recovery of the fluorescence signal on a strong transition that is coupled to one of the metastable states [40,76,77]. In our case, we excite the strong dipole cooling transition $6S_{1/2} \leftrightarrow 6P_{1/2}$ and at the same time we continuously weakly probe the quadrupolar $6S_{1/2} \leftrightarrow 5D_{5/2}$ transition by a near resonant 1.76 μm laser. When the electron is excited into the metastable state, the detected fluorescence on the dipole transition abruptly disappears, and when the electron moves back to the strongly driven dipole transition the fluorescence signal recovers, see figure 3.5. The rate of the quantum jumps on the quadrupolar transition depends on the frequency detuning and spatial alignment of the 1.76 μm laser. By making this rate much higher than the detection integration time of the fluorescence on the

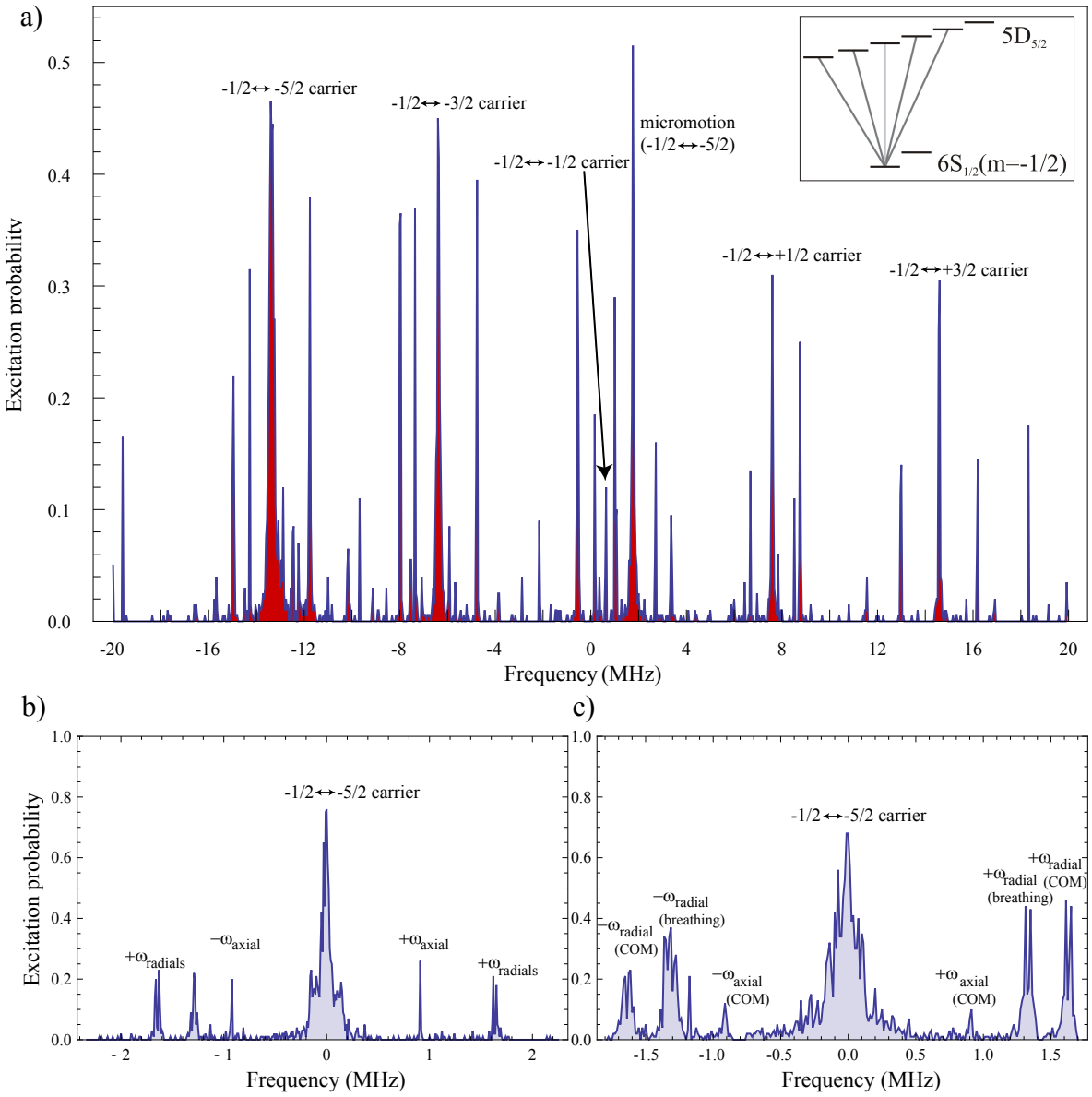

Figure 3.6: Quadrupole transition spectra. Figure a) shows a measurement of the $6S_{1/2}(m = -1/2) \leftrightarrow 5D_{5/2}$ transition spectrum, where individual carrier transitions are clearly resolved. Figure b) shows a single carrier ($6S_{1/2}(m = -1/2) \leftrightarrow 5D_{5/2}(m = -5/2)$) and the corresponding secular motional sidebands. The same measurement for a two-ion-crystal is presented in figure c).

strong dipole transition (in our case typically set to 100 ms), quantum jumps cease being resolvable in the detected count rate. Instead, the amount of detected fluorescence on the strong dipole transition per given detection time then decreases due to the finite time which the electron spends in the metastable $5D_{5/2}$ state. This measurement thus provides

a continuous signal for setting the laser driving parameters and it is sometimes referred to as observation of grey-out of quantum jumps. It is a very useful tool for maximizing the spatial coupling of the 1.76 μm laser beam to the ion and setting the parameters of the 614 nm repumping laser in the initial stage of the experiment, before the first spectroscopic measurements of the $6S_{1/2} \leftrightarrow 5D_{5/2}$ transition can be realized.

Next, we perform spectroscopy on the quadrupolar transition in the experiment, in which we measure the excitation probability on the $6S_{1/2} \leftrightarrow 5D_{5/2}$ transition as a function of the 1.76 μm laser detuning. The pulse sequence corresponds to the most simple version of the sequence presented in the figure 3.3. After Doppler cooling, the ion is optically pumped into the $6S_{1/2,(m=-1/2)}$ state and a single 1.76 μm laser pulse excites the quadrupolar transition. The electron shelving detection technique is then used for measuring the ion's state. The experiment is repeated 100 times for each frequency detuning of the 1.76 μm laser to estimate the corresponding excitation probability value.

An applied magnetic field of 4.08 Gauss lifts the degeneracy of the quadrupolar transition and spreads the measured spectrum over more than 40 MHz, see figure 3.6 a). Four carrier resonances corresponding to the $|\Delta m| = 1, 2$ transitions and their corresponding motional sidebands are clearly resolved, while the $\Delta m = 0$ transition is excited only weakly due to our geometrical configuration. The measured frequency distance between the neighboring carrier transitions is 6.9 MHz. A strong micromotion sideband corresponding to the $6S_{1/2,(m=-1/2)} \leftrightarrow 5D_{5/2,(m=-5/2)}$ carrier is due to the micromotion along the 1.76 μm laser direction. Minimizing the amplitude of this micromotion peak always seemed to increase the micromotion in the ion-mirror direction in our linear-trap setup, which is more crucial for the realized interference experiments with $6S_{1/2} \leftrightarrow 6P_{1/2}$ fluorescence photons. The relatively large measured amplitude of the micromotion peak compared to the corresponding carrier transition is partially caused also by the single-pass configuration of our 1.76 μm acousto-optical modulator AO4. Optimal diffraction efficiency of the AO4 and coupling efficiency to the single mode optical fiber leading to the trap was in the case of the presented measurements set for the center of the spectrum. The available excitation power after the single-mode fiber was then approximately three-times lower for the excitation of the outermost carrier transitions compared to the center of the spectra.

The motional sideband structure can be resolved more clearly by measuring a single carrier transition with a higher frequency resolution. Figures 3.6 b) and c) show the recorded spectrum of the $S_{1/2}(m = -1/2) \leftrightarrow 5D_{1/2}(m = -5/2)$ carrier transition for single and two ion crystals, respectively. Individual motional sidebands are clearly resolved. The irregular shapes of the carrier transition peaks are caused by the Rabi oscillations due to a finite length of the 1.76 μm excitation pulse. The measured frequencies of the secular motions are ν_{axial} =0.91 MHz, ν_{radialX} =1.62 MHz and ν_{radialY} = 1.66 MHz, respectively. The absorption strength on the radial sidebands is almost equal or noticeably

higher than on the axial motional sideband, even though they have higher frequency. This is mainly due to the orientation of principal motional axes with respect to the Doppler cooling (493 nm) and excitation (1.76 μm) laser beams, see table 2.1 for the summary of the corresponding Lamb-Dicke parameters. Coupling to higher order motional sidebands is not observed due to the very small Lamb-Dicke parameters for the 1.76 μm laser beam for all the motional modes.

3.2.4 Quadrupolar transition coherent operations

Rabi oscillations

More information about the strength and coherence of our laser-ion interaction on the quadrupolar transition can be obtained by varying the length of the exciting laser pulse.

If we neglect dissipative terms, the time evolution of the two-level atom interacting with a classical light field can be found by solving the time-dependent Schrödinger equation. This leads to the well known expression for the excitation probability $P_e(t)$ as a function of laser driving time and coupling strength Ω [78],

$$P_e(t) = \left|\frac{\Omega}{\bar{\Omega}}\right|^2 \sin^2(\bar{\Omega}t), \tag{3.7}$$

where $\bar{\Omega} = \sqrt{\Omega^2 + \delta^2}$, δ is the laser detuning and Ω is the Rabi frequency on resonance.

In the case of a single ion trapped in a harmonic potential, the coupling strength of the laser to the electronic transition strongly depends on the occupation of vibrational modes which have non-zero projection on the direction of the driving beam. By evaluation of the equation for Rabi frequency (2.8) for $m = 0$, the expression for the carrier Rabi frequency Ω_n for different motional populations n can be found [61, 79] to be

$$\Omega_n = \Omega_0 e^{-\eta^2/2} L_n^0(\eta^2), \tag{3.8}$$

where $L_n^0(\eta^2)$ is the Laguerre polynomial. The shape of the Rabi oscillations after Doppler cooling can then be calculated by averaging the time dynamics in equation (3.7) over a Boltzmann distribution of motional states with a mean phonon number value $\overline{n}$

$$p(n, \bar{n}) = \overline{n}^n/(\overline{n}+1)^{n+1}. \tag{3.9}$$

This gives rise to a dephasing mechanism of the Rabi oscillation contrast due to the simultaneous observation of flops with different frequencies between thermally populated vibrational states of the ion. The excitation probability on resonance ($\delta = 0$) as a function of time can then be expressed as

$$P_e(t) = \sum_{n=0}^{\infty} p(n, \bar{n}) \sin^2(\Omega_n t). \tag{3.10}$$

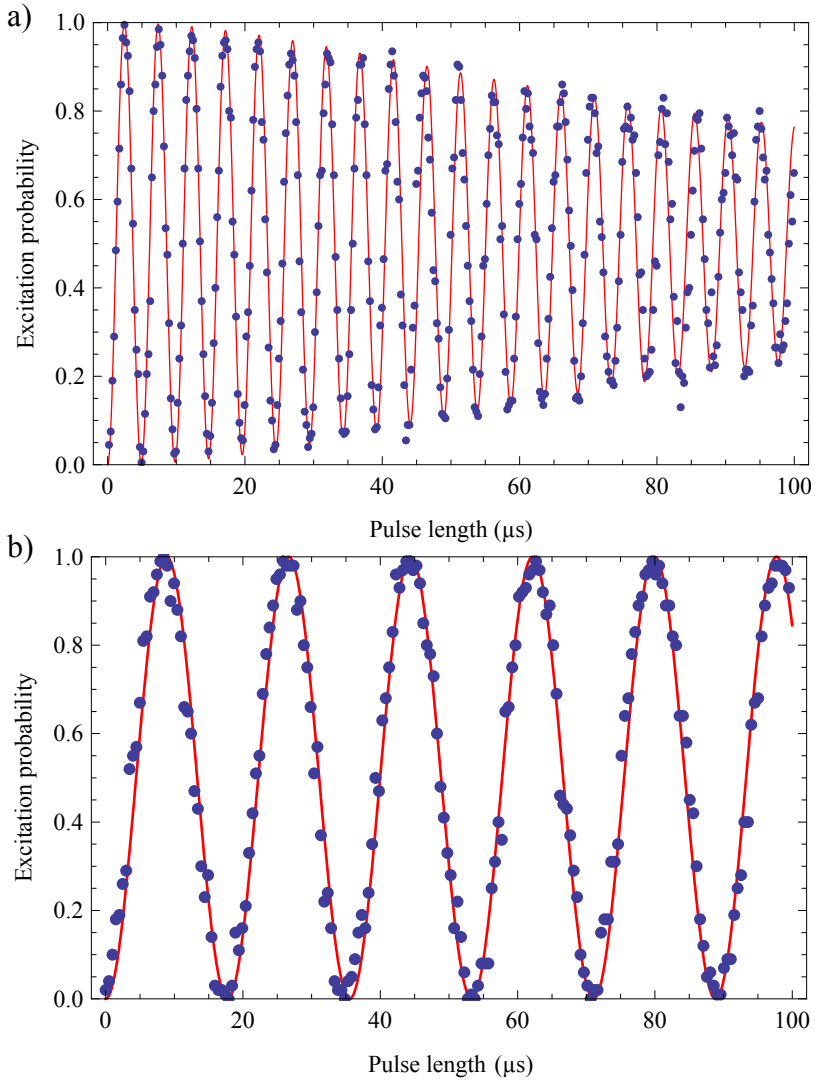

Figure 3.7: Measurements of Rabi oscillations on the $6S_{1/2,(m=-1/2)} \leftrightarrow 5D_{5/2,(m=-5/2)}$ quadrupole transition for a thermal motional state. a) The high observable number of Rabi oscillations is due to a very small Lamb-Dicke parameter in our setup. The presented data are fitted by the equation (3.11), where the main source of decoherence is the thermal occupation of the ion's motional modes. The 1.76 μm laser parameters correspond to the maximum Rabi frequency 1.29 MHz achievable with our setup. b) For optimal Doppler-cooling parameters and smaller Rabi frequencies almost no decay of the Rabi oscillation contrast is observed for up to 7 flops. The Rabi frequency estimated from the fit is 350 kHz.

By inserting the expression for the carrier Rabi frequency (3.8) into equation (3.10) and

expanding is to first order in η^2 we obtain [56]

$$P_e(t) = \frac{1}{2}\left(1 - \frac{\cos(2\Omega_0 t) + 2\Omega_0 t\eta^2\overline{n}\sin(2\Omega_0 t)}{1 + (\Omega_0 t\eta^2\overline{n})^2}\right). \tag{3.11}$$

As shown in the reference [56], this approximate solution is in a good agreement with the precise model for the times t much smaller than the time interval corresponding to $N = 1/(\pi\overline{n}^2\eta^4)$ Rabi oscillations.

Plots of typical Rabi oscillations measured in our system are shown in figure 3.7. For particular experimental settings, high contrast of the excitation to the $5D_{5/2}$ level can be observed for up to several milliseconds and more than 30 flops. Contrast at long time scales is mostly limited by the residual motion of the ion and 50 Hz noise of the magnetic field at the position of the ion.

Phase coherence measurements

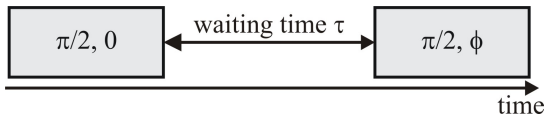

Figure 3.8: Ramsey-experiment pulse sequence.

In this section we will present experimental investigations of the phase-coherence of our quadrupolar qubit. Besides the fundamental limit on the decoherence rate set by the lifetime of the excited $5D_{5/2}$ state, the main sources of decoherence are fluctuations of the ambient magnetic field that cause the shift of energy levels via the Zeeman effect and fluctuations of the laser frequency. Random changes of the relative phase of the laser light with respect to the phase of the atomic qubit cause dephasing of an initial state prepared in some coherent superposition to an incoherent mixture.

The coherence of the atomic qubit can be measured using a Ramsey-interference experiment [80]. Two pulses with areas of $\pi/2$ and relative phase difference $\Delta\phi$ are applied to the atomic transition with a certain time delay τ between them, see figure 3.8. The first pulse creates a coherent superposition of the ground and excited states and the second pulse probes how much the phase of the atomic qubit has evolved during the waiting period with respect to the phase of the driving laser. A change of the second Ramsey pulse phase corresponds to a change of the rotation axis in the equatorial plane of the Bloch sphere. The excited state population should thus vary periodically with this phase difference if the second pulse amplitude is added coherently to the amplitude of rotation of the first pulse in the same or opposite directions. The experiment is repeated many

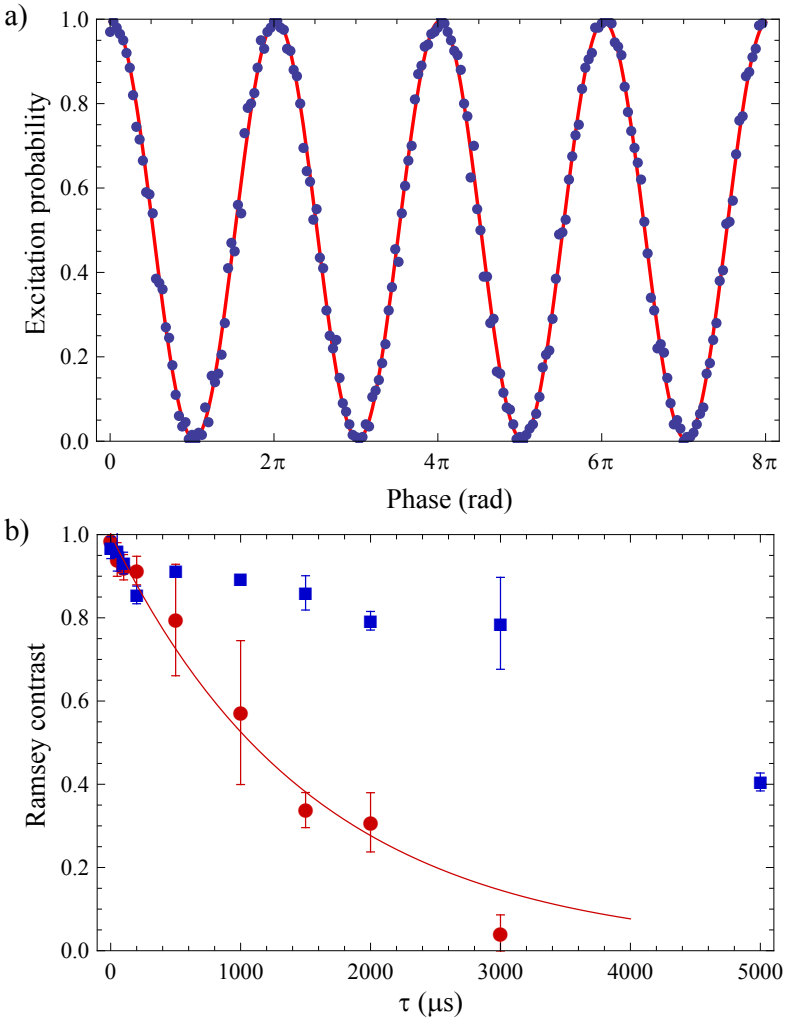

Figure 3.9: Measurements of the Ramsey interference experiments on the $6S_{1/2,(m=-1/2)} \leftrightarrow 5D_{5/2,(m=-3/2)}$ quadrupolar transition. a) Measurement of the excitation probability as a function of the second Ramsey-pulse phase ϕ with nearly unity contrast of the interference fringes for $\tau = 0$. b) Characterization of the Ramsey interference contrast as a function of the waiting time τ. For long waiting times the contrast decreases due to decoherence caused mostly by magnetic field fluctuations with 50 Hz periodicity, therefore the starting time of the experimental sequences is synchronized with 50 Hz power line (red circles). The coherence time can be further increased by using a spin-echo technique (blue squares). The error bars correspond to one standard deviation.

times, therefore any random mutual changes of the phase give rise to random probabilities of finding the ion in the ground or the excited states, which are then manifested by

a decreased contrast of the measured interference fringes.

Typical measurements of the Ramsey interference on our quadrupolar transition for $\tau = 0$ are shown in figure 3.9 a). The measured contrast of 98.7 ± 0.8 % proves the high degree of control over our single-qubit operations. For longer Ramsey waiting times τ, the measured contrast decreases due to the loss of phase coherence that is mainly caused by the large ambient magnetic field fluctuations at 50 Hz with an amplitude of about 20 mG at the position of the ion. Experimental cycles are synchronized with the power line frequency to minimize this effect so that every experimental sequence starts at the same phase of 50 Hz fluctuations. The measured decay of the Ramsey interference contrast is shown in figure 3.9 b). The red dots correspond to a measurement with power line synchronization and the exponential fit yields a coherence time of 1.6 ± 0.2 ms. Blue squares correspond to data obtained with a single spin-echo pulse applied in the middle of the Ramsey pulse sequence. This technique eliminates the effect of noise with frequency smaller than the inverse of the Ramsey waiting time. The direction of phase drift of the atomic superposition is flipped by applying an additional carrier laser pulse of length π after half of the Ramsey waiting time. The improved Ramsey decay time (> 3 ms) suggests that the main source of dephasing in our system is still coming from low frequency fluctuations, most likely corresponding to the ambient magnetic field noise.

The degree of control achieved on our quadrupolar qubit transition and coherence times reached are much beyond the requirements needed for the realization of the experiments presented in this thesis. Further improvements of our quadrupole qubit coherence times can be easily implemented by an active magnetic field stabilization system [70].

3.3 $6S_{1/2,(m=-1/2)} \leftrightarrow 6S_{1/2,(m=+1/2)}$ RF transition

The insensitivity to the motion and availability of narrow radio-frequency sources with power stability at the order 10^{-5} makes radio-frequency transitions a convenient candidate for atomic qubits. In this section we demonstrate the basic qubit operations on the $6S_{1/2,(m=-1/2)} \leftrightarrow 6S_{1/2,(m=+1/2)}$ RF-transition.

3.3.1 Introduction

For the purpose of the entanglement generation experiment presented in chapter 6 we realize a qubit on a two-level system consisting of the two Zeeman substates of the $6S_{1/2}$ level with an energy splitting $\hbar\omega_0$ introduced by a weak magnetic field $\overrightarrow{B}$ due to the Zeeman effect. This transition corresponds to a magnetic dipole transition and can be driven by an oscillating magnetic field $\overrightarrow{B_1}\cos(\omega_L t)$ perpendicular to the field $\overrightarrow{B}$. If the frequency of the applied time-dependent magnetic field is equal to the energy splitting between the two Zeeman states ($\omega_L = \omega_0$), the counterclockwise component

of $\overrightarrow{B_1}$ accompanies the spin in its Larmor precession around $\overrightarrow{B}$, whereas the clockwise component rotates at the frequency $-2\omega_L$ with respect to the spin and thus has negligible effect on it [81]. The strength of the coupling between the driving oscillatory magnetic field and the atomic transition can be conveniently expressed in the frame rotating at the frequency ω_L around the direction of magnetic field $\overrightarrow{B}$, $\Omega^{\mathrm{RF}} = \sqrt{\Omega_1 + \delta_L}$. Here $\Omega_1 = |\mu||B_1|/\hbar$ is the on-resonance Rabi frequency with μ being the magnetic dipole matrix element and $\delta_L = \omega_L - \omega_0$ is the detuning.

3.3.2 Experimental setup and sequence

Operations on the $6S_{1/2,(m=-1/2)} \leftrightarrow 6S_{1/2,(m=+1/2)}$ transition are initialized by optical pumping of the atomic population to a $6S_{1/2,(m=-1/2)}$ state by the 493 nm σ^- beam propagating along the direction of the magnetic field $\overrightarrow{B}$. The RF-transition is driven by a time-dependent magnetic field $\overrightarrow{B_1}$ with oscillation frequency equal to the energy splitting between the two states. The read-out of the RF-qubit state is accomplished by transfer of the $6S_{1/2,(m=-1/2)}$ population to the metastable $5D_{5/2}$ state using a single 1.76 μm laser pulse and by scattering and detection of the fluorescence on the dipole $6S_{1/2} \leftrightarrow 6P_{1/2}$ transition.

We generate the oscillatory magnetic field in our linear-trap setup in two different ways. We apply the RF-signal resonant with the $6S_{1/2}$ Zeeman sublevels energy splitting directly to one of the unused micromotion-compensation electrodes. This enables us to observe the spectrum of the RF-transition and demonstrate high fidelity coherent operations on the RF-qubit, however, it proved to be difficult to reach Rabi frequencies higher than 60 kHz, which are necessary for some further applications. This is mainly due to poor generation efficiency of the oscillating magnetic field using a compensation electrode consisting of a single rod perpendicular to the desired direction of the generated field. An increase of the driving RF-field amplitude in this case also causes considerable motional heating due to the generated oscillating electric field.

The second method is based on driving an LC-resonant circuit at the frequency corresponding to the Zeeman splitting induced by $\overrightarrow{B}$. The circuit consists of a coil with 8.5 cm diameter with just a single winding made out of a 1 mm thick copper wire and a 680 pF capacitor connected in parallel to it. The particular parameters were chosen to reach the resonance frequency of 11.5 MHz, which corresponds to the energy splitting between the $6S_{1/2,(m=-1/2)}$ and $6S_{1/2,(m=+1/2)}$ states for a static magnetic field amplitude of $|\overrightarrow{B}| = 4.1$ G. The LC-circuit parameters were then slightly tuned according to the measured reflection of radio-frequency power from the circuit to reach the exact desired center frequency. The reflected signal shows a 4 dB resonance dip in reflection with FWHM of about 2 MHz at the center frequency of 11.4 MHz. The coil is installed outside the vacuum chamber approximately 6 cm from the position of the ion. The RF-signal gener-

ated by the direct-digital-synthesizer or RF-generator is amplified using a 2 W amplifier (Mini-Circuits, ZHL-1-2W) and connected to the LC-circuit via an unidirectional-coupler (Mini-Circuits, ZDC-10-1+) to prevent the reflected power from reaching the amplifier. Using this setup we were able to efficiently excite the RF-transition of an ion without any observable motional heating.

3.3.3 Spectroscopy and coherent operations

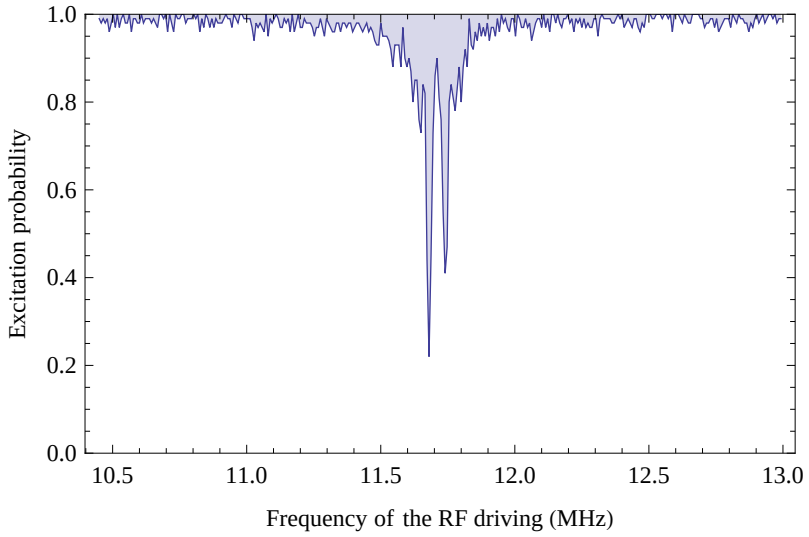

Figure 3.10: Spectrum of the $6S_{1/2,(m=-1/2)} \leftrightarrow 6S_{1/2,(m=+1/2)}$ magnetic dipole transition.

Figure 3.10 shows the measured spectrum of our magnetic dipole transition. The absence of any motional sidebands in the spectra is due to the extremely small Lamb-Dicke parameters for the wavelength of radiation corresponding to the radio-frequency signal of 11.5 MHz, which are on the order of $\eta \sim 10^{-9}$. The power-broadened carrier spectral line shows several peaks due to the Rabi oscillations even at very large length of the probing RF-pulses of 500 μs.

As can be seen in the figure 3.11-a), we were able to observe up to 80 Rabi oscillations with the decay mostly limited by the amplitude fluctuations of the static magnetic field $|\overrightarrow{B}|$. The measured data are fitted by equation (3.7) with time dependent detuning $\delta(t)$, where we assumed a Gaussian envelope of the magnetic field noise. Figure 3.11-b) shows the measurement of several Rabi flops for short lengths of the excitation pulses with almost unity flopping efficiency. The Rabi frequency estimated from the fit by harmonic function (3.7) is 419.9 ± 0.2 kHz.

We performed a Ramsey interference experiments as described in section 3.2.4 to demonstrate the phase coherence of our RF-qubit. First, we measured the Ramsey in-

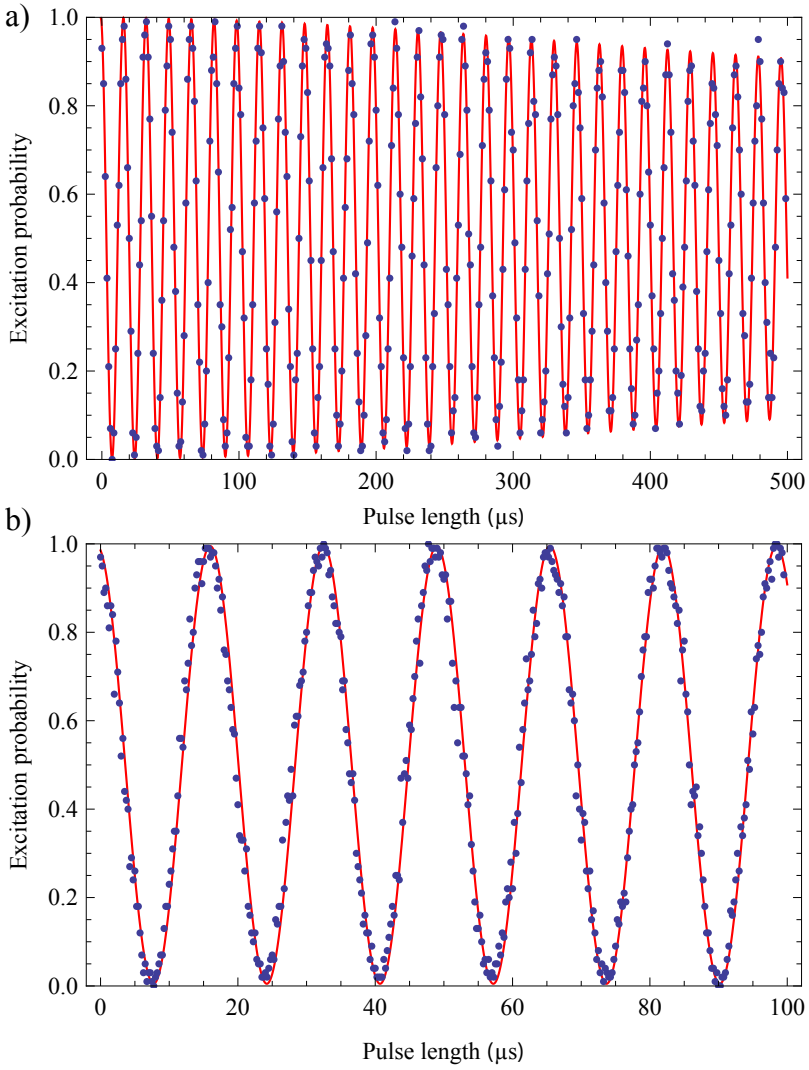

Figure 3.11: Measured Rabi oscillations on the RF-qubit transition for long a) and short time scales b). The decay is governed mostly by the ambient magnetic field fluctuations that change the energy splitting between the two qubit states.

terference contrast for zero time delay ($\tau = 0$) between the two excitation pulses, see figure 3.12-a). The measured contrast of the oscillations of 99.6 ± 0.1 % demonstrates a high degree of control of our RF-qubit limited mostly by the efficiency of the optical pumping to the $6S_{1/2}(m0 - 1/2)$ state. Next, we estimated its coherence time by observing the decay of the Ramsey contrast as a function of the time delay τ between the two Ramsey pulses, see figure 3.12-b). The presented data were taken with power-line synchronization and the Gaussian fit of the decay gives a coherence time of 280 ± 40 μs limited mostly by the residual fluctuations of the magnetic field $|\overrightarrow{B}|$.

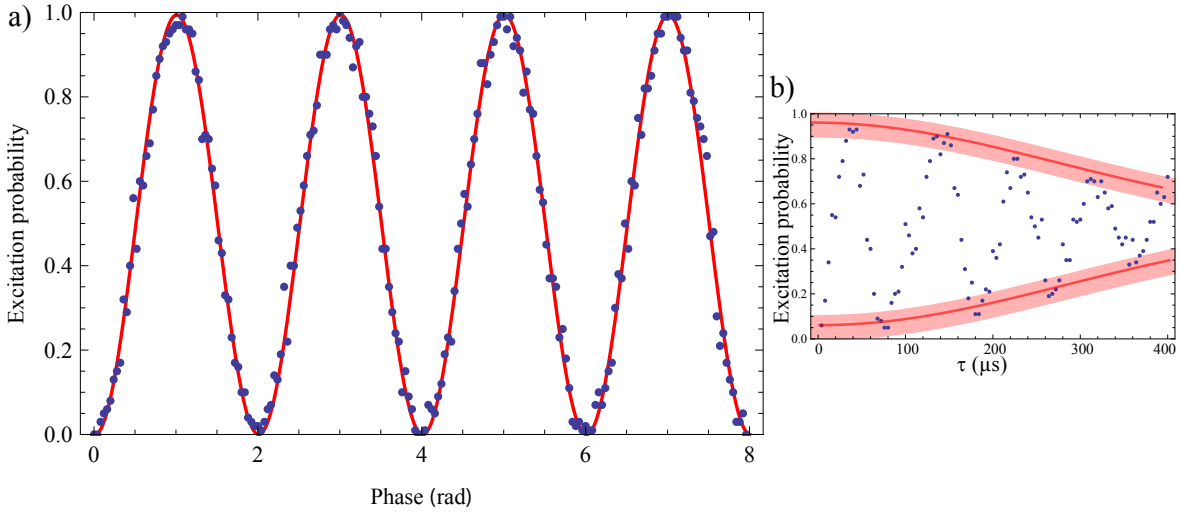

Figure 3.12: Ramsey experiments on the RF-qubit transition. a) Measurement of the excitation probability as a function of the second Ramsey pulse phase for zero time delay τ with the contrast of 99.6 ± 0.1 % proves a high fidelity of single-qubit operations in our system. b) Measurement of the RF-qubit coherence time by varying the time delay between the two Ramsey pulses.

4 Interferometric thermometry of a single ion

4.1 Introduction

We propose and experimentally test a thermometry method based on the self-interference of fluorescence photons in the half-cavity setup consisting of a single mirror [39]. The contrast of the measured interference fringe is proportional to the extension of the ion's motional wavepacket and thus it provides us with information about its temperature. We evaluate the performance of this technique by measurement of the interference contrast for different mean motional numbers estimated independently by spectroscopy methods using the 1.76 μm laser.

A part of the results and of the text presented in this chapter can be found also in the reference [66].

4.1.1 Motivation

The interaction of a single photon with a single isolated atom at rest in free space is an important model in quantum physics. Systems that enable its precise experimental investigation have become available with optically cooled atoms in harmonic potentials which can be localized to a few nanometers in position for extended periods of time [55,82,83]. Over the past decade, remarkable progress has been made in the control of the coupling of single atoms to light with important steps made in the direction of quantum networking [84–86]. In particular, single ions in Paul traps are considered today as very promising systems for such applications [87] because of the possibility of excellent control of their internal and external (motional) states [55]. Good atom localization is essential for long distance entanglement of atomic qubits relying on single photon interference [37]. On the pure quantum optics side, as one of the most fundamental processes, the quantum properties of resonance fluorescence from single trapped atoms were investigated with a high level of detail [65, 88, 89].

Precise estimation and control of atomic motion are crucial for most of these experimental investigations [90–93], and vice versa, studying the coherence properties of the light emitted by an atom can provide us with the information about its motion. Furthermore, thermometry proved to be important for measurement and understanding of the strong heating processes in the field of development of novel ion traps for quantum information processing [94, 95].

4.1.2 Thermometry methods

An atom of mass m trapped and Doppler cooled in a harmonic potential $V(z) = m\omega^2 z^2/2$ with motional frequency ω along the z-axis behaves as a quantum harmonic oscillator. Occupation probabilities $p(n, \bar{n})$ of its motional states with phonon numbers n follow the thermal distribution, see equation (3.9). The temperature T of the ion can then be defined with respect to the mean phonon number $\overline{n}$ as [96]

$$\overline{n} = 1/(\exp(\hbar\omega/k_B T) - 1), \tag{4.1}$$

where k_B is Boltzmann constant.

There are several methods available for the measurement of temperature or the mean motional energy of single trapped atoms. They can be divided according to the obtainable precision of the measured temperature and according to the binding limit in which they are applicable. Here is the brief summary of some of the most used thermometry techniques.

- Comparison of strength of motional sidebands or measurement of Rabi oscillations on them allows very precise temperature measurements in the strong-binding regime where motional sidebands are resolved [55, 97, 98]. We will use these techniques in our experiment to evaluate the performance of the new thermometry method and check its agreement with theoretical predictions. A simplified theoretical background for the measurement of temperature in the sideband resolved regime can be found in the next section.

- The ion's temperature can be estimated from fluorescence line shapes. For a two-level atom, they correspond to a convolution of Lorentzian and Gaussian functions, coming from the finite lifetime of the excited state and the thermal distribution of the motional state populations, respectively [99, 100]. The contribution of thermal broadening to the overall linewidth can be estimated from the measured fluorescence spectra with the shape of a Voigt function. This method can be particularly useful in the regime where sidebands are not resolved.

- An intuitive thermometry method which was recently tested and improved in several experiments is based on high spatial resolution imaging of the fluorescence emitted

by an ion [101, 102]. By assuming a Gaussian occupation of motional energy levels, the mean motional energy can be evaluated from the measured spatial profiles of the ion's position. However, this method can deliver resolution of single mean motional quanta only in the regime of low trapping frequencies on the order of a few hundred kHz and imposes strict requirements on the quality of the optical imaging system. The resulting spread of the measured spatial distribution corresponds to the convolution of the point-spread function of the imaging system and the extension of the motional wavefunction.

Besides these most common thermometry methods, there are several other techniques available. After proper calibration, the self-interference spectrum of the ion's fluorescence signal detected by a single-photon detector can provide information about motional sidebands amplitude and thus the temperature of an ion [103]. The mean phonon number can be also estimated using quantum limited measurement of the electromagnetically-induced-transparency phase shift from an single trapped atom [104].

4.1.3 Thermometry in the sideband-resolved regime

A comprehensive overview of thermometry techniques based on the precision spectroscopy in the sideband-resolved regime can be found for example in [55, 56]. Here we will briefly introduce the two basic methods which we later employ in the phase-interference thermometry experiment.

Time evolution of the Rabi oscillations on the blue sideband transition

The mean phonon number in a particular motional mode in a sideband-resolved regime can be estimated by observation of the time evolution of the internal atomic state population when driving the motional sidebands. By assuming the thermal distribution of the motional states of the ion in a given motional mode (eq. 3.9), the probability of driving the ion into the excited state as a function of the length of the excitation pulse resonant with the first blue motional sideband frequency can be found as [55, 56]

$$P_e(t) = \sum_{n=0}^{\infty} p(n, \bar{n}) \sin \Omega_{n,n+1} t. \tag{4.2}$$

Here $\Omega_{n,n+1}$ is the Rabi frequency on the blue sideband transition in the Lamb-Dicke regime for the phonon number n as defined in equation (2.10). A mean phonon number $\bar{n}$ and thus the temperature of an ion can then be estimated from the fit of the measured time evolution using the equation (4.2).

Comparison of the coupling strengths

The temperature of the ion after Doppler cooling can be estimated by comparison of the coupling strength of the laser field to the red and blue motional sidebands. This method is precise especially for very cold ions, where the asymmetry between the excitation strengths becomes large. The strength of coupling on the first red sideband is proportional to $\eta^2\overline{n}$, while the strength on the first blue sideband is proportional to $\eta^2(\overline{n}+1)$, see equation (2.10). The coupling to the red sideband for $\overline{n} \to 0$ vanishes, because no more quanta of motional energy can be extracted from the ion. The relation between the ratio of excitation probabilities on the red and blue sidebands $R = P_e^{\mathrm{red}}/P_e^{\mathrm{blue}}$, mean photon number in given motional mode $\bar{n}$ and the probability of finding the ion in the lowest $(n = 0)$ motional state P_0 can be found to be, respectively [55],

$$\bar{n} = \frac{R}{1-R} \qquad \text{and} \qquad P_0 = 1 - R. \tag{4.3}$$

The ratio R can be estimated either directly by the weak incoherent driving of the two sidebands for a given time and measurement of the corresponding excitation probabilities, or by measurement and comparison of the areas below the sidebands. This method can be easily extended to measurements of the ion's temperatures corresponding to higher phonon numbers by probing the excitations on the higher order motional sidebands. The order of the sideband should be chosen to be the integer number nearest to the mean phonon number $\overline{n}$ to maximize the precision of the temperature estimation [105].

4.2 Sideband cooling of a single Barium ion

Sideband cooling is a crucial tool for characterization of our thermometry method in the regime of sub-Doppler temperatures. Here we implement a sideband cooling technique using the 1.76 μm laser on the $6S_{1/2} \leftrightarrow 5D_{5/2}$ quadrupolar transition. It allows us to cool the ion close to its motional ground state and thus enables studies of interference effects with the ion's fluorescence with much higher precision.

4.2.1 Theoretical background

The cooling process in the resolved-sideband regime has been described in detail in several theoretical and experimental works [41, 55, 106–108]. Here we restrict ourselves to a description of the basic working principle, pulse sequence and optimization procedure used in our linear-trap experimental setup to sideband cool individual motional modes of a single Barium ion.

The principle of laser cooling of a two-level atom in the resolved sideband regime is described in figure 4.1 a). Here ω_0 is the resonance frequency of the cooling transition and

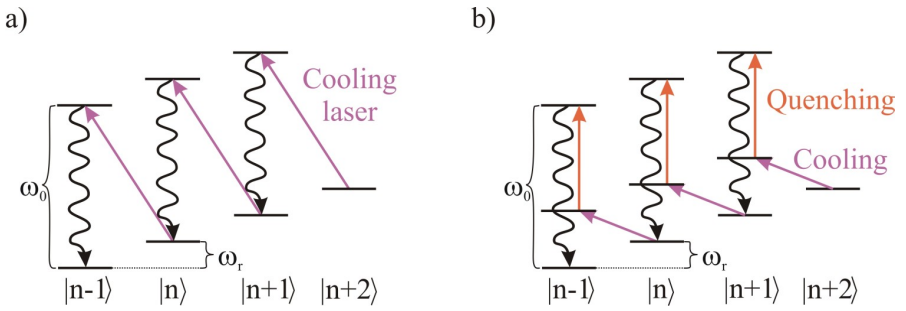

Figure 4.1: a) Depiction of the basic principle of sideband cooling. Each excitation on the red sideband and emission of the photon on the carrier transition removes a single quanta of motional energy. b) To decrease a time needed for a single cooling cycle, the excited metastable state can be quenched by an additional laser field to a third atomic level which decays back to the electronic ground state with a high rate.

ω_r is the secular frequency of the atomic motion in a harmonic potential $V = m\omega_r^2 r^2/2$ along the normal spatial mode of the motion r. As described in equation (2.9), the absorption and emission spectra have resolved components at the frequencies $\omega_0 + n\omega_r$, where n is an integer. The cooling process consists of exciting the atom by a narrowband laser tuned to the first lower sideband ($n = -1$) that corresponds to an absorption of the photon of frequency $\omega_0 - \omega_r$ and emission of a photon of average frequency ω_0 on the carrier transition ($n = 0$). In this process, each scattered photon reduces the atom's vibrational energy on average by one motional quantum.

For a two-level atom moving as a harmonic oscillator, the necessary condition for sideband cooling is that the linewidth Γ of the employed transition is much smaller than the motional frequency ω_r. For typical dipole allowed transitions this condition is not satisfied, because the spontaneous decay rate is typically much higher (several tens of MHz) than the trap frequency (usually a few MHz). This can be solved either by increasing the trap frequency, or by employing an atomic transition with small spontaneous decay rate. The usual approach is to use a very narrow, typically quadrupolar transition with a linewidth of a few Hertz. Since the typical heating rates of the trapped ions are of the same order of magnitude or much higher as the corresponding lifetimes [95, 98, 108, 109], the cooling scheme depicted in figure 4.1-a) using these transitions would not be practically possible. The metastable state must therefore be quenched by an additional laser field to the third atomic level which decays to the ground state with a high rate, see figure 4.1-b). This effectively creates a two level system with a fast decay channel in the regime where motional sidebands are resolved by the cooling laser. For high Rabi frequencies of the cooling laser it is necessary to compensate for the dynamical ac Stark shifts coming from off-resonant interaction of the laser with the carrier transition.

In the absence of other strong sources of heating, like fluctuating patch-potential noise or thermal electronic noise [105], there are two dominant processes which decrease the efficiency of the sideband cooling [55]:

- off-resonant excitation of the carrier transition and de-excitation on the first blue motional sideband,
- off-resonant excitation of the blue sideband and emission of the photon on the carrier transition.

The heating rates due to both processes are typically of the same order. However, for cooling the axial motion of the Barium ion in our linear trap, the heating due to off-resonant excitation of the carrier is 210 times more probable than heating due to off-resonant excitation of the blue sideband transition. This is mainly due to the large difference between Lamb-Dicke parameters on the excitation ($6S_{1/2} \leftrightarrow 5D_{5/2}$, $\eta = 0.0086$) and de-excitation ($6P_{3/2} \leftrightarrow 6S_{1/2}$, average $\eta \sim 0.063$) transitions caused by a difference of the transition wavelengths and by alignment of the 1.76 μm excitation beam with respect to axis of the axial motion, see chapter 2.3.3.

4.2.2 Experimental realization

Optimal Doppler cooling by a red-detuned excitation of the dipole transition gives a mean phonon number corresponding to a Doppler limit temperature $T_{\min} \sim \hbar\Gamma/(2k_B)$ [56]. For the axial motion of a single Barium ion in our linear trap and Doppler-cooling with the 493 nm laser on the $6S_{1/2} \leftrightarrow 6P_{1/2}$ transition this gives $\overline{n} \sim 10$, see equation (4.1). In order to cool an ion closer to the motional ground state, we use a sequence of 1.76 μm laser excitations on the quadrupolar $6S_{1/2} \leftrightarrow 5D_{5/2}$ transition resonant with the first red sideband, which should in principle provide a reduction of the mean phonon number down to the ground state of ion's motion. To enhance the speed of these excitation and decay cycles we apply the 614 nm quenching laser together with the 1.76 μm laser. The cooling speed is then directly proportional to the Lamb-Dicke factor for the 1.76 μm laser beam for the axial motional mode [108], see table (2.1). This gives an estimated ground state cooling time of about 14 ms for a starting mean phonon number of $\overline{n} = 10$ and carrier Rabi frequency of about 500 kHz.

When performed on the $S_{1/2,(m=-1/2)}$-$D_{5/2,(m=-5/2)}$-$P_{3/2,(m=-3/2)}$ levels, the sideband cooling process is a quasi-closed cycle. Short pulses of 493 nm σ^+ light must be applied every 200 μs on the ion to depopulate the $S_{1/2,(m=+1/2)}$ level that might eventually get populated due to a decay from the $6P_{3/2}$ down to the $5D_{3/2}$ level or to the other $5D_{5/2}$ Zeeman sub-levels, see figure 4.2.

A 1.76 μm laser pulse is finally applied to estimate the mean photon number after sideband cooling by one of the described thermometry methods. Figure 4.3 shows scans

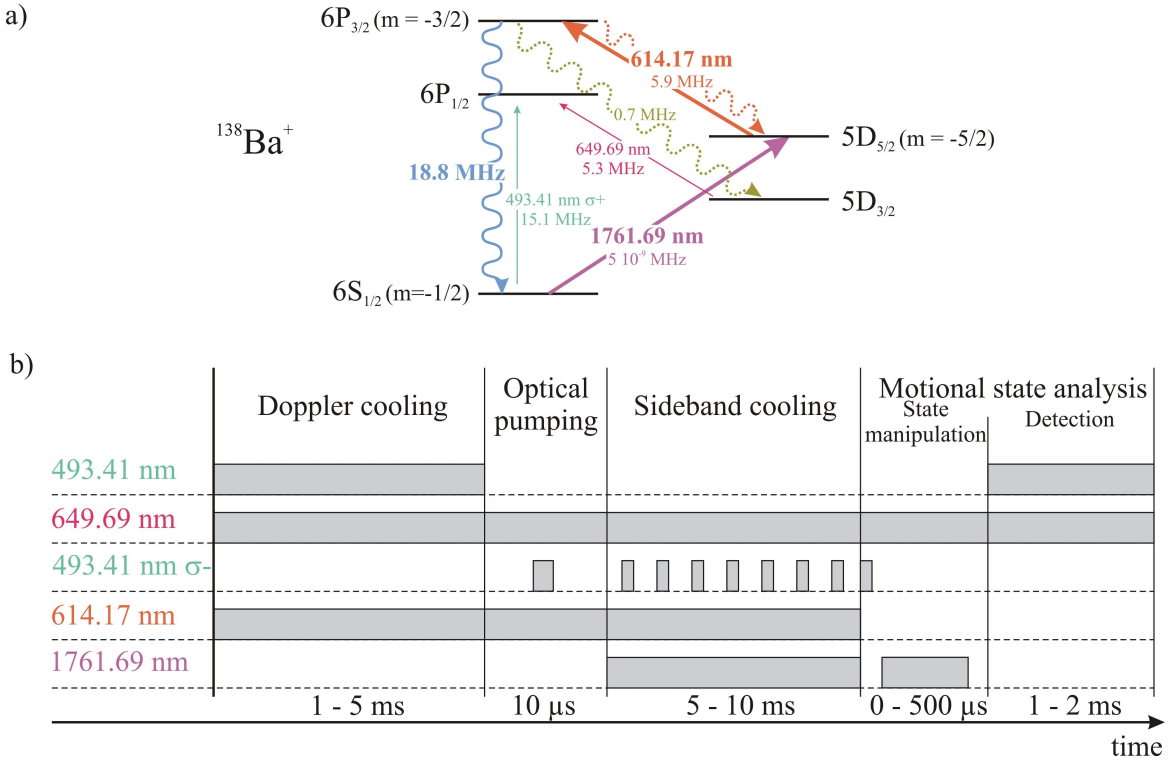

Figure 4.2: a) Electronic transitions involved in the sideband cooling of a Barium ion. The quasi-closed cooling cycle on the $6S_{1/2,(m=-1/2)}$-$5D_{5/2,(m=-5/2)}$-$6P_{3/2,(m=-3/2)}$ cooling transition is disturbed by unwanted decay channels (dashed) from the $P_{3/2,(m=-3/2)}$ state. b) Experimental sequence for sideband cooling.

of the mean excitation across the red and blue axial motional modes. Figure 4.3-a) (and b)) shows the red (and blue) axial sideband (i) before and (ii) after sideband cooling for 10 ms. The clear reduction of the area under the red sideband shows that the mean photon number has been greatly reduced. As described in section 4.1.3, from the measurements of the ratio R between the red and blue sideband areas we estimate a mean photon number after sideband cooling of $\bar{n} = 0.03$ which gives $P_0 = 97\,\%$. The sideband cooling speed and efficiency are mainly limited by the small Lamb-Dicke factor η on the $6S_{1/2} \leftrightarrow 5D_{5/2}$ quadrupolar transition. Increasing the 1.76 μm laser Rabi frequency helps only up to the point where excitations on the red sideband contributing to sideband cooling start to compete with strong heating processes coming from the off-resonant carrier excitations. We performed the evaluation of the efficiency of our sideband cooling also by thermometry based on the measurement of the time evolution of excitation probability on the blue motional sideband. Figure 4.4-a) shows the measured Rabi oscillation on the blue sideband of the axial motional mode after Doppler cooling. The estimated mean photon number from the fit using the equation (4.2) is $\bar{n} = 8.2$. Figure 4.4-b) shows a

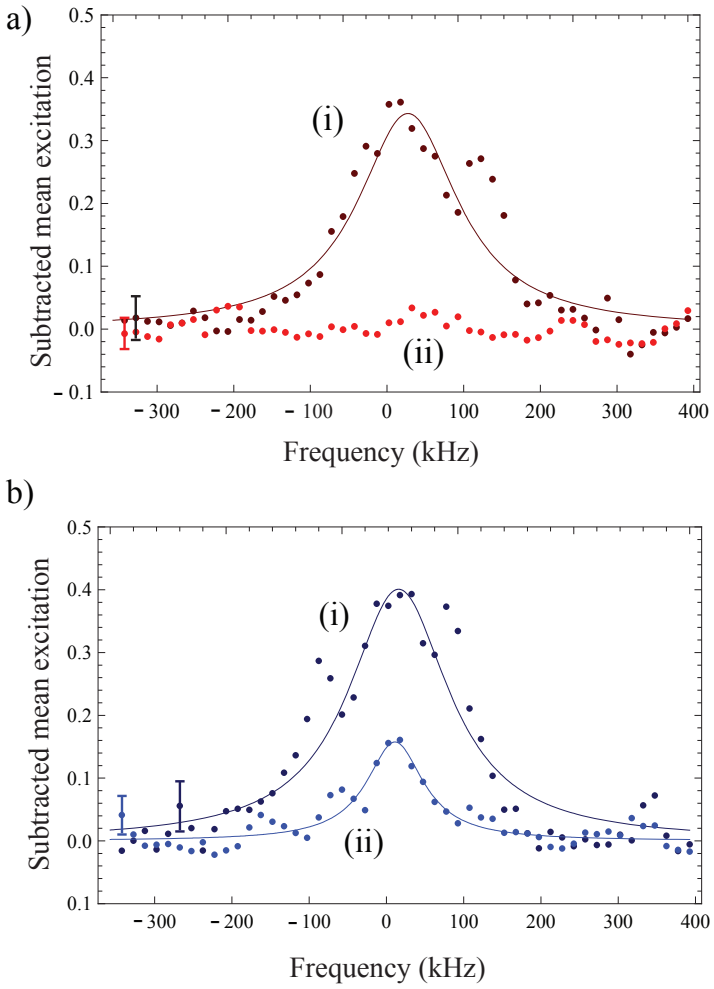

Figure 4.3: Comparison of the coupling strengths to red and blue axial sidebands. The measured mean excitation of the a) red and b) blue sideband are plotted (i) before and (ii) after sideband cooling. The error bars correspond to one standard deviation.

typical Rabi oscillation on the blue sideband after sideband cooling for 7 ms, resulting in a mean phonon number of $\bar{n} = 0.2$. We performed sideband cooling close to the motional ground-state also for both radial motional modes where a mean phonon number of $\bar{n} = 1.1 \pm 0.2$ is readily obtained for the sum of the two radial modes.

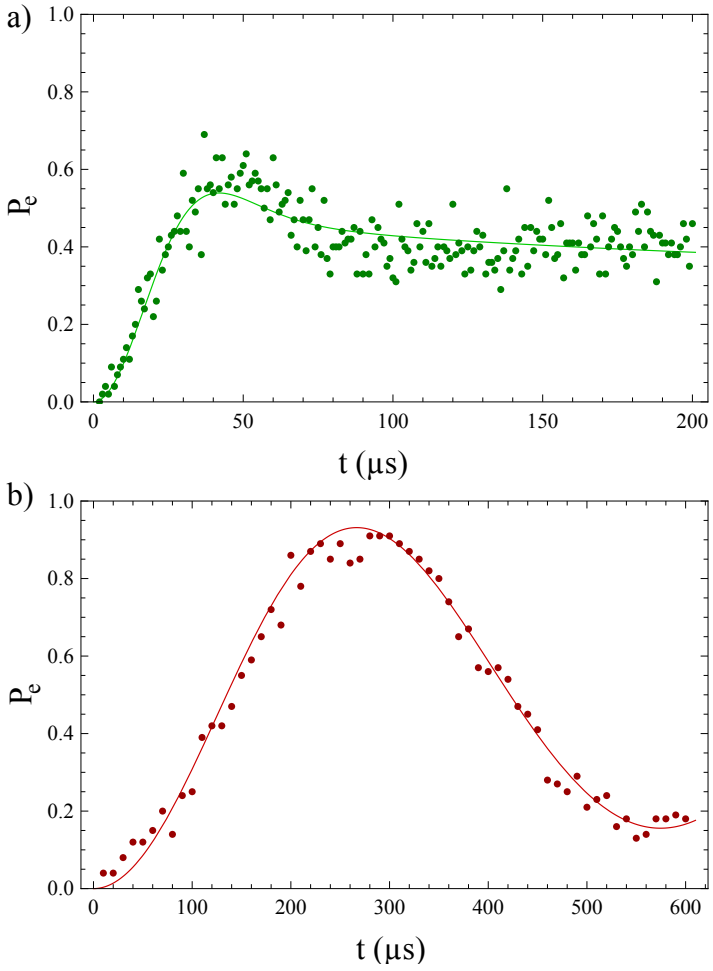

Figure 4.4: Examples of the estimation of the mean phonon number by measurement of the time evolution of the excitation probability P_e on the blue sideband transition for the axial motional mode. Figures a) and b) show the measured Rabi oscillations after Doppler and sideband cooling close to the motional ground state, respectively.

4.3 Interferometric thermometry

4.3.1 Description of the experiment

We make use of the interferometric setup [39] to estimate the mean phonon number of a single ion in its radial modes of motion. Using the quadrupolar transition for sideband cooling of the ion and for independent estimation of the mean phonon number allows us to study the self-interference contrast of the ion fluorescence for very low temperatures.

Any motion of the ion modulates the phase of the emitted light which results in a modulation of the light intensity detected on the PMT in the interference setup depicted

in figure 4.5. Considering the trapped ion as a quantum harmonic oscillator [110], the detected intensity will then be given by

$$\begin{aligned} I(t) &= I_0(1 + V_0 \sum_{n_x,n_y} P_{n_x} P_{n_y} \langle n_x, n_y| \\ &\quad \cos[2kL + 2k(\hat{x}\cos\theta + \hat{y}\cos\theta' + A_m \cos(\Omega_{RF} t))]|n_x, n_y\rangle), \end{aligned} \tag{4.4}$$

where I_0 is the mean fluorescence rate in counts/sec, V_0 is the visibility of the interference fringes due to imperfect optics and acoustic noise on the mirror path and k is the wavevector of the 493 nm light. The operators $\hat{x}$, $\hat{y}$ correspond to the position operators of the ion along the respective trap axes, both of which make an angle $\theta = \theta' = \pi/4$ with respect to the mirror-detector direction, see figure 2.3-b). Note that we neglected the contribution of the axial motion to the reduction of the interference contrast because it is perpendicular to the detector-mirror axis. Probabilities P_n correspond to the thermal distribution defined in equation (3.9). A_m and Ω_{RF} are the amplitude and frequency of the residual micromotion along the detector-mirror axis, respectively. The change of the macromotion amplitude due to the inherent micromotion is on the order of $q\sigma$, where q is the stability parameter of the trap and σ is the standard deviation of the ion's position. It is defined as

$$\sigma^2 = (2\overline{n} + 1)\langle 0|x_M^2|0\rangle. \tag{4.5}$$

For our linear trap $q \approx 0.15$, so this effect is always negligibly small compared to σ and thus we will neglect it here. The micromotion that we consider is due to unwanted dielectric patches that displace the ion from the RF null. Although it was compensated for to a large extent by minimizing the correlation signal between scattered light and the radio-frequency drive [111] and by further optimizing the fringe contrast, it can still increase the motional amplitude by a few nanometers.

As shown in figure 4.5, a single mode fiber was used to collect both the direct and retro-reflected fields. Optical abberations due to the overall imaging system are thus reduced to a large extent. If distortions of the wavefront on the mirror path are too large however, the fringe contrast will be reduced due to a power mismatch. To ensure that the retro-reflected field has the same intensity as the direct field, we lower the direct field coupling efficiency to the fiber by a slight misalignment of the fiber coupler in order to exactly match these aberration-induced losses. We estimated these losses to be $\approx 40\%$. Realigning the mirror channel through the new spatial mode defined by the fiber thus ensures that the fringe contrast does not depend on abberations at the cost of a lower total count-rate. The possible contributions to the visibility are then micromotion, radial motion of the ion and acoustic noise on the mirror path. The latter is thus the only contribution that we insert into the prefactor V_0.

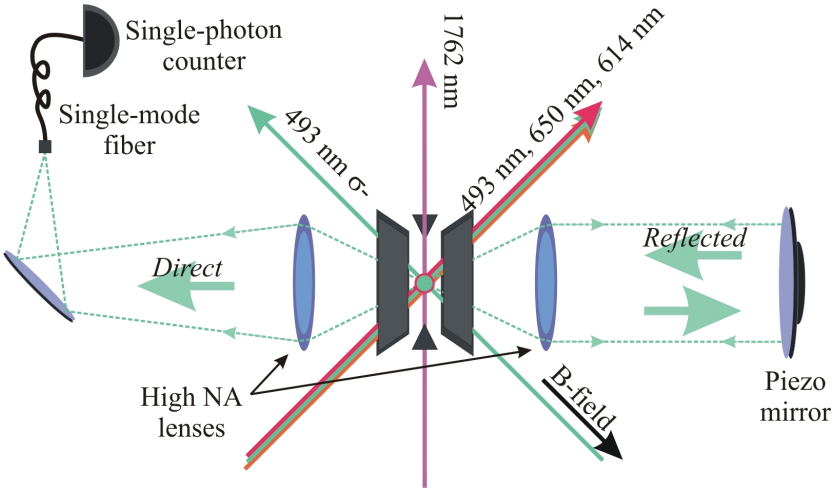

Figure 4.5: Schematic setup of our interferometric thermometry experiment. Fluorescence emitted by the ion interferes due to the indistinguishability of direct and mirror paths to the single photon detector. The interference contrast depends strongly on the ion's radial motion, which effectively changes the relative phase of the interfering wave packets on the time-scale of the motional frequency. The temperature of the ion is estimated also by means of spectroscopic techniques on the quadrupolar $6S_{1/2} \leftrightarrow 5D_{5/2}$ transition using the 1.76 μm laser to evaluate the performance of our thermometry method.

Writing $|n_x, n_y\rangle$ in the spatial eigen-basis of the harmonic oscillators and averaging the coherent micromotion amplitude over the detection period, we found that the total visibility is

$$V = V_0 J_0(2kA_m) e^{-2(k\sigma)^2}, \tag{4.6}$$

where σ is in our case 4.6 nm for the radial motional amplitude in the ground state. J_0 is the zero-order Bessel function. We assumed here that the radial modes are degenerate ($\overline{n} = \overline{n_x} = \overline{n_y}$). The finite extension of the ground state wavepacket reduces the fringe contrast by 1.4%.

4.3.2 Results

We now experimentally determine the dependence of the fluorescence self-interference visibility on the ion's motion. A plot of the fringe contrast as a function of the mean phonon number is shown in figure 4.6. For the three experimental points close to the ground state (shaded area), the mean phonon number was varied by changing the sideband cooling time. We apply a sequence of pulses for sideband cooling and then probe the fringe contrast using a weak 100 μs-long 493 nm laser pulse. The added mean phonon

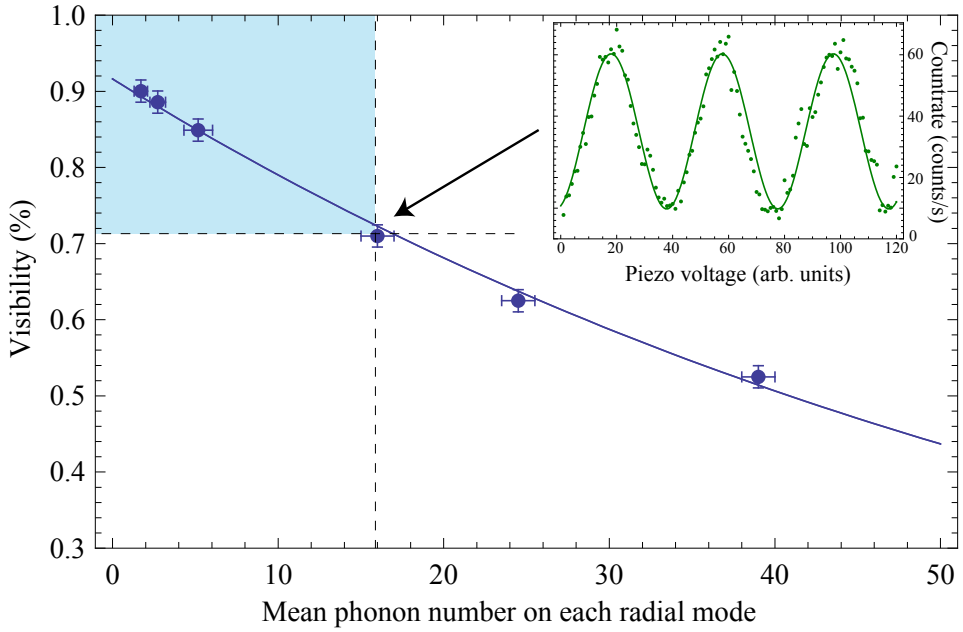

Figure 4.6: Dependence of the visibility on the mean phonon number in the radial modes. The error bars correspond to one standard deviation. The solid line is a theoretical fit using equation (4.6). The inset shows the fluorescence intensity as a function of the mirror position for a mean phonon number of $\bar{n} = 16$. The shaded area highlights the points where the ion was cooled below the Doppler limit.

number close to the motional ground state was measured to be about 0.5 due to this probe laser pulse. The mean phonon number was evaluated by comparing areas of the first red and blue motional sidebands of the quadrupolar transition spectrum, as described in section 4.1.3. This measurement method is however not accurate for large mean phonon numbers, where the ratio of the areas does not differ significantly anymore. The three other experimental points were measured only after Doppler cooling. Higher mean phonon numbers were reached by increasing the power of 493 nm laser, what corresponds to less efficient Doppler cooling conditions. To estimate the mean phonon number there, we chose to fit Rabi oscillations on the blue radial sideband.

Figure 4.6 shows that a clear increase of the fringe contrast is observed as the ion gets closer to the motional ground state and a maximum of 90% was observed for a mean phonon number of 1.1 on both radial modes. The fringe contrast is seen to depend dramatically on the ion's secular motion, so that single phonon resolution is readily achieved using this technique. The solid line shows a fit using equation (4.6) where $V' = V_0 J_0(2kA_m)$ is the only fitting parameter. Using $V' = 0.9$, the theory well reproduces well the measured data. The difference between the 99% contrast expected for a ground-state

cooled atom and the maximal observed value of 90% can thus be explained by residual micromotion and acoustic noise on the mirror.

4.3.3 Conclusion

The strong dependence of the interference contrast on the ion's motional amplitude and achieved resolution of about 1 phonon suggest possible applications of our thermometry method for ion trapping experiments. In the ideal case, the fundamental limit to the measurement of ultra-low atomic temperature is imposed solely by the fluorescence shot noise and by a small uncertainty due to the heating induced by the weak laser pulse necessary to probe the self-interference contrast. Compared to the measurement of the mean phonon number using spectroscopy methods in sideband-resolved regime, our technique might be often much easier to realize as it does not rely on complicated laser sequences, sideband-resolved regime and ultra-narrow laser sources. The presented interferometric thermometry method can be used for precise probing of the temperature of both Doppler and sub-Doppler cooled atoms.

5 Controlling the extinction from a single atom

5.1 Introduction

The efficient transfer of quantum information between atoms and photons requires controlled photon absorption with a very high probability. The requisite strong coupling can be achieved, for example, using high-finesse cavities [24–26] or large atomic ensembles [27–29], which are the most studied routes towards such goals.

The coupling of radiation to a single atom in free space is generally considered to be weak, however, technological advances, as nowadays available with large aperture lenses and mirrors [30, 31], recently led to reconsider this point of view. Novel experiments demonstrated extinctions of about 10% from single Rubidium atoms [32], single molecules [33–35] and quantum dots [36]. A light phase shift of one degree has been measured by tuning an off-resonant laser to a single Rubidium atom [112] and non-linear switching was demonstrated with a single molecule [113]. More recently, a phase shift of more than one radian has been measured from a single Ytterbium ion positioned in the focus of a high numerical aperture Fresnel lens [114]. These experiments demonstrate first steps towards quantum optical logic gates, quantum memories with single atoms and deterministic entanglement generation between single atoms in free space. However, there are still many open questions related to the coherence and efficiency of coupling to single atoms in a free-space and limitations imposed by the realistic high-NA optics and atomic motion which need to be overcome.

The aim of our extinction experiments is to examine the interaction of a weak coherent beam and a single ion mediated by a single high numerical aperture lens. The strong confinement offered by Paul traps, the readily available sideband-cooling techniques and the ability to perform efficient and deterministic quantum gates [115] make trapped-ion systems a good candidates for achieving high extinction/absorption efficiencies and thus enable practical scalability of quantum communication networks [90, 116].

Electromagnetically induced transparency

Electromagnetically induced transparency (EIT) has been a phenomenon specific to optically thick media consisting of ensembles of many atoms [117], where both the optical fields and the atomic states are modified. However, quantum information processing requires single well-defined qubits, e.g. single atoms, that can be individually manipulated to perform deterministic quantum gates. In single atom experiments, the related effect of coherent population trapping has been observed on the fluorescence field, which reveals modifications of the atomic population, but leaves the transmitted optical fields without significant change. The feasibility of EIT from a single atom in free space thus still remains to be shown for the first time as a part of this thesis.

The EIT is already widely used to control the absorption of weak light pulses or single photons in atomic ensembles [28, 29, 118, 119] and in high-finesse cavities [120]. A single-atom system based on this technique could easily be used as an efficient single atom switch, or as a programmable phase shifter of a weak coherent beam or a single photon field.

Single-atom as a mirror

Besides the two processes of absorption and emission of photons, coupling of radiation to atoms raises a number of questions that are worth investigating for a deeper theoretical and thus interpretational insight. The modification of the vacuum by boundaries is amongst the most fundamental problems in quantum mechanics and is widely investigated experimentally. In quantum optics, most studies make use of optical cavities that modify the vacuum-mode density of the field around atoms to change their emission properties [24–26, 90, 121]. Another more recent research area investigates the direct coupling of tightly focussed light to atoms in free space, using high numerical aperture elements [30, 31, 33, 36, 113, 114, 122].

By combining our half-cavity setup [39, 92] with the free space coupling of a weak coherent beam to a single ion we realize a first step towards merging these two fields, the field of cavity QED and free-space coupling. In a combined atom-mirror system, the atomic coupling to the probe is modified by a single mirror in a regime where the probe intensity is already significantly altered by the atom without the mirror. Absorption spectroscopy enables us to measure the first-order coherence between the driving laser and the back-scattered light and thus to estimate the amplitude of the coherently back-scattered field.

A part of the results and of the text presented in this chapter can be found also in the references [123] and [93].

5.2 Extinction from a single atom

This section presents a simple theoretical description and experimental realization of interaction between a single Barium ion and a weak resonant laser beam in a regime, where a substantial part of this beam is affected by the atom.

5.2.1 Theoretical model

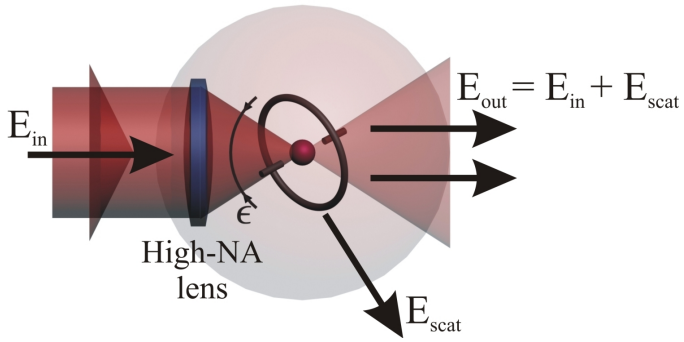

Figure 5.1: Extinction from a single atom in free space. The transmitted part of the weak probe field destructively interferes with the forward scattered part, which gives rise to an extinction of the beam intensity in the forward direction. The relative phase difference of π between the transmitted light field and the field scattered from the atom in the forward direction corresponds to the sum of two contributions, the Gouy phase shift of $\pi/2$ and the phase shift of $\pi/2$ due to the scattering of the light field on resonance [33].

In the following we present a simple theoretical description of extinction/reflection of a weak probe from a single atom. It uses a perturbative input-output formalism to relate the incoming field, $\hat{a}_{\text{in}}$, and the outgoing field, $\hat{a}_{\text{out}}$, through their interaction with the atom [124]. In the Markov limit this gives

$$\hat{a}_{\text{out}}(t) = \hat{a}_{\text{in}}(t) + i\sqrt{2\gamma_{\text{in}}}\hat{\sigma}(t), \tag{5.1}$$

where $\hat{\sigma}(t)$ is the atomic coherence and γ_{in} is the effective coupling of the input to the atom. γ_{in} can also be expressed by the total decay rate of the excited state γ and the fraction ϵ of the full solid angle covered by the incoming field as $\gamma_{\text{in}} = \epsilon\gamma$. Solving the two-level atom Bloch equations in the weak excitation limit, and in steady state, gives

$$\hat{\sigma} = i\sqrt{2\gamma_{\text{in}}}\hat{a}_{\text{in}}/(\gamma + i\Delta), \tag{5.2}$$

where Δ is the frequency detuning of the probe from the excited state. The transmission of the intensity of a probe field finally reads

$$T = |1 - 2\epsilon\mathcal{L}(\Delta)|^2, \tag{5.3}$$

where $\mathcal{L}(\Delta) = \gamma/(\gamma + i\Delta)$ for a two level atom, see reference [124] for details of the calculation. This theory predicts full reflection of the probe field for a weak resonant input field covering half of the full solid angle.

One important point here is the interference between the incident beam and the radiated dipole field, which yields a considerable decrease in the forward mode amplitude [33, 125], see figure 5.1. Using our numerical aperture NA=0.4 (i.e $\epsilon = 4\%$), we expect a probe beam extinction of 16% using equation (5.3). More refined models were proposed in [32, 33, 126] using a decomposition into cylindrical modes and including the dipole emission pattern. This set of modes is adapted to the coupling of the input beam with a high numerical aperture lens beyond the paraxial approximation. From the model of [32], we expect our extinction to be around 13%. We note that for efficient information transfer between a single photon and a single atom, i.e. efficient change of the atomic states population by a single photon, the full dipole radiation pattern and the reversed temporal mode of the atomic emission have to be matched by the single photon input mode [31].

5.2.2 Extinction experiment and results

Our experimental set-up is depicted in figure 5.2-a). A single Barium ion trapped in a ring Paul trap is our single-atom reflector. The ion is continuously cooled on the $6S_{1/2} \leftrightarrow 6P_{1/2}$ transition by the 493 nm laser that is red detuned by 50 MHz with respect to the resonance. The cooling beam intensity is set far below saturation to minimize depopulation of the $6S_{1/2}$ state, yet allowing cooling to the Lamb-Dicke regime. The saturation parameter $S = \Omega^2/(\gamma^2 + \Delta^2)$ for the 493 nm cooling beam obtained by fitting the four dark resonances in the fluorescence spectrum is about 0.1. Here, Ω, γ and Δ are the Rabi frequency, spontaneous decay rate and the laser detuning of the considered transition, respectively. Atomic population from the $5D_{3/2}$ manifold is recycled by the 650 nm beam (repumper), red detuned by 35 MHz and operated with a saturation parameter of about 0.8. For this configuration of the laser intensities and frequencies, solutions for the atomic populations in steady state using 8-level optical Bloch equations show that 70 % of the atomic population is in the $S_{1/2,(m=+1/2)}$ Zeeman sublevel.

The weak probe beam is frequency-shifted with respect to the cooling beam by an acousto-optic modulator and spatially filtered using a single-mode fiber (SMF) to guarantee a Gaussian spatial profile. Its polarization is adjusted by a quarter-wave plate for efficient elastic scattering on the $6S_{1/2,(m=+1/2)} \leftrightarrow 6P_{1/2,(m=-1/2)}$ transition. A crucial part in the extinction experiment is achieving a high spatial overlap between the incoming probe beam and the dipole emission pattern. The mode-matching is done using an expanding telescope (Beam Expander 2x-10x, Jenoptik Optical Systems GmbH) and a custom-designed objective with a numerical aperture of 0.4, see description of the

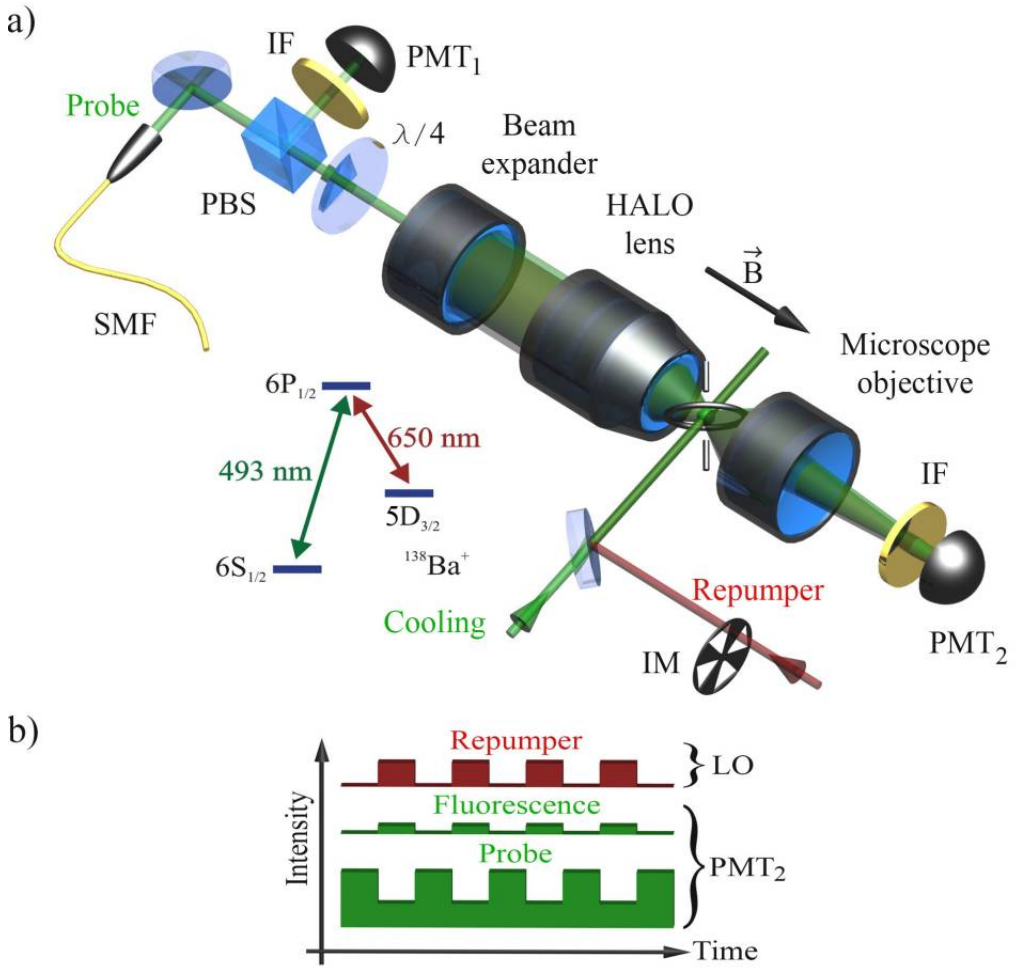

Figure 5.2: a) Schematic of the experimental setup. PBS: polarizing beam splitter, $\lambda/4$: quarter-wave plate, IF: interference filter to select the green fluorescence, IM: intensity modulation, PMT: photomultiplier and SMF: single mode fiber. The ion is cooled by the *cooling* beam, while the *repumper* recycles population from the $5D_{3/2}$ state manifold to the $6S_{1/2}$ to $6P_{1/2}$ transition. The *probe* beam is spatially adjusted to match part of the atomic dipole emission profile and is detected on the photomultiplier PMT_2. b) Extinction detection scheme. Probe beam and fluorescence modulation signals from PMT_2 can be unambiguously distinguished due to their mutual π phase shift. The modulated signal from PMT_2 is mixed down to DC and further analyzed. The figure is taken from the reference [123].

ring-trap setup 2.3.2 for more details about the objective positioning. 1.5 % of the transmitted probe together with a fraction of the ion's green fluorescence is then collected by a macroscope objective and detected on photomultiplier PMT_2. The green fluorescence is

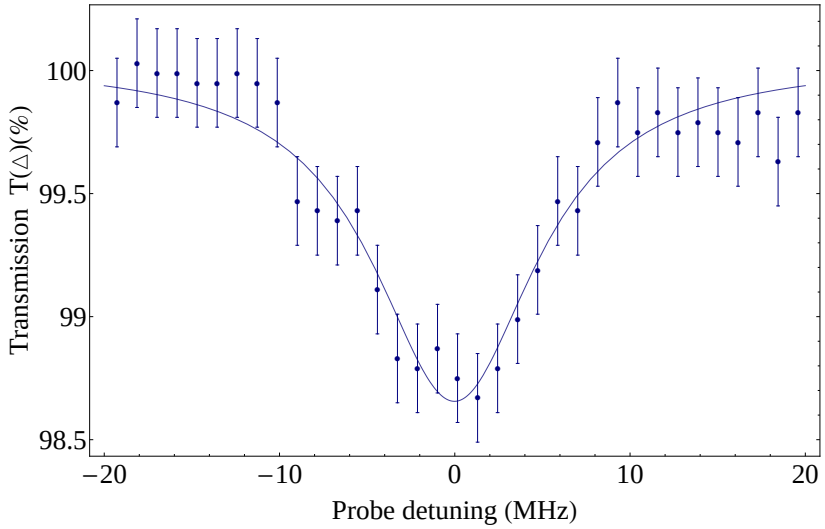

Figure 5.3: Normalized power of a probe field transmitted through a single trapped Barium ion as a function of the probe beam detuning. The transmission spectrum is fitted by a Lorentzian profile with a width of 11 MHz. The peak probe beam extinction is 1.35%.

also detected in the backward direction by the PMT_1. A typical fluorescence count rate measured on PMT_1 is 600 photons per second, with the fluorescence from the probe beam contributing to less than 100 photons per second. After considering detection losses, these count rates are still lower than the count rates typically observed for the $6S_{1/2}$ to $6P_{1/2}$ transition in saturation by factor of more than ten.

We modulate the repumper at 600 Hz using a mechanical chopper (IM) to allow for precise estimation of our extinction efficiency. When the repumper beam is on, fast optical pumping to the S state takes place, which allows both scattering of the probe and cooling. When the repumper is off, however, the green cooling beam depopulates the S state, so that the probe does not interact with the ion. The probe signal intensity is then modulated at 600 Hz by the ion with a phase shifted by π with respect to the chopping signal. The signal from PMT_2 is subsequently demodulated and low pass filtered. As a first step, we find the local oscillator phase which yields the maximum positive signal amplitude for the fluorescence only, i.e. operating with large cooling field powers and with the probe off. Next we turn down the cooling beam power to below saturation in order to observe a negligible fluorescence signal whilst still cooling the ion efficiently. With the probe field on, reflection off the ion gives a negative signal in transmission (see figure 5.2(b)), thus unambiguously discriminating the fluorescence contribution from the probe extinction.

Figure 5.3 shows a typical scan of the probe beam extinction as a function of probe frequency. We observed a Lorentzian dependence of the transmission profile with a width

of 11 MHz. A maximum extinction of 1.35 % was found on resonance. The difference with the extinction predicted in [125] can be partly explained by imperfect overlap of the incoming probe polarization mode with the polarization of the scattered light and by residual saturation of the S to P transition by the cooling beam. Residual spherical aberrations and atomic motion reduce the spatial matching of the probe with the dipole field and thus effectively decrease the solid angle covered by the high-NA lens. Larger extinctions are likely to be reached through better pumping preparation and by time separation of the cooling and extinction measurement processes.

5.3 Electromagnetically induced transparency from a single atom

In the extinction experiment we observed a reduced intensity of a weak probe beam after interaction with a single ion. This enables us to demonstrate quantum-optics phenomena, which were so far available only in optically thick media, using single atoms trapped in free space. In this section, we present an experimental observation of electromagnetically induced transparency with a single ion.

5.3.1 Theoretical model

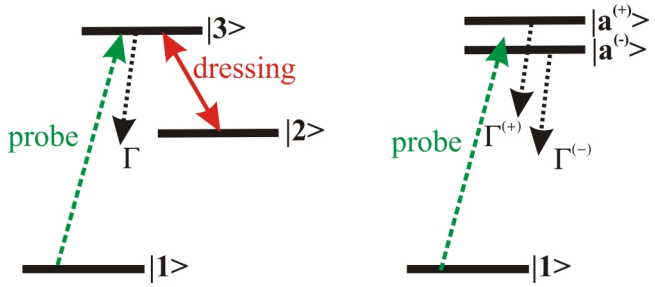

Figure 5.4: Theoretical model of the electromagnetically induced transparency based on the dressed states approach.

Electromagnetically induced transparency (EIT) is an optical phenomenon where in optically dense media, typically large cloud of atoms, the transparency of a weak electromagnetic field (probe field) is influenced by the presence of a strong field (control field) [117]. In the dressed-states picture, the control field creates a pair of dressed states as depicted in figure 5.4 [127, 128]. Their decay channels interfere and create a hole in the absorption profile for the probe field tuned to the center of the splitting. The linear susceptibilities of decay channels from the two dressed states are equally spaced with

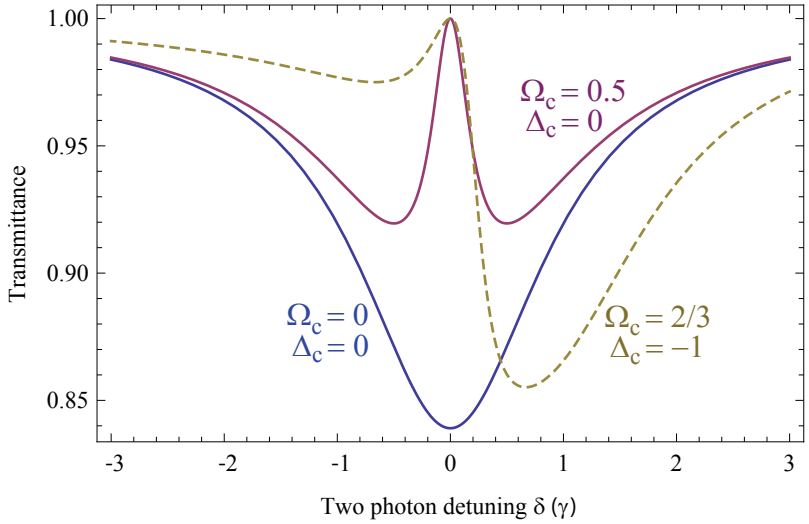

Figure 5.5: Illustration of the transmission profiles for various control and probe lasers driving parameters. Detunings and Rabi-frequencies are given in units of spontaneous decay rate γ. The ground-state dephasing rate here is assumed to be zero for simplicity. At the two-photon detuning $\delta = 0$ a transparency window opens in the extinction spectra for the weak probe beam and any nonzero Rabi-frequency of the control beam Ω_c.

respect to probe field frequency, but due to opposite signs of the detuning the excitation probability amplitudes interfere destructively.

Under weak probe excitation, the probe transmission as a function of the two-photon detuning $\delta = \Delta_p - \Delta_c$ can be found by solving the Bloch equations [127] and using the input-output relations (5.1). Δ_p and Δ_c are probe and control lasers detunings, respectively. We can then replace the function $\mathcal{L}$ in equation (5.3) by

$$\mathcal{L}_\Lambda(\delta) = \frac{\gamma(\gamma_0 - i\delta)}{(\gamma_0 - i\delta)(\gamma + i\Delta_p) + \Omega_c^2}, \tag{5.4}$$

where Ω_c is the Rabi frequency of the control laser field, γ_0 the ground state dephasing rate, γ the natural linewidth of the two transitions (assumed to be the same for simplicity). The relation 5.4 can be can found also by solving the master equation for a three-level atom and evaluating the expression for the linear susceptibility on the probe transition [117]. An important condition for EIT to take place is $\gamma\gamma_0 \ll \Omega_c^2$, i.e. the pumping rate to the dark state must be much faster than any ground state decoherence process γ_0. Independent frequency fluctuations of the two laser fields, magnetic field fluctuations, and atomic motion induced Doppler shifts which contribute to γ_0, must be therefore reduced. Extinction of the resonant probe can then be completely inhibited, within a small range of control laser detuning Ω_c^2/γ, creating an EIT window in the extinction spectrum, see figure 5.5.

5.3.2 Experimental results

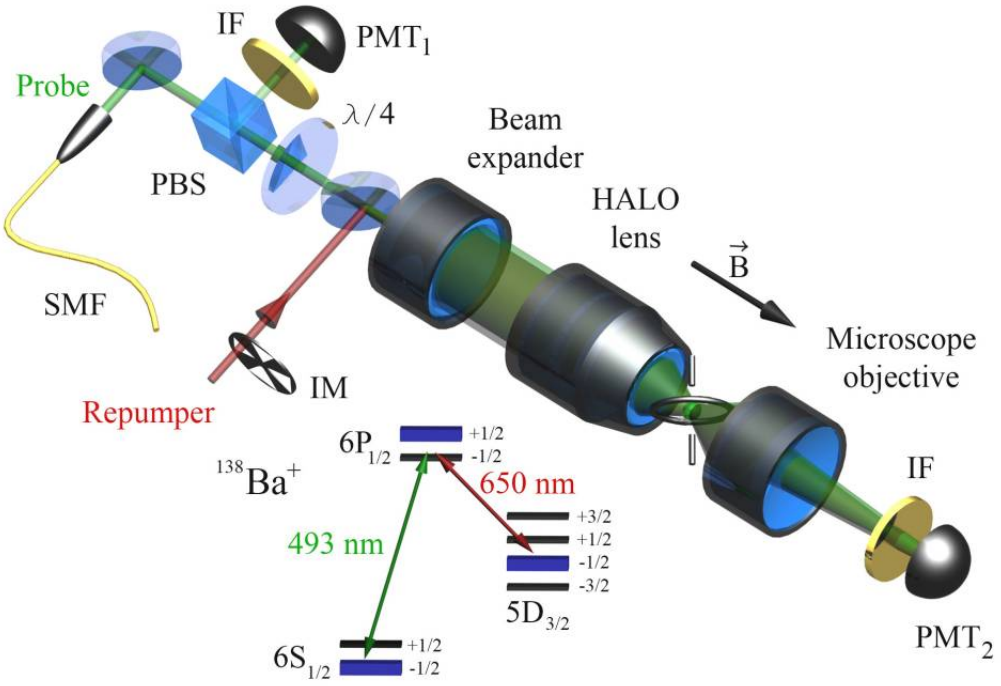

Figure 5.6: Schematic of the experimental setup for observation of electromagnetically induced transparency. The probe field itself serves as a cooling beam and a co-propagating repumper is used. A weak magnetic field $\vec{B}$ lifts the energetic degeneracy of the Zeeman substates and creates an eight-level system. The levels marked as bold lines were employed in the EIT experiment. The figure is taken from the reference [123].

In the EIT experiment [123], we co-propagated the control and probe fields to eliminate the effects of Doppler shifts due to the ion motion, see figure 5.6. We found that the motion induced decoherence yields broadening of tens of kHz, which reduced the EIT when the control and the probe were orthogonal to each other. We did not use the cooling fields which would reduce the EIT process, so the ion was now cooled by the probe itself. Consequently, a red-detuned and more intense probe was used, which reduced the extinction efficiencies to about 0.6%. Due to the multi-level structure of Barium, a single three-level system can only be perfectly isolated from the others through optical pre-pumping. Stark-shifts induced by the other levels and double-Λ type couplings here contribute to a slight reduction of the EIT contrast.

Figure 5.7 a) shows the probe beam extinction strength as the control field is scanned across the two-photon resonance. We observe a large inhibition of the probe beam extinction at zero two-photon detuning, with a peak value of 75 %. The measured linewidth

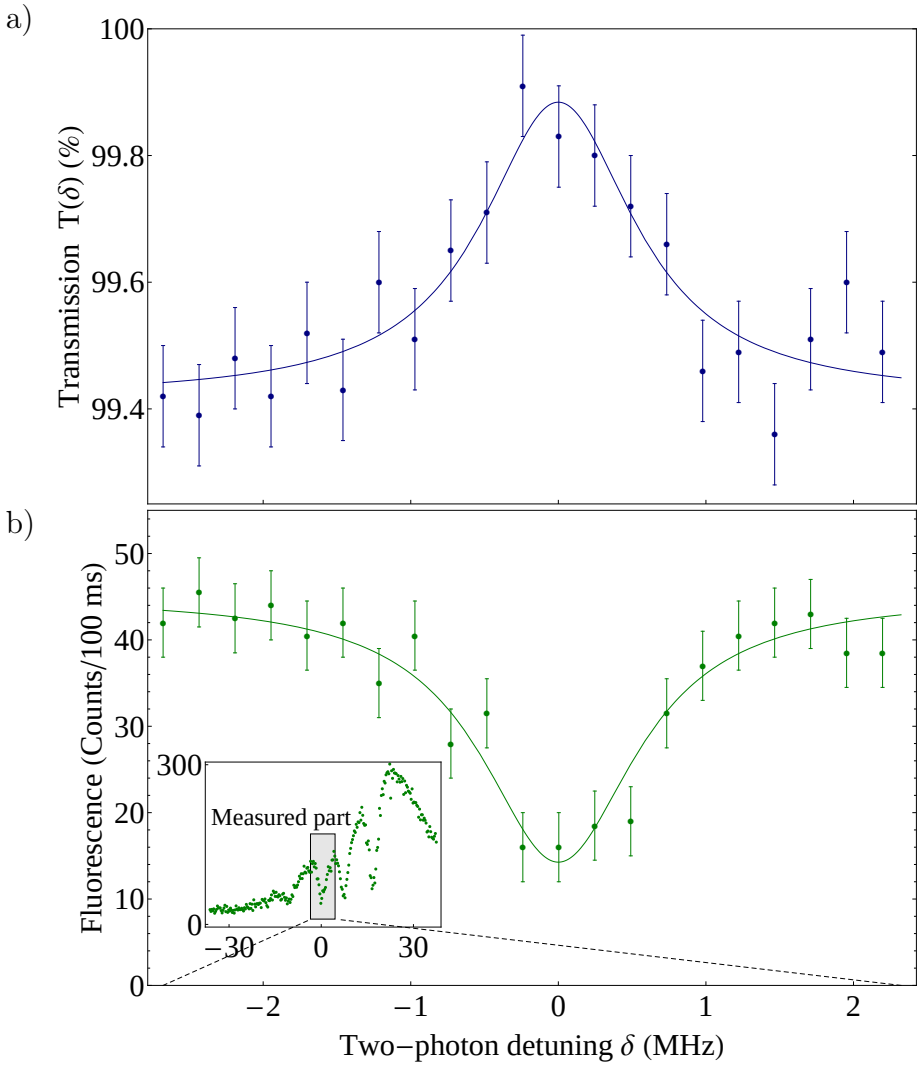

Figure 5.7: Measured extinction with EIT window and fluorescence spectra. a) Normalized transmitted power of a probe field scattered by a single ion as a function of the two-photon detuning. The control beam frequency is tuned across a two-photon resonance, which enhances forward scattering via EIT. The Lorentzian fit of the EIT transmission dip gives a linewidth of 1.2 MHz and suppression of the probe beam extinction of 75 %. b) Dark resonance in the fluorescence spectrum simultaneously measured in the backward direction. The inset shows a typical fluorescence spectrum with all four dark resonances. The EIT experiment was performed for the two-photon detunings corresponding to the shaded part of the spectrum.

of the EIT window is 1.2 MHz, much below the natural linewidth of the S to P transition. Figure 5.7 b) shows the resulting scattered light intensity in the backward direction, showing a corresponding decrease of the fluorescence light around the two-photon resonance, as expected due to dark-state pumping. Although the ion motion was too large to yield significant extinction on the blue side, the other three EIT profiles corresponding to the measured dark-resonances in fluorescence spectrum could also be observed. The contrast and width of these two-photon resonances are mostly given by power broadening and frequency fluctuations of our two lasers. The control and probe laser linewidths are 80 kHz and 20 kHz respectively, which allows a minimal EIT transmission window width of 82 kHz to be observed. Performing an efficient pre-pumping to one of the $6S_{1/2}$ Zeeman sublevels and switching the cooling fields off while the EIT is measured would allow us to reach ultra-narrow transmission profiles. This is of significant interest as this means that large phase shifts are imprinted on the probe field [128], which might become useful for precision spectroscopy and state detection of single atoms.

5.4 Single atom as a mirror of an optical cavity

In the extinction and EIT experiments we were able to observe an attenuation of a weak coherent field by a single atom at the order of one percent. We believe that the observed extinction corresponds solely to the coherent reflection and the interference mechanism described in section 5.2.1, rather than to the incoherent process of absorption of probe light by the atom [129]. Based on this assumption, we designed an experiment where a single Barium ion corresponds to the mirror of a Fabry-Pérot cavity. Results of the transmissivity and reflectivity measurements using such a setup will not only validate our assumption, but they will help us to understand and study atom-light interactions in a novel regime, where the fields of cavity QED and free-space coupling merge together. The experiment and its theoretical description presented here can be found also in the reference [93].

5.4.1 Experimental setup

We consider the single atom to be an optical reflector, as depicted in the set-up of figure 5.8. The central frequency and transmission bandwidth of the single atom-mirror can be estimated from single-atom extinction measurements, which were done in the same parameter regime of laser intensities and detunings. As described in chapter 5.2, we use a very weak probe beam resonant with the $S_{1/2,(m=+1/2)}$-$P_{1/2,(m=-1/2)}$ transition for observation of the extinction of a laser field by the ion in free space. The probe beam is overlapped with part of the dipole emission pattern of the ion using a custom-designed objective with a numerical aperture (NA) of 0.4. A 1.5% fraction of the ion's 493 nm

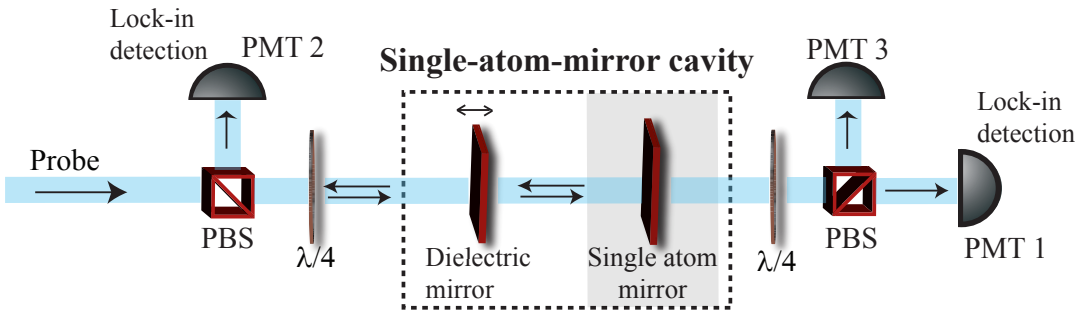

Figure 5.8: Single ion+mirror set-up. The probe field is coupled to the atom-mirror cavity through the dielectric mirror that is mounted on piezo stages. The intensity of the probe is measured in transmission by PMT1 and in reflection by PMT2. PMT3 is used for measuring the ion fluorescence. The figure is taken from the reference [93].

fluorescence together with the transmitted part of the probe beam is then collected by a microscope objective and detected by the photomultipliers PMT3 and PMT1, respectively. Again, we use here an intensity modulation of the 650 nm laser beam and a lock-in detection to enhance the sensitivity of our measurements to the detected extinction signal. In the case of coherent reflection of a laser field by a single atom, the back-scattered field must be able to interfere with the driving laser. To verify this, we modify our extinction experimental setup by inserting a dielectric mirror 30 cm away from the atom into the probe path, with a reflectivity $|r|^2 = 1 - |t|^2 = 99.7\,\%$. We align this mirror so that the ion is re-imaged onto itself and shine the resonant probe through it. Treating this system as a Fabry-Pérot cavity and modelling the atom as a mirror with amplitude reflectivity 2ϵ [124], one can naively assume that the transmissivity of the probe laser intensity reads

$$T = \left| \frac{t(1-2\epsilon)}{1 - 2r\epsilon e^{i\phi_L}} \right|^2, \tag{5.5}$$

where $\phi_L = 2k_L R$, R is the atom-mirror distance and k_L the wavevector of the probe laser. The finesse $\mathcal{F} = \pi\sqrt{2\epsilon r}/(1-2\epsilon r)$ of such a cavity-like set-up can in fact be made very large by using a high numerical aperture lens such that $\epsilon \to 50\,\%$ together with a highly reflective dielectric mirror. In our experiment, the atom reflectivity is around 1% [123], so the transmitted intensity is well approximated by

$$T \approx |t|^2 |1 - 2\epsilon + 2\epsilon r e^{i\phi_L}|^2. \tag{5.6}$$

By tuning the distance between the dielectric mirror and the ion, one would therefore expect a dependence of the transmitted signal on the cavity length, provided that the temporal coherence of the incoming field is preserved upon single-atom reflection.

5.4.2 Ion-mirror cavity measurements results

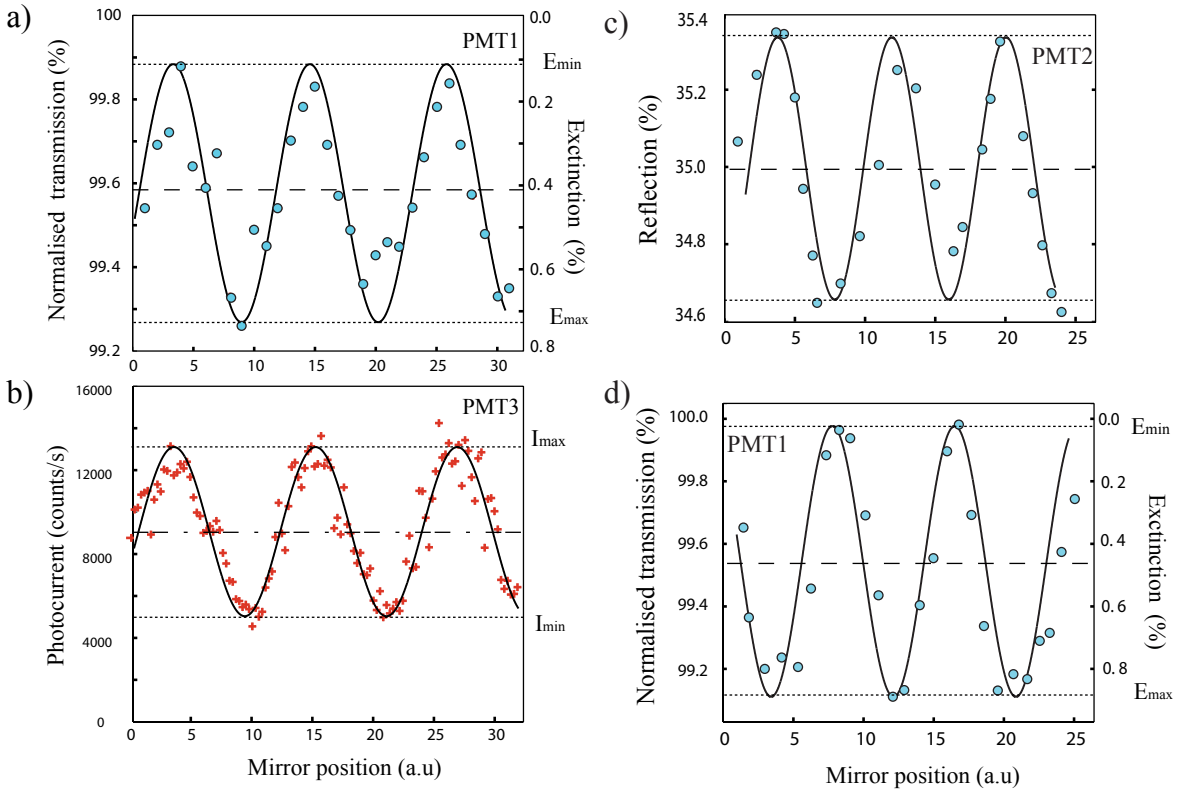

Figure 5.9: a) Normalized transmission $T/|t|^2$ of the probe through the single atom-mirror system as a function of the mirror position, with a 99.7 % reflective dielectric mirror. The dashed lines shows the transmission of the probe when the mirror is slightly misaligned. The dotted lines show the minimum and maximum extinction values used for estimating the contrast V'. b) Interference of fluorescence photons measured on PMT3 with a 99.7 % reflective mirror. Solid lines are the sinusoidal fits to the data. The dotted lines show the minimum and maximum photocurrent values used for estimating the contrast V. c) Intensity of the probe reflected off the cavity, normalized to the probe intensity without ion, and using a 75% reflective dielectric mirror. d) shows the transmission of the probe through the atom-mirror system as a function of the 75 % reflective mirror position, normalized to the mirror transmissivity. The dashed line in c) shows the reflection of the probe without the ion and in d) the transmission with the mirror misaligned from the ion.

The operation of our ion-mirror system is shown in figure 5.9 a). As the mirror position is scanned, we indeed observed clear sinusoidal oscillations of the power detected in PMT1 on a wavelength scale. These results reveal that the elastic back-scattered field is

interfering with the transmitted probe, and that the ion is very well within the Lamb-Dicke regime [66]. Figure 5.9 b) shows the fluorescence rate measured at PMT3 for the same experimental conditions but with the probe field blocked. The intensity change of the fluorescence rate is the result of the self-interference of single photons, which can be expressed as $I = I_0(1 + V\cos(\phi_L))$ [39, 130]. With our ion-mirror distance (30 cm), the interference contrast V is mostly limited by residual aberrations of the imaging optics and atomic motion [39, 66]. As predicted by the formula for the transmission T (equation 5.6), the two signals in figure 5.9 a) and figure 5.9 b) oscillate perfectly in phase. The oscillations are however observed with a lower contrast than for the extinction coefficient (defined as $E = 1 - T/|t|^2$, and plotted on the right axis). As we will show, this pronounced difference stems from an aberration-free dependence of the extinction contrast. We then perform another experiment in which we replace the high reflectivity mirror by a 25%/75% mirror. The results are shown in figure 5.9 c) and d) where we simultaneously recorded the reflected and transmitted powers measured on PMT2 and PMT1, respectively. With this mirror reflectivity, we are able to measure the change of the probe power being reflected off the cavity, which we found to be exactly out of phase with the transmitted signal, as is predicted for a Fabry-Pérot cavity response. We note that, here again, an unexpectedly large extinction contrast is observed.

5.4.3 The role of optical aberrations

The modulation of the fluorescence rate in figure 5.9 b), is due to a self-interference of single photons emitted by the atom [39, 130]. The intensity change of the fluorescence can be expressed as

$$I = I_0(1 + V\cos(\phi_L)). \tag{5.7}$$

With our ion-mirror distance (30 cm), the interference contrast

$$V = (I_{\max} - I_{\min})/(I_{\max} + I_{\min}) \tag{5.8}$$

is mostly limited by residual aberrations of the imaging optics and atomic motion [39]. As predicted by the formulas for the transmission T (5.6) and fluorescence intensity I (5.7), the two signals in figure 5.9-a) and figure 5.9-b) oscillate in phase. We note however, that the contrasts $V' = (E_{\max} - E_{\min})/(E_{\max} + E_{\min})$ of the ion-mirror cavity extinction in figure 5.9-a) and defined on the right axis, and the ion's fluorescence self-interference contrast in figure 5.9-b), clearly differ.

To understand this effect, we will consider the influence of aberrations by including a random phase shift to each of the contributing amplitudes of the transmitted field. We change the input field amplitude $E_{\text{in}} \to E_{\text{in}}e^{i\phi'(\vec{r}_l)}$ so that the input probe gets an $\vec{r}_l$-dependent phase shift when it goes through the point $\vec{r}_l$ on the lens surface. We replace

ϵ by ϵ' ($\epsilon > \epsilon'$) to account for a decrease of the field amplitude at the focus due to these same phase shifts. Finally, we make the substitution $2\epsilon e^{i\phi_L} E_{\text{in}} \rightarrow 2\epsilon' e^{i\phi_L} e^{2i\phi'(\vec{r}_l)} E_{\text{in}}$, where the reflected scattered field gets two times the $\vec{r}_l$-dependent phase shift. For simplicity, we here consider the case of a high mirror reflectivity. We then obtain $T(\vec{r}_l) \approx |t|^2(1 - 4\epsilon' \cos\phi(\vec{r}_l) - 4\epsilon' \cos(\phi(\vec{r}_l) + \phi_L))$, which, averaged over the lens surface with a corrugation pitch smaller than the optical wavelength λ, gives the total transmission

$$T \approx |t|^2(1 - 4\bar{\epsilon}(1 - \cos(\phi_L))). \tag{5.9}$$

Here $\bar{\epsilon} = \epsilon' J_0(\eta)$, $J_0(\eta)$ is the first order Bessel function of the first kind and $\eta = 2\pi\sigma_{\text{ab}}/\lambda$ where σ_{ab} is the root mean square amplitude of the aberrations. We then obtain the normalized extinction plotted in figure 5.9-a) to be

$$E = 4\bar{\epsilon}(1 - \cos(\phi_L)). \tag{5.10}$$

When making the same substitutions in the case of the single photon interference that we observed in figure 5.9 b), one gets the intensity

$$I = I_0(1 + J_0(\eta)\cos(\phi_L)), \tag{5.11}$$

The contrast of I and E will therefore differ, since the contrast of the single photon interference fringes depends directly on the aberrations. The two intensities that contribute to the extinction E arise from an interference between the input and the scattered amplitudes that carry the same global phase shifts, which is the reason for the larger contrast observed in figure 5.9-a) and figure 5.9-d) over figure 5.9-b). This observation can be important for precise characterization and control of the tight focussing of optical fields onto single trapped particles.

To find out how much of the single photon-interference contrast is limited by aberrations, we used an independent estimation method by coupling the fluorescence into a single mode fiber. A contrast close to 90% was observed for a single ion trapped and Doppler cooled in the ring trap, which shows that the self-interference contrast is here in fact mostly limited by aberrations. $J_0(\eta)$ is therefore about 30%-40% in our measurements. We note that atomic motion would also give aberration-like effects, however a separation of these two sources of error is not straightforward and will be the subject of further studies.

5.4.4 Quantum electrodynamics calculations

We will now investigate whether the naive Fabry-Pérot interpretation that we used to describe our results is valid. One could indeed wonder how the modification of the quantum vacuum around the atom affects our results. It is clear that the dielectric mirror

imposes new boundary conditions that will change the vacuum mode density close to the atom, but it is less obvious how much it will contribute to the probe intensity changes that we observe in this experiment. One can in fact show, that solving the multimode Heisenberg equations in a time-dependent perturbation theory gives [93]

$$T = |t|^2 \left| 1 - \frac{2 g_\epsilon \overline{g}^*}{\tilde{\gamma} + i\tilde{\Delta}} \right|^2, \tag{5.12}$$

assuming the input probe to be resonant with the atomic transition. The full calculation can be found in supplemental material of reference [93]. Here, g_ϵ denote the atomic coupling strength in the probe mode, $\overline{g}$ is the mean coupling to all the modes, $\tilde{\gamma}$ and $\tilde{\Delta}$ are the decay and level shifts modified by the presence of the mirror. Their expressions can be evaluated using the appropriate spatial mode function for this system [131] and we can then show that

$$\frac{g_\epsilon \overline{g}^*}{\tilde{\gamma} + i\tilde{\Delta}} = \frac{\epsilon(1 - r e^{i\phi_L})}{1 - 2r\epsilon e^{i\phi_L}}. \tag{5.13}$$

After combining this relation with equation (5.12) we obtain the same transmissivity as was obtained by modelling the atom as a mirror with reflectivity 2ϵ (equation 5.5). Interestingly, the QED calculations yield the same mathematical results as the direct Fabry-Pérot calculation.

In this QED approach, it was not necessary to invoke multiple reflections off the atom for the Fabry-Pérot-like transmission to appear. The transmission of the probe through the single atom+mirror system is mathematically equivalent to a cavity, but the origin of the peaked transmission profile can be interpreted as a line-narrowing effect due to the QED-induced changes of the spontaneous emission rate and level shift. In our experiment, we observed a change of the coupling between the atom and the probe mode, due to the modification of the mode density induced by the mirror. Deviations from the sinusoidal shape due to line narrowing would be visible for a lens covering a solid angle of more than 10%. We note that, with this interpretation, the aberration-free dependence of the extinction contrast is analogous to an almost complete cancellation and enhancement by a factor of two of the atomic coupling constant in the probe mode.

5.5 Conclusion

In the presented extinction experiments, we observed both the direct extinction of a weak probe field and electromagnetically induced transparency from a single Barium ion. The maximum observed extinction of the probe beam intensity due to the scattering on the ion was 1.3% and inhibition of extinction due to EIT was almost 75%. The amount of extinction is limited mainly by the numerical aperture of the employed lens, and residual

saturation of the probed transition by the cooling beams. Using a numerical aperture of, say 0.7, and a better pumping scenario, would already give extinction values of up to 50%, which are within experimental reach. Better EIT contrasts and narrower features can be reached through efficient preparation of an isolated Λ scheme, with pre-pumping steps. Our results have a number of direct applications. For example, one can take advantage of the sensitivity of EIT with regards to Doppler shifts to read out the atomic motional state in a quantum non-demolition manner, thereby also opening the way towards quantum feedback [104]. Furthermore, the presented results have direct implications for long distance quantum information [20] and quantum computation. Quantum memories, where quantum states between atoms and light fields are reversibly exchanged, indeed form an essential part of quantum repeater architectures [21, 117] and EIT is a prominent method to achieve such a transfer [117].

We successfully observed the operation of a single atom as an optical mirror of a Fabry-Pérot-like cavity. Our investigations are performed in a novel regime where a significant fraction of the power of a probe field can be affected by the atom in free space. This allows us to realize an experiment in which both the properties of an atom as a reflector and the modification of the atomic coupling constant can play a role. Although a simple cavity interpretation lends itself naturally to a description of our experiment, a more general QED formulation should be preferred for an unambiguous discrimination of the involved mechanisms. Interestingly, for our experimental parameters (weak excitation, small atom-mirror distances), we found that both interpretations are equivalent. Our set-up demonstrates almost full suppression and enhancement by a factor of two of the atomic coupling constant in the probe mode. Besides the appealing quantum memory application that we presented above, our set-up has a number of other realistic prospects. It can be, for instance, a useful tool for operating the ion as an optical switch, similar to the single atom transistors using EIT implemented in [122, 123, 132, 133] or using a population inversion [113].

We foresee a direct application of our atom-mirror cavity system. In discrete variable quantum communications, and specifically for quantum repeater architectures, single photons must be stored and released from stationary qubits [22, 134] to prevent the unavoidable losses in optical fibers [20]. The required efficient coupling between a single photon and a single atom can be obtained through the use of a high-finesse cavity [22, 135], or parabolic mirrors to mode-match the incoming field with the whole atomic dipole field [136]. Our single atom-mirror set-up is an attractive alternative solution for full absorption of a single photon. In such a scenario, the retro-reflection of the back-scattered field by the mirror mediates the required interference effect so that the excitation probability of the atom can reach more than 50% [137, 138]. However, unlike standard lossless mirrors, the ion will fully reflect the light back into the probe mode only for $\epsilon = 50\,\%$. So in the realistic NA case, the scattered field is emitted into almost 4π steradian. With

standard mirrors, impedance matching can be reached by matching the mirror reflectivities. Since impedance matching is here not immediately fulfilled, in order to attain a steady state transmission of the optical field through such a system, one can optically pump a fraction of atomic population to another state to match the input mirror reflectivity. Implementing a dynamic coherent transfer of population [111, 134] to another metastable ground state will furthermore allow efficient and long lived quantum storage of a single photon pulse in the atom. Alternatively, one could ramp the mirror position from the anti-node to the node of the standing wave so as to match the incoming photon's temporal profile to the ion-mirror system and store the photon in the long lived atomic excited state [131]. Although the present results are obtained in the elastic scattering regime with two levels, our experimental results may be seen as the first tests of such a new single atom-photon interface.

6 Entanglement of two ions via single photon detection

6.1 Introduction

Entanglement lies at heart of quantum information science [139]. It is an essential resource for quantum communication protocols including the secure distribution of cryptographic keys [140] and quantum teleportation [141], as well as for quantum computation schemes promising an exponential speed-up for particular computational tasks [142].

Long-lived entanglement between distant physical systems is an essential primitive for quantum communication networks [20,21], distributed quantum computation [17–19] and further tests of quantum mechanics. There are several protocols generating entanglement between distant material systems. The vast majority of them exploit travelling light fields as mediators of the entanglement generation process. One way to generate distant entanglement is based on the generation of entanglement between a matter-qubit and a single photon followed by the mapping of the photonic state onto a second matter-qubit [22]. Another useful approach is to use the single photons for providing a heralded entanglement generation [20, 21, 37, 38].

The realization of heralded entanglement between distant atomic ensembles [143, 144] was amongst the first major experimental achievements in this field. Probabilistic generation of heralded entanglement between single atoms [38] was demonstrated using single trapped ions [145] with an entanglement generation rate given by the probability of coincident detection of two photons coming from the ions [146, 147]. More recently, single neutral atoms trapped at distant locations were entangled by first generating the single atom-photon entanglement and then mapping the photonic state onto the electronic state of the second atom [148]. A heralding mechanism will however be essential for efficient entanglement and scalability of quantum networks using realistic channels [21], and single qubit operations are required for distributed quantum information processing schemes [87]. For future quantum information applications it therefore seems to be crucial to realize *heralded* distant entanglement with the possibility of *single qubit operations* and with *high entanglement generation rate* at the same time.

We present the experimental realization of a fundamental process which fulfills all three conditions by showing entanglement between two well-defined atomic qubits via emission and detection of a single light quanta, as proposed in the seminal work of Cabrillo et al. [37]. In this scheme, both the energy and the phase of the emitted single photon are used for entanglement generation. In addition, this mechanism allows the demonstration of a large speedup in entanglement generation rate compared to the previously realized heralded entanglement protocol with single atoms [145, 146]. This result has potential to enable the practical distribution of quantum information over long distances using single atom architectures.

A part of the results and of the text presented in this chapter can be found also in the reference [149].

6.2 Generation of entanglement by single photon detection

Entanglement of distant single atoms through the detection of a single photon, as proposed in the seminal work of Cabrillo et al. [37], is both a fundamental and promising technique for the field of quantum information. In this scheme, two atoms (A,B) are both prepared in the same long-lived electronic state $|gg\rangle$, see figure 6.3. Each atom is then excited with a small probability p_e to another metastable state $|e\rangle$ through a spontaneous Raman process ($|g\rangle \rightarrow |i\rangle \rightarrow |e\rangle$) by weak excitation of the $|g\rangle \rightarrow |i\rangle$ transition and spontaneous emission of the single photon on the $|i\rangle \rightarrow |e\rangle$. Here $|i\rangle$ denotes an auxiliary atomic state with short lifetime. This Raman process entangles each of the atom's internal states $|s\rangle$ with the emitted photon number $|n\rangle$, so the state of each atom and its corresponding light mode can be written as

$$|s,n\rangle = \sqrt{1-p_e}|g,0\rangle e^{i\phi_L} + \sqrt{p_e}|e,1\rangle e^{i\phi_D}. \tag{6.1}$$

Here, the phases ϕ_L and ϕ_D correspond to the phase of the exciting laser at the position of the atoms and the phase acquired by the spontaneously emitted photons on their way to the detectors, respectively. The total state of the system consisting of both atoms and the light modes can be written as

$$\begin{aligned} |s_\mathrm{A}, s_\mathrm{B}, n_\mathrm{A}, n_\mathrm{B}\rangle = {} & (1-p_e)e^{i(\phi_{\mathrm{L,A}}+\phi_{\mathrm{L,B}})}|gg,00\rangle + \\ & + \sqrt{p_e(1-p_e)}(e^{i(\phi_{\mathrm{L,A}}+\phi_{\mathrm{D,B}})}|eg,10\rangle + e^{i(\phi_{\mathrm{L,B}}+\phi_{\mathrm{D,A}})}|ge,01\rangle) + \\ & + p_e e^{i(\phi_{\mathrm{D,A}}+\phi_{\mathrm{D,B}})}|ee,11\rangle. \end{aligned} \tag{6.2}$$

Indistinguishability of the photons from the two atoms is achieved by overlapping their

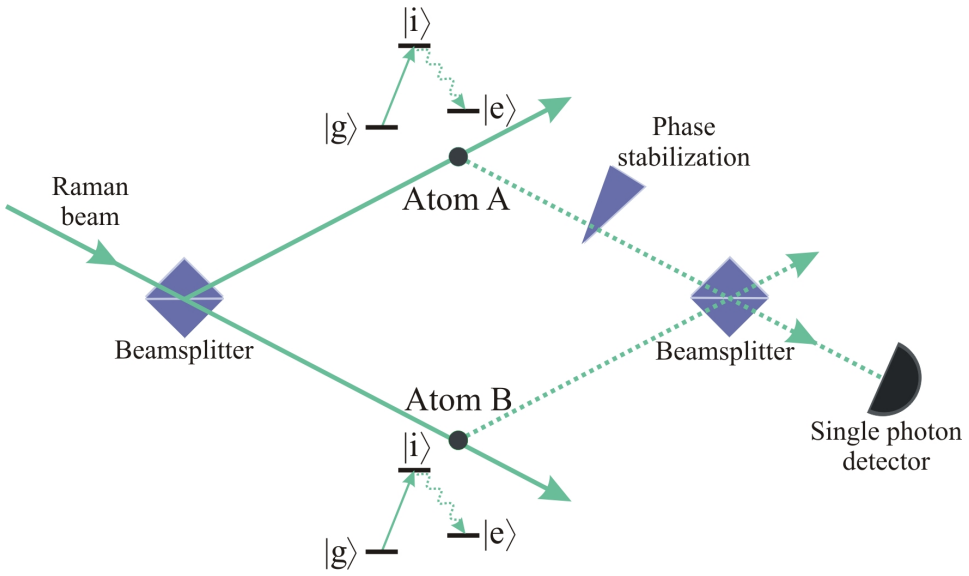

Figure 6.1: Schematic picture of the entanglement generation by single photon detection.

corresponding modes, for example using a beam splitter. Single photon detection then projects the two-atom state onto the entangled state

$$|s_{\mathrm{A}}, s_{\mathrm{B}}\rangle = |\Psi^{\phi}\rangle = \frac{1}{\sqrt{2}}(|eg\rangle + e^{i\phi}|ge\rangle), \tag{6.3}$$

with the probability of 1-p_e. The analysis of success rate and fidelity of the generated states including finite detection efficiency of a realistic experimental setup can be found in the next section (6.2.1). The phase of the generated entangled state ϕ corresponds to the sum of the phase difference acquired by the exciting beam at the position of the two atoms and the phase difference acquired by the photons from the respective atoms upon travelling to the detector,

$$\phi = (\phi_{\mathrm{L,B}} - \phi_{\mathrm{L,A}}) + (\phi_{\mathrm{D,A}} - \phi_{\mathrm{D,B}})). \tag{6.4}$$

The first term in equation (6.4) corresponds to the phase difference of the exciting laser at the position of atoms A and B. The second term is the phase difference acquired by spontaneously emitted photons from the two atoms upon travelling to the detector.

In the ideal case, the fidelity of the generated state with the maximally entangled state (6.3) is limited only by the probability of simultaneous excitation of the two atoms p_e^2, which can be made arbitrarily small at the expense of entanglement generation success probability P_{s}, see figure 6.2. The phase of the generated state depends on the relative length of the excitation and detection paths, which therefore need to be stabilized with sub-wavelength precision. Random changes of these path-lengths caused by

atomic motion or air density fluctuations change the phase of the entangled state (6.3) in an incoherent way, which can considerably reduce the fidelity of the generated state.

6.2.1 Single versus two-photon protocols

Here we compare the efficiency of the two known heralded entanglement generation protocols based on the single-photon [37] and two-photon [38] detection.

The main limitation for generation of heralded distant entanglement between single atoms with high rate is imposed by the relatively small overall detection efficiencies of fluorescence photons emitted by atoms in free space η [146]. For state-of-the-art experimental setups employing high numerical aperture optics close to single trapped neutral atoms or ions, η_D is on the order of 10^{-3} [89,125,150–152]. There is a large effort in experimental quantum optics community towards increasing this number both by employing very high numerical aperture optics in the form of spherical [48] or parabolic [137, 153] mirrors and by developing single-photon detectors with high quantum efficiency. However, even with these improvements it will be hard to increase the overall detection efficiency by more than one order of magnitude.

Two-photon protocol

In the two-photon protocol, two distant atoms are first simultaneously excited using a short laser pulse. After excitation to the same electronic state, the atoms ideally decay with a probability of 50 % to two different electronic levels and the detection of two photons with typically different polarization states in an indistinguishable way triggers entanglement between the atoms. This corresponds to first entangling each of the atomic states with the polarization of the emitted photon followed by entanglement swapping onto the atoms by detection in a Bell measurement setup. In the case of an overall photon detection efficiency equal to one, this technique generates entangled state of the atoms in half of the trials. However, in realistic experimental setups, the rate of entanglement generation is strongly suppressed due to a finite detection probability, because the two heralding photons need to be detected in the same experimental run.

Comparison of the two protocols

We define two dimensionless measures crucial for the performance of any practical quantum information network. Fidelity between the generated state described by the density matrix ρ and the desired maximally entangled two qubit state $|\psi\rangle$,

$$F = \langle\psi|\rho|\psi\rangle \tag{6.5}$$

and success probability P_s, corresponding to probability with which this state can be generated for given overall detection efficiency η_D.

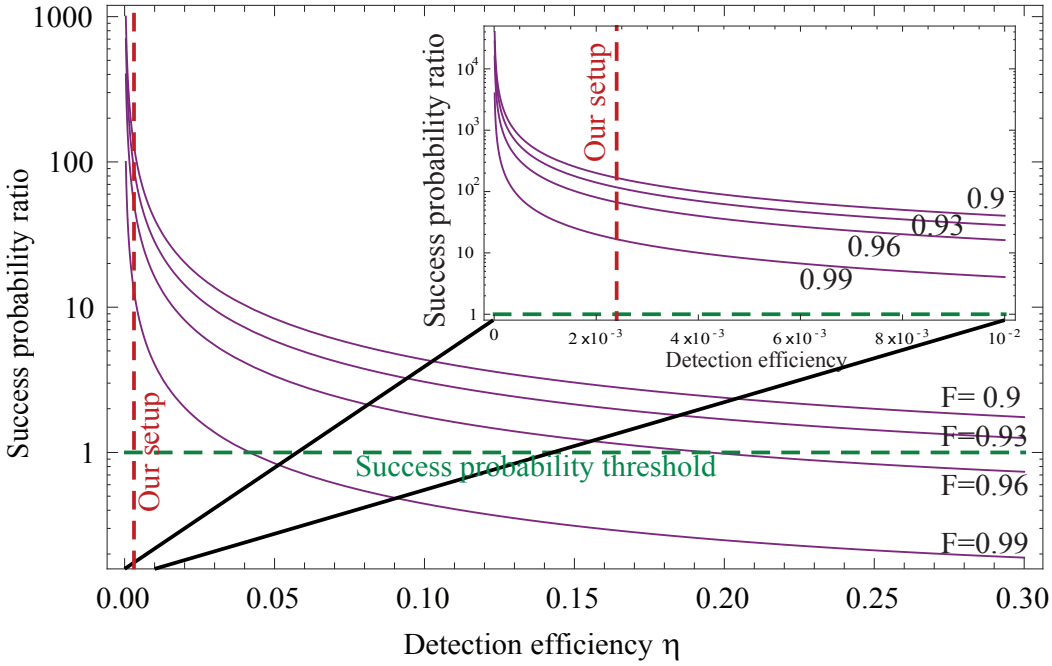

Figure 6.2: Success probability ratio of entanglement generation for the single-photon and two-photon protocols. For current experimental setups, the single-photon scheme is several orders of magnitude faster than the two-photon scheme.

Following the simplified model in the work of Zippilli et al. [146], the fidelity and success rate of the single-photon protocol are given by

$$F_1 \sim (1 - p_e)/(1 - \eta_D p_e) \quad \text{and} \quad P_{s,1} \sim 2\eta_D p_e (1 - \eta_D p_e). \tag{6.6}$$

Here p_e is the probability of the successful excitation and emission of a single photon by a single ion. For a given value of p_e, the fidelity increases with overall detection efficiency because the likelihood of detecting events where two photons are scattered increases. For a two-photon protocol, the effect of the detection efficiency on the generated state fidelity is negligible, because both atoms need to be excited and only coincidence detection events trigger entanglement, and thus the fidelity of the generated state with the maximally entangled state is assumed to be $F_2 = 1$. However, the rate and success probability of entanglement generation depend here quadratically on η_D,

$$P_{s,2} \sim \eta_D^2, \tag{6.7}$$

since the two photons need to be detected at the same time.

Figure 6.2 shows the ratio of success probabilities $R = P_{s,1}/P_{s,2}$ of the two protocols for fixed values of the generated states fidelities as a function of detection efficiency. For

a given desired fidelity the two-photon scheme is faster only for high overall detection efficiencies. There is a large advantage in using the single-photon scheme for experimental setups with detection efficiencies below 10^{-2}. For most of currently realized single-atom experiments, the theoretical gain in entanglement generation rate using the single-photon scheme corresponds to several orders of magnitude. In addition, even for unrealistically high detection efficiencies of more than 90 %, the single-photon scheme can give higher success rates of generated entangled states with high fidelities. This is due to the high detection probability of double excitations which correspond to the fundamental source of infidelity in the single-photon protocol, see equation (6.6).

6.3 Experimental implementation

6.3.1 Experimental setup

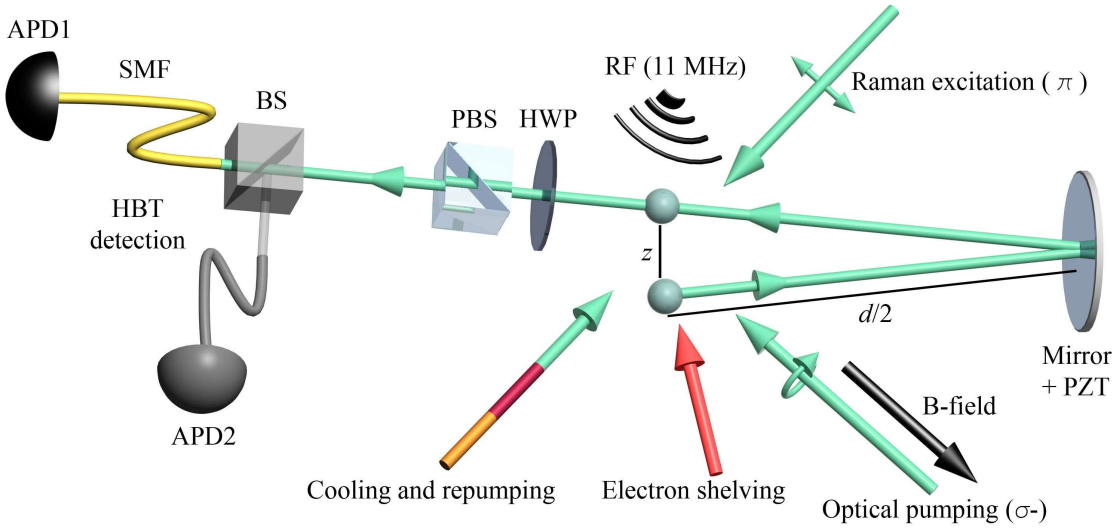

Figure 6.3: Experimental setup for entanglement generation by a single photon detection. a) The fluorescence of the two ions is overlapped using a distant mirror which sets the effective distance between them to $d = 1$ meter. A half wave plate (HWP), a polarizing beam splitter (PBS) and a single-mode optical fiber select the polarization and the spatial mode before an avalanche photodiode (APD1). A non-polarizing beam-splitter and an additional avalanche photodiode (APD2) can be inserted to form a Hanbury-Brown-Twiss setup. The figure is taken from the reference [149].

Two Barium ions are trapped and cooled in our linear Paul trap setup. As shown in

figure 6.3 a) and b), laser light at 493 nm is used to Doppler-cool the ions and to detect their electronic states by means of electron shelving, and a laser field at 650 nm pumps the atoms back to the $6P_{1/2}$ level from the metastable $5D_{3/2}$ state. By carefully adjusting the cooling and trapping parameters, the ions are always well within the Lamb-Dicke limit so that the photon recoil during the Raman scattering process is mostly carried by the trap. This ensures that only minimal information is retained in the motion of the ion about which atom has scattered the photon during the entanglement generation process. The fluorescence photons are efficiently collected by two high numerical aperture lenses (NA ≈ 0.4) placed 14 mm away from the atoms. A magnetic field of 0.41 mT is applied at an angle of 40 degrees with respect to the two-ion axis and defines the quantization axis. After passing through a polarizing beam splitter that blocks the π-polarized light and lets σ-polarized light pass, the spatial overlap of the photons is guaranteed by collecting the atomic fluorescence of the first ion in a single mode optical fiber, whilst the fluorescence of the second ion is sent to a distant mirror that retro-reflects it in the same optical fiber. We note that in our setup, super/sub-radiance effects that might occur here are on the order of 1%, and can thus be neglected [154]. The fluorescence of the two ions (including the Raman scattered light) is then detected by an avalanche photodiode with a quantum efficiency of 60%.

6.3.2 Control of the entangled state phase

In order to produce a pure entangled state of two qubits, the phase ϕ defined in equation (6.4) of the generated states must be controlled with high precision. In our experiment, this is achieved by a measurement of the phase of the interference produced by the elastic scattering of the 493 nm Doppler-cooling beam with wavevector oriented perpendicularly to the magnetic field direction and opposite to the wavevector of the counter-propagating Raman beam, see figure 6.4. The Doppler cooling (phase-stabilization) beam is linearly polarized with polarization vector orthogonal to the magnetic field direction. It therefore excites the σ^+ and σ^- transitions of the $6S_{1/2} \leftrightarrow 6P_{1/2}$ manifold and elastically scattered photons can pass the polarization filter in the detection channel, which blocks the π-polarized light. Photons scattered by the Doppler cooling beam are following the same optical paths as the photons scattered by the Raman beam just in opposite directions. Observation of their interference can be used for stabilization of the relative phase of the exciting Raman beam at the position of the two ions $\phi_{\mathrm{L,B}} - \phi_{\mathrm{L,A}} = \varphi_1 - (\varphi_1 + kz\cos\theta)$ and the phase difference of emitted photons acquired upon travelling to detectors $\phi_{\mathrm{D,A}} - \phi_{\mathrm{D,B}} = kd$. Here z is the mutual distance between the ions, θ is the angle between the ions crystal axis and direction of the exciting Raman beam and φ_1 is the phase of the exciting Raman laser at the position of ion A. Using this method, the phase ϕ can be stabilized and set to the desired value.

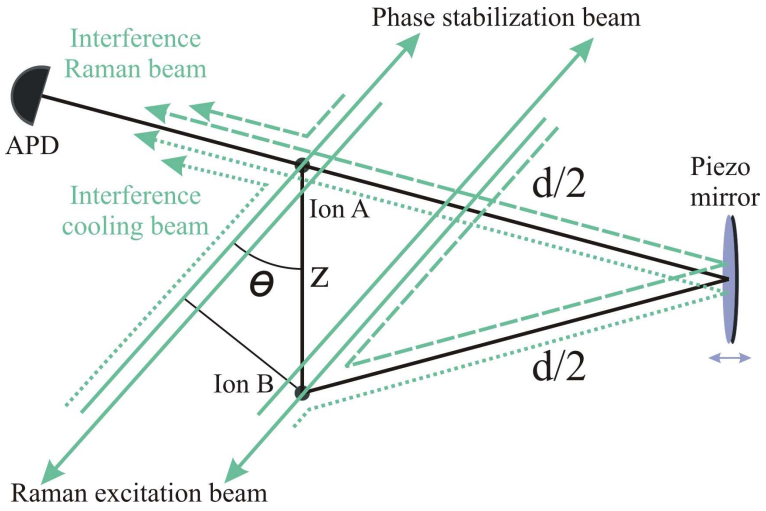

Figure 6.4: Experimental setup for phase stabilization. The exciting Raman and Doppler cooling beams are counter-propagating and the angle θ between them and the two-ion axis is about 40°. The solid green lines depict the direction of the two beams and dashed lines show the corresponding interference paths. Observation of the interference between photons elastically scattered from the two ions by the Doppler cooling beam then enables us to precisely estimate the phase factor ϕ of the generated entangled state (6.3). The phase ϕ can be adjusted by changing the position of the distant piezo mirror. Furthermore, the distance z between the two ions can be set to a value which guarantees that the interference signals generated by the two counter-propagating beams oscillate in-phase.

We set the distance z to a value, which makes the interference signals generated by the two counter-propagating beams *oscillate in-phase* as a function of the distance d. The desired distance z is found by comparing the phase of the two interference fringes for the exciting Raman and phase-stabilization beams. A simple plane-wave model gives the detected light intensity I of the generated interference signals,

$$I_{\text{Raman}} = |e^{-i\varphi_1} + e^{-i(\varphi_1 + kz\cos\theta + kd)}|^2 = 2(1 + \cos(kz\cos\theta + kd)), \tag{6.8a}$$

$$I_{\text{Doppler}} = |e^{-i(\varphi_2 + kz\cos\theta)} + e^{-i(\varphi_2 + kd)}|^2 = 2(1 + \cos(kz\cos\theta - kd)), \tag{6.8b}$$

where φ_2 is the phase of the phase-stabilization beam at the position of ion B. By comparing the phase factors of these interference signals, it is easy to show that they are *in-phase* as a function of the distance d, if the distance $z = n\lambda/(2\cos\theta), n \in \mathbf{Z}$. The phase of the interference pattern generated by the Doppler beam is then simply equal to the overall phase factor ϕ relevant for the generated entangled state. We note that our

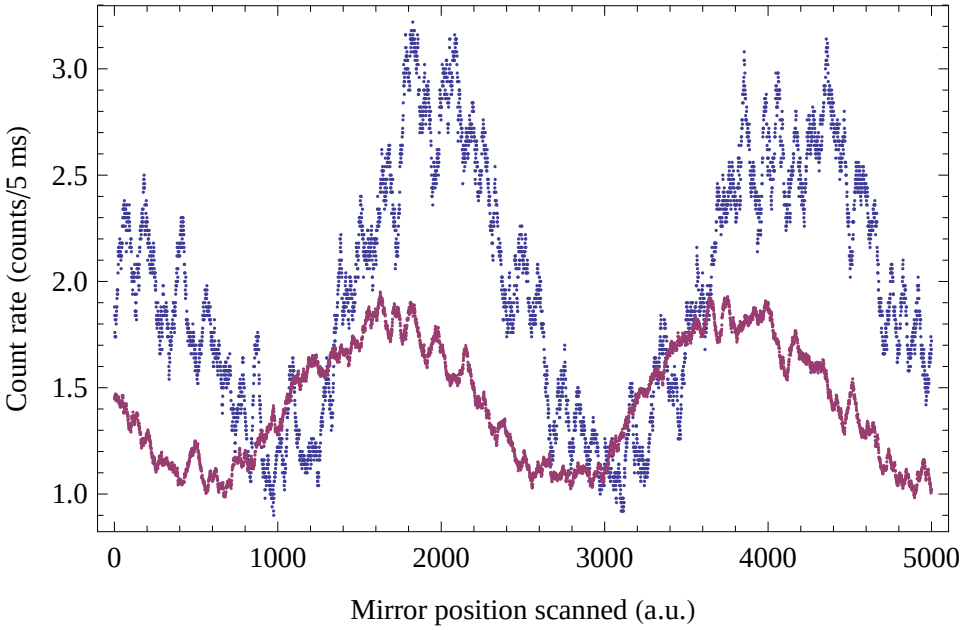

Figure 6.5: Measurement of the phase difference of the interference signals generated by the two counter-propagating beams. Blue and violet traces are the detected count rates of fluorescence scattered by the Raman and phase-stabilization (Doppler cooling) beams, respectively. The fringes are recorded in a pulsed regime where the two driving beams are switched on consecutively in 5 ms intervals, during which the scattered light intensity is detected. The phase of interference fringes is varied by scanning the atom-mirror distance. The estimated phase difference in the presented measurement example is about 47 °.

phase-stabilization technique applies also to setups where the two atoms to be entangled are in distant separate traps.

In the experiment we find the desired distance z by measurement of the interference patterns generated by the Doppler and Raman beams for several tip-voltages, see figure 6.5. The estimated optimal tip-voltage for reaching the in-phase interference signals from these measurements is 243 V. In the experimental realization of the entanglement generation we aim to demonstrate a successful preparation of the state (6.3) for the phase $e^{\phi} = 1$

$$|\Psi^{+}\rangle = \frac{1}{\sqrt{2}}(|eg\rangle + |ge\rangle), \tag{6.9}$$

which then corresponds to an antinode of the measured interference fringe generated by the Doppler beam.

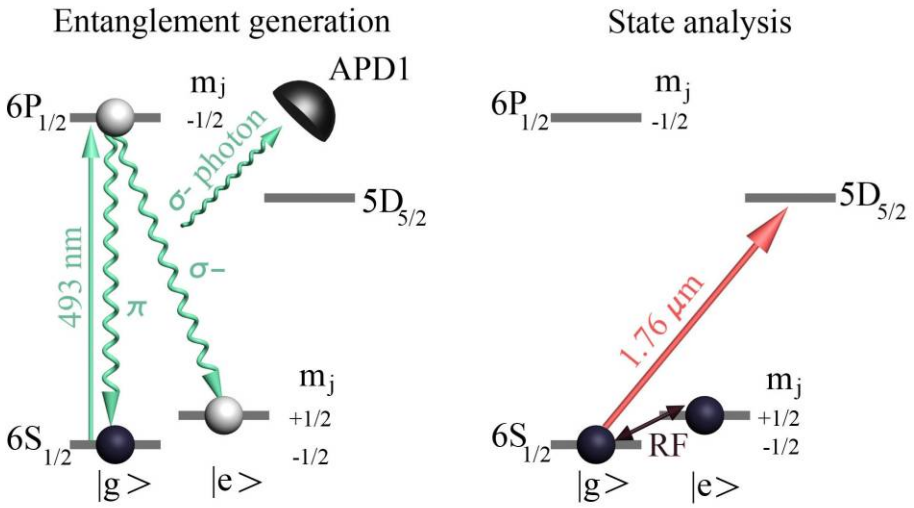

Figure 6.6: Experimental sequence. Spontaneous Raman scattering from $|g\rangle$ to $|e\rangle$ triggers emission of a single photon from the two atoms. Upon successful detection of a σ^- photon, state analysis comprising coherent radio-frequency (RF) pulses at 11 MHz, and electron shelving to the $5D_{5/2}$ level are performed.

6.3.3 Experimental sequence

In the entanglement generation procedure, we first Doppler-cool the ions and stabilize the ion-mirror distance $d/2$ by locking the position of the interference fringe measured during the Doppler cooling sequence to a chosen position, see figure 6.6. The electronic states of the ions are then prepared to the Zeeman substate $|6S_{1/2,(m=-1/2)}\rangle = |g\rangle$ by optical pumping with a circularly polarized 493 nm laser pulse propagating along the magnetic field. Next, a weak horizontally polarized laser pulse (Raman excitation) excites both ions on the $S_{1/2} \leftrightarrow P_{1/2}$ transition with a probability $p_e = 0.07$ through a resonant spontaneous Raman scattering to the other Zeeman sublevel $|6S_{1/2,(m=+1/2)}\rangle = |e\rangle$. The electronic state of each ion is at this point entangled with the number of photons $|0\rangle$ or $|1\rangle$ in the σ^- polarized photonic mode. Provided that high indistinguishability of the two photonic channels is assured and that simultaneous excitation of both atoms is negligible, detection of a single σ^- photon on the APD projects the two-ion state onto the maximally entangled state (6.3).

Following the detection of a Raman scattered σ^- photon, we coherently manipulate the generated two-atom state to allow for measurements in different bases. As shown in figure 6.6, this is done by first applying radio-frequency (RF) pulses that are resonant with the $|g\rangle \leftrightarrow |e\rangle$ transition of both atoms, see chapter 3.3 for more details. Discrimination between the two Zeeman sub-levels of the $6S_{1/2}$ state is finally done by shelving the

population of the $6S_{1/2,(m=-1/2)}$ state to the metastable $5D_{5/2}$ level using a narrowband 1.76 μm laser. The fluorescence rate on the $6S_{1/2} \leftrightarrow 6P_{1/2}$ transition [66] allows distinguishing between having no excitation at all ρ_{gg}, a single delocalized excitation ρ_{ge} or ρ_{eg} and two excitations ρ_{ee} in the two-atoms system. These events can all be separated with 98% probability, enabling us to efficiently reconstruct the relevant parts of the density matrix of the two-atom state. The 614 nm laser field then resets the ions to the $6S_{1/2}$ state and the same experiment is repeated 100 times.

6.3.4 Photon indistinguishability measurements

For efficient generation of the two-atom entangled state, the emitted photons must be indistinguishable in all degrees of freedom at the position of the triggering single-photon detector. We characterize their indistinguishability by measuring the first and second-order correlation functions and by estimating the overlap of their wavepackets.

Second-order correlation function of two atoms

In order to estimate the degree of the spatial and polarization indistinguishability of the photons coming from the two ions, we measure the second-order correlation function $g^{(2)}(\tau)$. To reach a time-resolution beyond the spontaneous decay time, we implemented a Hanbury-Brown-Twiss setup by splitting the atomic fluorescence into two parts with a non-polarizing beam-splitter and inserting a second avalanche photodiode (APD2), see figure 6.3.

The unnormalized second-order correlation function $G^{(2)}(\tau)$ reads

$$G^{(2)}_{\mathrm{Tot}}(\tau) = \langle \hat{E}^-(t)\hat{E}^-(t-\tau)\hat{E}^+(t-\tau)\hat{E}^+(t)\rangle, \tag{6.10}$$

where $\hat{E}^+$ and $\hat{E}^-$ are positive and negative frequency parts of the field operator $\hat{E}$ and τ is the time delay between two clicks at the two detectors. Field $\hat{E} = \vec{e}_1\hat{E}_1 + \vec{e}_2\hat{E}_2 e^{i\phi}$ corresponds to the coherent sum of the two field operators from atoms 1 and 2 with a phase difference ϕ and $\vec{e}_1$ and $\vec{e}_2$ are the polarization vectors. For this measurement, we do not stabilize the optical paths. By inserting the field expression into equation (6.10), and averaging over the optical phases ϕ, we obtain

$$G^{(2)}_{\mathrm{Tot}}(\tau) = 2(G^{(2)}(\tau) + |\vec{e}_1\vec{e}_2|^2|G^{(1)}(\tau)|^2 + \langle n\rangle^2), \tag{6.11}$$

where $G^{(1)}(\tau)$ is the (unnormalized) single ion first-order correlation function $G^{(1)}(\tau) = \langle \hat{E}^-(t)\hat{E}^+(t+\tau)\rangle$ and $\langle n\rangle$ is the mean number of photons on each APD.

By normalization of the second-order correlation function to the total detected countrate $\langle \hat{E}^-(t)\hat{E}^+(t)\rangle^2$ we get

$$g^{(2)}_{\mathrm{Tot}}(\tau) = \frac{1}{2}(g^{(2)}(\tau) + |\vec{e}_1\vec{e}_2|^2|g^{(1)}(\tau)|^2 + 1), \tag{6.12}$$

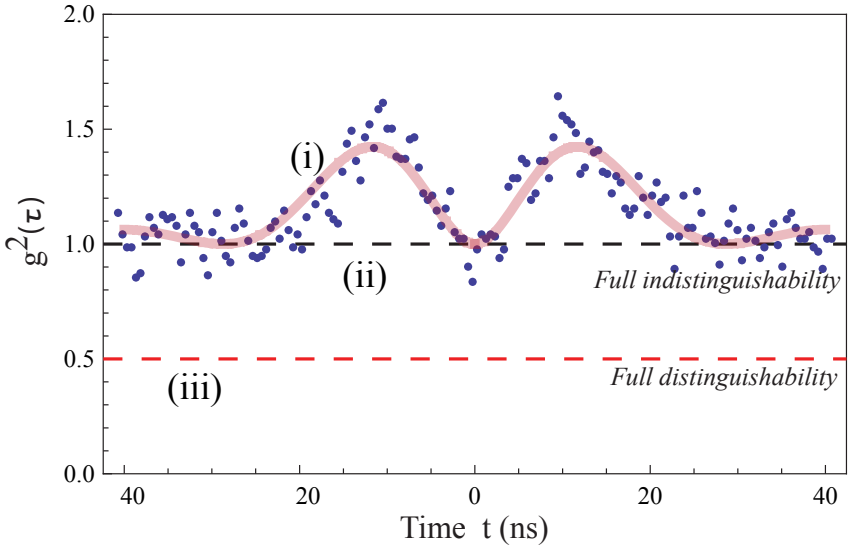

Figure 6.7: Measurement of the second order correlation function of the two ions. Trace (i) shows the experimental results and theoretical fit. Trace (ii) and (iii) are the expected values at $\tau = 0$ for fully indistinguishable/distinguishable emitters, respectively.

where $g^{(1)}$ and $g^{(2)}$ stand for first and second-order normalized correlation functions, respectively. For a two single atoms, $g^{(2)}(0) = 0$ (antibunching) and $g^{(1)}(0) = 1$, so the total second-order correlation function is equal to

$$g^{(2)}_{\mathrm{Tot}}(0) = \frac{1}{2}(1 + |\vec{e_1}\vec{e_2}|^2). \tag{6.13}$$

From here it follows that for two indistinguishable polarizations $g^{(2)}_{\mathrm{Tot}}(0) = 1$. The same analysis applies also for the spatial indistinguishability.

Figure 6.7, trace (i) shows the measured normalized second-order correlation function of the scattered light measured using the Hanbury-Brown-Twiss detection setup shown in figure 6.3-a). The measured value of the normalized second order correlation function in our experiment of $g^{(2)}_{\mathrm{Tot}}(0) = 0.98 \pm 0.07$ close to the theoretical value $g^{(2)}_{\mathrm{Tot}}(0) = 1$ proves a very high degree of spatial and polarization indistinguishability.

Measurement of the photon wavepackets

We estimate the overlap between the photons generated by the two ions in the spontaneous Raman process. We measure the correlation between the TTL-pulse at the output of programable-pulse-generator (PPG) which switches on the excitation Raman-beam and the arrival times of photons emitted from the two atoms using a high resolution

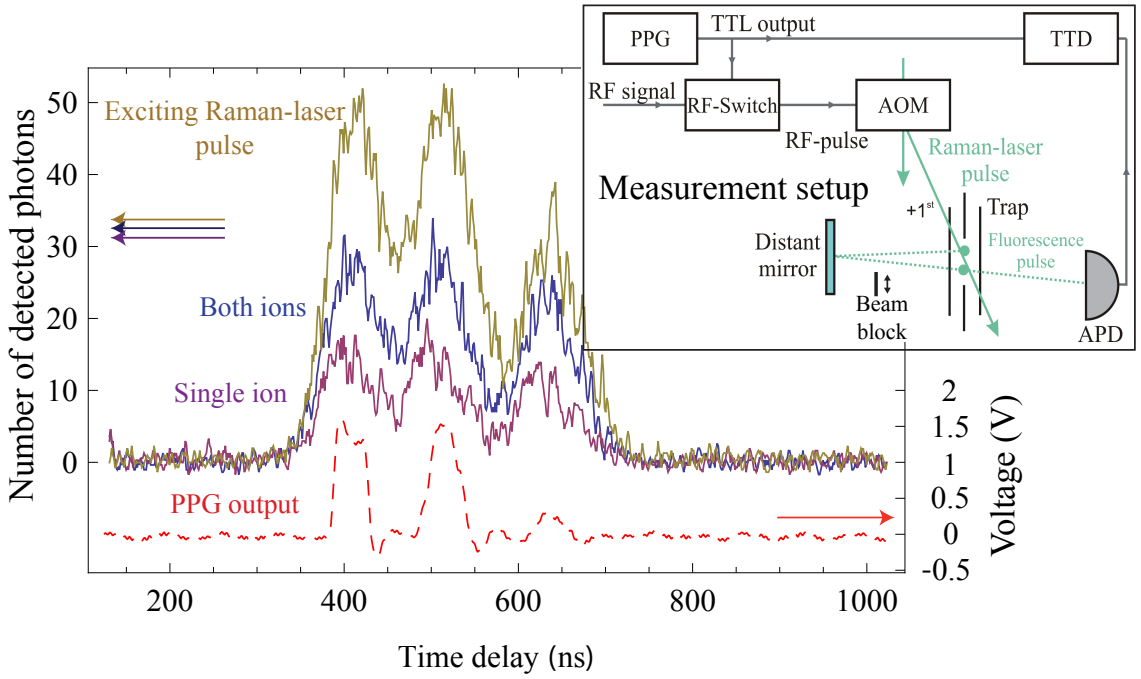

Figure 6.8: Correlation measurements between triggering TTL pulses at the output of the programable-pulse-generator (PPG) and arrival times of the Raman-scattered photons from the two ions. Measured yellow, blue and violet traces correspond to shapes of photons coming directly from an attenuated exciting Raman-laser pulse, fluorescence photons scattered from both ions and fluorescence photons scattered from one of the ions, respectively. The background noise is subtracted in all three measured traces. The shape of the wavepackets is determined by the output from the PPG, which switches the acousto-optic modulator (AOM). As can be seen in the measurement of the PPG digital output (red dashed trace), the generated pulse is very different from a desired TTL pulse for sub-microsecond pulse lengths. It generates three pulses separated by about 50 ns instead of single pulse.

(64 ps) time tagging measurement (TTD, PicoQuant GmbH, PicoHarp 300). We detect the exact arrival times of the TTL pulses and of the pulses generated by the avalanche-photodiode (APD) due to the photon detection events. The switching of the exciting Raman-beam using these TTL-pulses is achieved by switching of the RF-signal sent to the acousto-optic modulator (AOM, Brimrose, EM-160-25-493). In this way sub-microsecond lengths of the generated optical pulses are achieved, limited mostly by the acousto-optic modulator bandwidth of around 10 MHz and the shape of the pulse generated by the PPG [63].

The results of these measurements are presented in the figure 6.8. We measure the wavepackets of photons coming directly from an attenuated Raman beam and of fluorescence photons generated by both one and two ions. Shapes of the measured photon wavepackets are determined mostly by the imperfect TTL pulse shape generated by the PPG. The overall time delay between the generated TTL pulses and arrival times of the pulses generated by the detected photons was measured to be 380 ns, which is mostly given by the speed of the sound-wave in the acousto-optical modulator crystal. The length and the shape of the emitted photons from single ions on the Raman transition ($|g\rangle \rightarrow |i\rangle \rightarrow |e\rangle$) in the weak excitation regime and in the limit of the excitation pulse length being much longer than the decay time of the excited state $|i\rangle$ is determined by the time profile of the generated exciting laser pulse [155]. We measure the wavepackets of the photons inelastically scattered from single ion towards the detector by blocking the second ion emission in the mirror channel. The same measurement is done also with second ion unblocked, which allows us to estimate the overlap between the photons emitted from the two ions. The shape of the photons generated by the second ion is calculated by subtraction of the blue and violet traces in the figure 6.8. Normalized measured envelopes of photons generated by the two ions show very high overlap of $96 \pm 2\,\%$, limited mostly by the shot noise of the detected light. A small difference in the detection probabilities of photons from the two ions is caused by the lower detection probability of the photons from the second ion, which have to pass the high-NA lens twice and only after that they share the path and thus the losses of the photons coming from the first ion. The ratio between the detection probabilities of the photons coming from the two ions in our setup was estimated to be around 0.9. We make the detection probabilities the same by setting the fiber coupling efficiencies of the two ions to be approximately equal using a slight misalignment of the coupling of the fluorescence from the first ion to the single mode fiber.

The presented measurements of the photon wavepackets show that the shapes of photons coming from the two ions are the same and thus they should not affect our entanglement-generation measurements.

Phase interference measurements

In order to estimate the amount of motion induced which-way information, we measure the first-order correlation function. Figure 6.9, trace (i) shows the fluorescence intensity as a function of the distance d between the two ions in a regime where elastic scattering dominates. For comparison, trace (ii) shows the interference of the fluorescence of one ion with itself under the same cooling conditions. A contrast of up to 40% is observed for the interference of the elastic light scattered by the two ions. Temporal decoherence caused by the photon emission and absorption recoils [39, 66, 156, 157] is high enough to

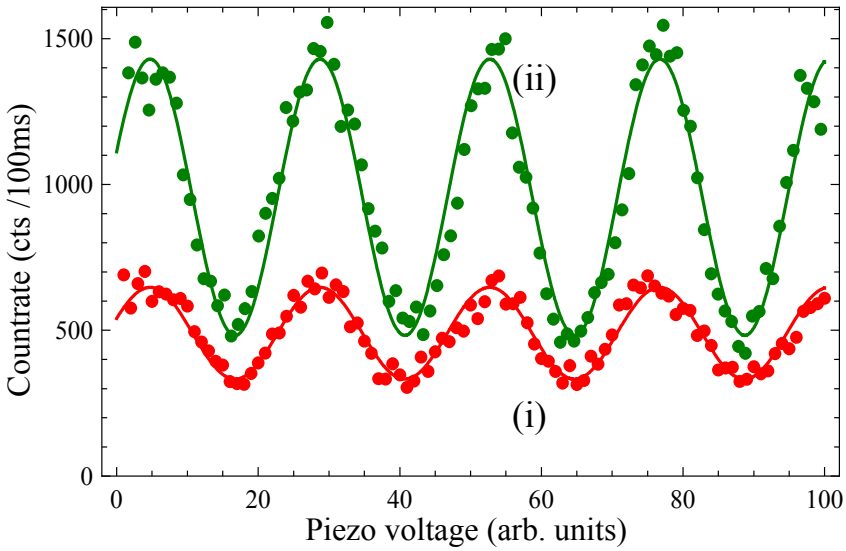

Figure 6.9: Measurement of the phase coherence of photons scattered by the two ions. Interference fringes when the fluorescence of one ion overlaps with itself (trace (ii)) and when the fluorescence light of both ions is superimposed (trace (i)), is measured in the limit of a weak excitation as a function of the phase difference between the two optical paths. The contrasts are 60% and 33% respectively, both limited mostly by atomic motion.

explain this contrast.

Conclusion

The measurement of the first and second-order correlation functions and measurements of the temporal overlap of photons emitted by two ions yield unambiguous separation between the major decoherence mechanisms. We have shown that photons emitted from the two atoms are almost perfectly indistinguishable in their spatial and polarization degrees of freedom and that the temporal overlap of their wavepackets is very high. The presented measurements of phase coherence and theoretical analysis presented in the chapter 6.5.2 lead us to the conclusion that which-way information given by atomic motion is the main source of distinguishability in our entanglement generation experiment.

6.4 Quantum state reconstruction

We need to estimate the generated state to evaluate the efficiency of the presented experimental realization of the single-photon entanglement generation protocol. This is usually

done by means of quantum state tomography, which consists of a set of measurements on identical copies of the unknown state. Using the frequencies of the different measurement outcomes, the state which most likely corresponds to the measured one can be estimated [158, 159].

6.4.1 Estimation of distant entanglement

In most quantum information experiments with single or multiple ion crystals, qubits are encoded in an electronic state on some long-lived atomic transition [160]. The phase of this state oscillates at a frequency corresponding to the energy difference between the two levels, typically at hundreds of THz for an optical transition. These qubits are controlled using narrowband lasers with frequency tuned close to the resonance frequency of the qubit transition. In the frame rotating with this fast oscillation, the relative phase between atomic qubit and control laser field can be defined with precision of up to $10^{-}4\,\mathrm{deg}$ limited by the technical accuracy of the phase-coherent switching [63, 69]. Qubits can be then initialized by pumping all the population into one of the energy eigenstates of the employed transition and by applying a laser pulse with some unknown but stable absolute phase. This phase defines the rotation axis of the qubit in the Bloch sphere. The relative phase of the following laser pulses can be easily set by controlling the phase of the radio-frequency signal applied to an acousto-optical modulator (AOM) acting on the laser beam in a phase-coherent way. Within the coherence length of the qubit, an arbitrary state can then be created and measured by keeping track of relative phase and amplitude of the RF-signal applied to the AOM, see figure 6.10.

However, when creating the state of atomic qubits by a laser-phase independent method, for example by interference and a detection process as in our entanglement generation experiment, the phase of the generated state generally depends on other parameters, for example the time of the photon detection, and is independent of the phase of the analyzing laser. Therefore, the phase of the qubit states is not correlated to the absolute phase of the laser which could be used for the quantum state tomography on optical transition qubit. Absolute phase of the laser used for the qubit rotations in the state tomography procedure would be in this case random with respect to the phase of the generated state. Full state tomography thus cannot be then performed on the entangled states generated by single or two-photon entangling protocols if the qubits encoded on optical transitions.

There are several ways to prove that two distant atoms are entangled, here is a short summary:

- Employment of a radio-frequency or microwave atomic transition for encoding the qubits, because the absolute phase of the applied radiation at these frequencies can be well controlled. If additionally the individual ion addressing can be realized, for

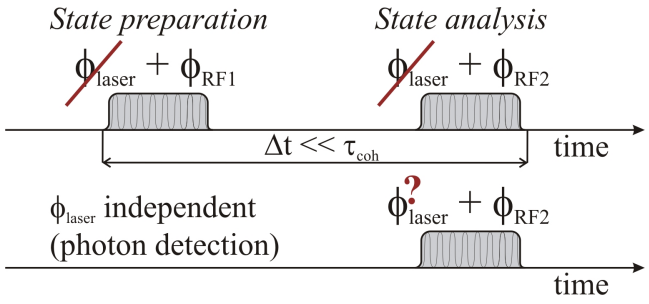

Figure 6.10: Illustration of the two experimental situations in quantum state tomography of atomic qubits. When the state of the qubits is prepared and reconstructed using the same laser field within the coherence time of the system τ_{coh}, the whole procedure is independent of the absolute phase of the laser. However, if the state of the atomic qubits is prepared using some procedure which is independent of the absolute phase of the laser field, for example by detection of the emitted fluorescence photon, the full quantum state tomography cannot be easily realized on optical transitions.

example for spatially separated ions in distant traps, full quantum tomography of the generated state is possible.

- In order to estimate the overlap of the generated state with the desired entangled state it is sufficient to measure only the parts of the density matrix which contribute to this overlap. For some particular entangled states, for example $|\Psi^+\rangle$, these parts of the density matrix can be accessed by a sequence of global qubit rotations, independent of the absolute phase of the applied laser field. We use this method in our experiment and a detailed theoretical description can be found in chapter 6.4.2.

- Complementarity relations between the visibility of the interference of spontaneously emitted photons from the two atoms and the amount of concurrence as an entanglement measure can be used for particular atomic level schemes. In our experiment, this would correspond to the scattering of a single photon from the two entangled atoms following the Raman process ($|e\rangle \rightarrow |i\rangle \rightarrow |g\rangle$). Observation of the phase interference between these photons can be then quantitatively related to a lower bound of the amount of entanglement in the system [161, 162]. The main disadvantage of this approach is the small detection efficiency of scattered photons which is proportional to the overall success rate of the entanglement generation process P_{succ}.

6.4.2 Parity measurements

We perform a Ramsey-type interference measurement that probes the coherence between the $|ge\rangle$ and $|eg\rangle$ states to estimate the fidelity of our experimentally generated state with the maximally entangled state $|\Psi^+\rangle$. This is realized by a measurement of the parity operator

$$\hat{P} = \hat{p}_{gg} + \hat{p}_{ee} - \hat{p}_{eg} - \hat{p}_{ge}, \tag{6.14}$$

where $\hat{p}_{ij}$ are the projection operators on states $|ij\rangle$, $i, j \in \{g, e\}$ in different bases [163].

The general state of our two-qubit system can be described by the 4×4 Hermitian matrix

$$\hat{\rho} = \begin{pmatrix} \rho_{gg} & \rho_{gg,eg} & \rho_{gg,ge} & \rho_{gg,ee} \\ \rho^*_{gg,eg} & \rho_{eg} & \rho_{eg,ge} & \rho_{eg,ee} \\ \rho^*_{gg,ge} & \rho^*_{eg,ge} & \rho_{ge} & \rho_{ge,ee} \\ \rho^*_{gg,ee} & \rho^*_{eg,ee} & \rho^*_{ge,ee} & \rho_{ee} \end{pmatrix} \tag{6.15}$$

Measurement of the parity operator $\hat{P}$ on state $\hat{\rho}$ preceded by the collective rotation $\hat{R}(\pi/2, \phi)$ defined in (3.4) can then be formally written as $\mathrm{Tr}[\hat{P}\hat{R}(\pi/2, \phi)\hat{\rho}(\hat{R}(\pi/2, \phi))^+]$.

For $|\Psi^+\rangle$ we get the rotated state

$$\hat{R}(\pi/2, \phi)|\Psi^+\rangle = \frac{1}{\sqrt{2}}(|ee\rangle + e^{2i\phi}|gg\rangle) \equiv |\alpha\rangle \tag{6.16}$$

and thus

$$\mathrm{Tr}(\hat{P}|\alpha\rangle\langle\alpha|) = 1 \tag{6.17}$$

for all ϕ. A parity measurement on the $|\Psi^+\rangle$ entangled state is therefore invariant with respect to the change of the phase ϕ of the rotation pulse $\hat{R}(\pi/2, \phi)$. In order to measure the parity oscillations for this state, we first have to rotate by a global $\hat{R}(\pi/2, \pi/2)$ pulse, corresponding to a $\hat{\sigma}_y$ rotation on both qubits with the pulse area of $\pi/2$.

It can be shown that a peak-to-peak value of the parity measurement oscillation higher than one with an oscillation period of $\phi = \pi$ on two qubits is a sufficient condition for proving that the measured bi-partite system is entangled [163].

We evaluate the fidelity $F = \langle\Psi^+|\rho|\Psi^+\rangle$ with the maximally entangled state $|\Psi^+\rangle$ to quantify the amount of entanglement. It reads

$$F = \frac{1}{2}[\rho_{ge} + \rho_{eg} + 2\mathrm{Re}(\rho_{eg,ge})]. \tag{6.18}$$

The fidelity thus depends only on the diagonal populations ρ_{ge} and ρ_{eg} and on the real part of the off-diagonal term $\rho_{eg,ge}$ that expresses the mutual coherence between them. All these terms can be accessed using collective rotations $\hat{R}$ followed by the parity operator measurement. Diagonal terms ρ_{ge} and ρ_{eg} can be estimated directly by measuring populations without any prior RF-pulse application. The coherence term $\rho_{eg,ge}$ however

Number of pulses	Pulse sequence	Measurement result
0	–	$\rho_{gg} + \rho_{ee} - (\rho_{eg} + \rho_{ge})$
1	$\hat{R}(\pi/2, 0)$	$2\mathrm{Re}(\rho_{\mathrm{ge,eg}} - \rho_{\mathrm{gg,ee}})$
	$\hat{R}(\pi/2, \pi/4)$	$2(\mathrm{Re}(\rho_{\mathrm{ge,eg}}) + \mathrm{Im}(\rho_{\mathrm{gg,ee}}))$
	$\hat{R}(\pi/2, \pi/2)$	$2\mathrm{Re}(\rho_{\mathrm{ge,eg}} + \rho_{\mathrm{gg,ee}})$
2	$\hat{R}(\pi/2, \pi/2)\hat{R}(\pi/2, 0)$	$2\mathrm{Re}(\rho_{\mathrm{ge,eg}} - \rho_{\mathrm{gg,ee}})$
	$\hat{R}(\pi/2, \pi/2)\hat{R}(\pi/2, \pi/2)$	$\rho_{gg} + \rho_{ee} - (\rho_{eg} + \rho_{ge})$

Table 6.1: Examples of the measurement sequences. Expectation value of the parity operator after applying various global RF-pulse sequences to the ions.

cannot be measured with a single global pulse sequence, because it is always measured together with the coherence term $\rho_{gg,ee}$. A simple way to separate their respective contributions to the measured parity signal is to measure the parity operator value after a single rotation $\hat{R}(\pi/2, \phi)$ for different phases ϕ. Invariance of the measured parity value with respect to the phase ϕ proves that the only coherence term contributing to the measured coherence signal is the desired $\rho_{eg,ge}$. Table (6.1) shows examples of some relevant RF-pulse rotation sequences and the corresponding parts of the density matrix ρ contributing to the measured signal.

6.5 Entanglement generation results

6.5.1 Experimental analysis of the generated state

Figure 6.11-a) shows the measurement results obtained without RF analysis pulses. We measure the number of excited atoms after detection of a triggering photon what gives us the diagonal terms of the density matrix (6.15) corresponding to the populations of the generated state. The results tell us that 89±3% of all the triggering events signal that only one of the atoms was excited to the $|e\rangle$ state. The remaining 10% errors are caused by APD dark counts and double excitation of the ions. Our detection process using a single photomultiplier doesn't allow us to resolve individual ρ_{eg} and ρ_{ge} populations directly, but it tells us the number of the excited atoms, which correspond to the populations ρ_{gg},ρ_{eg} and $(\rho_{eg} + \rho_{eg})$. As demonstrated in equation (6.18), this is sufficient information about the populations of the generated state for the estimation of the fidelity with the state $|\Psi^+\rangle$. Nevertheless, we also experimentally proved that ρ_{eg} and ρ_{ge} are approximately the same, since they depend only on the excitation probabilities and overall detection efficiencies from the two ions, which are the same in our experiment (see section 6.18).

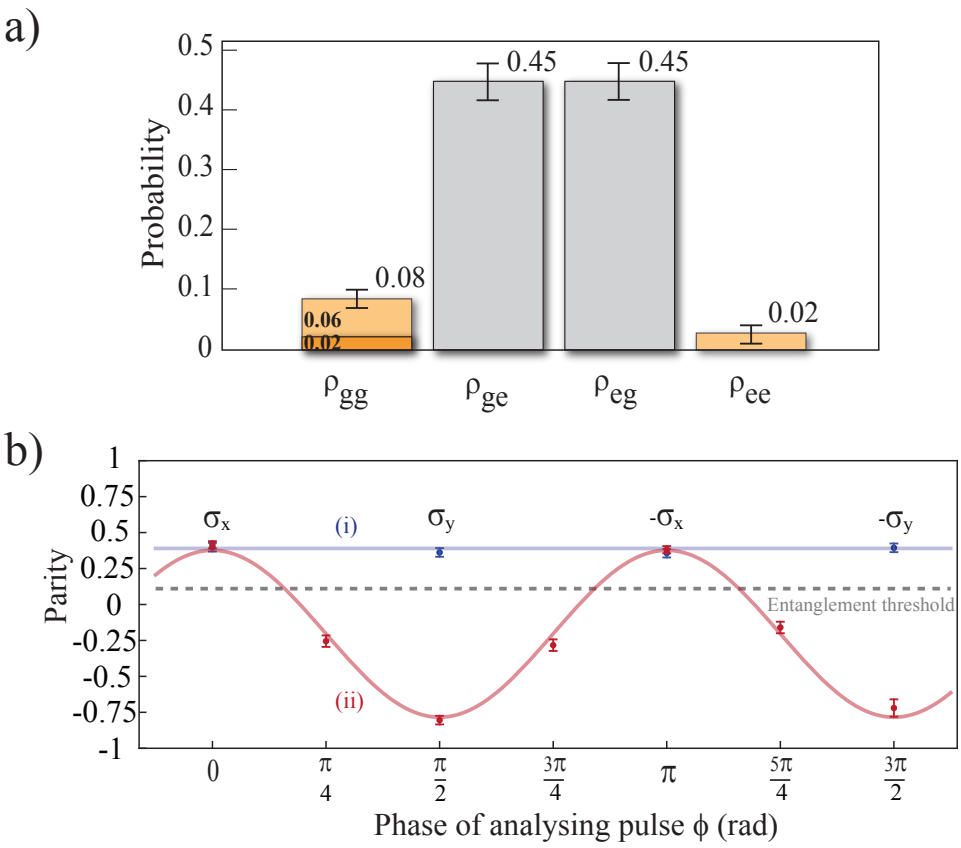

Figure 6.11: Characterization of the entangled state. a) Two-atom state populations after the detection of a σ^- photon showing that the total probability of measuring the state with a single excitation is 90%. b) Parity measurements as a function of the RF-phase. Trace (ii) corresponds to the measurement of the atomic populations after two global rotations $\hat{R}^g(\pi/2, \pi/2)\hat{R}^g(\pi/2, \phi)$. In the measurement of trace (i) only a single global RF-pulse $\hat{R}^g(\pi/2, \phi)$ is applied. The dashed line shows the threshold for entanglement, estimated from the measured diagonal terms. This threshold corresponds to the minimal value of the coherence term $2\mathrm{Re}(\rho_{eg,ge})$ which guarantees the presence of entanglement for the measured populations $(\rho_{eg} + \rho_{ge})$. Individual points of the measured parity signals at different phases ϕ are explained in the table 6.1.

Therefore we can estimate also the individual populations as $\rho_{eg} = \rho_{ge} = 1/2(\rho_{eg} + \rho_{ge})$.

In order to measure the quantum coherence of the generated state, we then apply two consecutive global RF-pulses, each corresponding to the rotation

$$\hat{R}(\theta, \phi) = \exp\left(-i\frac{\theta}{2}(\cos\phi\hat{S}_x + \sin\phi\hat{S}_y)\right), \tag{6.19}$$

where $\hat{S}_{x,y} = \hat{\sigma}^{(1)}_{x,y} \otimes \hat{\sigma}^{(2)}_{x,y}$ is the global Pauli operator acting on both ions. The rotation angle θ and rotation axis ϕ on the Bloch sphere are determined by the duration and the phase of the RF pulses, respectively. We first apply the pulse $\hat{R}(\pi/2, \pi/2)$ which performs the unitary rotation $\hat{R}(\pi/2, \pi/2)|\Psi^+\rangle \rightarrow |\Phi^-\rangle$, where $|\Phi^-\rangle = \frac{1}{\sqrt{2}}(|gg\rangle - |ee\rangle)$. A second RF-pulse with same duration but with a phase ϕ then performs the rotation $\hat{R}(\pi/2, \phi)|\Phi^-\rangle$. After shelving the state $|e\rangle$ to the metastable level $5D_{5/2}$, we scatter light from both ions on the cooling transition. From the measured fluorescence rate at different phases ϕ we extract the mean value of the parity operator $\hat{P}$.

Figure 6.11-b), trace (ii), shows the results of the parity operator measurements preceded by two global RF rotations $\hat{R}(\pi/2, \pi/2)\hat{R}(\pi/2, \phi)$. The measured parity clearly oscillates as a function of phase ϕ with contrast of 58.0±2.5% and period of π, a proof that we indeed succeed in preparing an entangled two-ion state close to $|\Psi^+\rangle$ [163]. The mean value of the parity operator at zero phase $\langle\hat{P}\rangle_{\phi\rightarrow 0}$ corresponds to the difference between the inner parts and outer-most coherence terms of the density matrix. We evaluate it to be $2\mathrm{Re}(\rho_{\mathrm{ge,eg}} - \rho_{\mathrm{gg,ee}}) = 0.38 \pm 0.03$. This number proves that there is a coherence in our system. However, to precisely quantify the fidelity of our state with $|\Psi^+\rangle$, we need to estimate solely the real part of the coherence $\rho_{ge,eg}$ itself. The contribution of the coherence term $\rho_{gg,ee}$ to the measured value can be excluded by measurement of the parity without the first RF rotation, see table 6.1. Trace (i) of figure 6.11-b) shows the expectation value of the parity as a function of the phase ϕ of the single RF-pulse. The invariance of the measurement result with respect to the phase ϕ proves that $\rho_{gg,ee} = 0 \pm 0.03$, so that indeed only the coherence corresponding to the state $|\Psi^+\rangle$ is measured. We finally estimate that the fidelity of the generated state with the maximally entangled state $|\Psi^+\rangle$ is $F = 63.5 \pm 2\%$. The threshold for an entanglement is thus surpassed by more than six standard deviations. The parameters of the measured parity function are in general given by the measurement sequence and by the state of the qubits. For the case of the two-qubit entangled state $|\Psi^+\rangle$ and the sequence corresponding to two consecutive rotations $\hat{R}(\pi/2, \phi)\hat{R}(\pi/2, \pi/2)$, the measurement of the parity operator $\hat{P}$ with the phase values of $\phi = n\pi, n \in \mathbf{Z}$ and $\phi = \pi/2 + n\pi, n \in \mathbf{Z}$ gives $\langle\hat{P}\rangle_{\phi=n\pi} = 1$ and $\langle\hat{P}\rangle_{\phi=\pi/2+n\pi} = -1$, respectively. The values of the parity operator at $\langle\hat{P}\rangle_{\phi=n\pi}$ and $\langle\hat{P}\rangle_{\phi=\pi/2+n\pi}$ correspond then directly to the measurement of the coherence and population of the $|\Psi^+\rangle$ state, see also the table 6.1. If the populations are much higher than the coherence between them and if we assume all other parts of the two-qubit density matrix to be zero, we get parity oscillations which are strongly asymmetric with respect to the zero value of the parity operator. This is the case also in our measurements presented in the figure 6.11-b), trace (ii). In the extreme example where populations would be perfect but with no coherence, the parity signal would oscillate in the interval $[-1, 0]$.

The coherence between the $|ge\rangle$ and $|eg\rangle$ states of $38 \pm 3\%$ is limited by three main processes. First, imperfect populations of $|ge\rangle$ and $|eg\rangle$ states set a limit of 89% [164].

Around 4% of the coherence loss can be attributed to the finite coherence time of the individual atomic qubits (120 μs) due to collective magnetic field fluctuations. Although the generated $|\Psi^+\rangle$ state is intrinsically insensitive against collective dephasing [165,166], a loss of coherence is indeed expected after a rotation of $|\Psi^+\rangle$ out of the decoherence-free subspace. The highest contribution to the coherence loss can be attributed to atomic motion, which can provide information about which atom emitted the photon. Around 55% of the coherence is lost due to the atomic recoil kicks during the Raman scattering as explained in the analysis section 6.5.2. Error bars in the presented measurements results correspond to one standard deviation and are estimated statistically from several experimental runs each giving approximately 120 measurement outcomes. Up to 60 % of the measurement error is caused by the quantum projection noise. Additional uncertainty comes from slow magnetic field drift with a magnitude of several tens of nT making the RF-driving off-resonant by tens of kHz.

6.5.2 Quantum coherence

The fidelity of the maximally entangled state $|\Psi^+\rangle$ with the experimentally generated one is given by [37]

$$F = \frac{1}{2}\kappa(1 + F_{\mathrm{dyn}}e^{-4t/\tau}). \tag{6.20}$$

Here κ is a factor taking into account imperfect populations of the $|ge\rangle$ and $|eg\rangle$ states mimicked mostly by the detector dark-counts and double-excitations of ions due to imperfect setting of the Raman-beam polarization and finite value of the excitation probability p_e. The latter gives a double-excitation rate of $3p_e^2 \approx 1.5 \times 10^{-2}$. F_{dyn} describes the decoherence due to atomic motion (dynamical fidelity factor) and $e^{-4t/\tau}$ expresses the loss of coherence due to the finite coherence time τ of each individual qubit [167]. Time t is the time relevant for the decoherence process, which in our case corresponds to the time difference between the rotation of the generated state out of the decoherence-free subspace and realization of the (parity) rotation using second analyzing pulse. The overall fidelity F is related to the respective density matrix elements as defined in (6.20), through

$$\rho_{ge} + \rho_{eg} = \kappa, \tag{6.21}$$

$$2\mathrm{Re}(\rho_{eg,ge}) = \kappa F_{\mathrm{dyn}}e^{-4t/\tau}. \tag{6.22}$$

The main factor contributing to the decoherence is atomic motion. One can show that

$$F_{\mathrm{dyn}} = e^{\langle[\vec{q}_1\cdot\vec{u}_1 - \vec{q}_2\cdot\vec{u}_2]^2\rangle/2}, \tag{6.23}$$

where $\vec{q}_{1,2} = \vec{k}^{1,2}_{\text{out}} - \vec{k}_{\text{in}}$ and $\vec{k}^{1}_{\text{out}} \approx -\vec{k}^{2}_{\text{out}}$. $\vec{k}^{1,2}_{\text{out,in}}$ is the wavevector of the 493 nm light driving (in) and emitted (out) by atom 1 and 2 respectively. $\vec{u}_{1,2} = \vec{R}_{1,2} - \vec{R}^{O}_{1,2}$ are the displacements of atom 1 and 2 away from their equilibrium positions $\vec{R}^{O}_{1,2}$. Decomposing the ion crystal motion into the normal modes, one gets

$$\vec{q_1} \cdot \vec{u_1} - \vec{q_2} \cdot \vec{u_2} = -2k_{\text{out}}\hat{r}^{\text{rad}}_{\text{cm}} + 2k_{\text{in}} \cos\varphi \hat{r}^{\text{rad}}_{\text{rel}} - 2k_{\text{in}} \sin\phi \hat{r}^{\text{ax}}_{\text{rel}} \tag{6.24}$$

where $\hat{r}^{\text{rad,ax}}_{\text{cm,rel}}$ are the position operators of the quantized harmonic oscillator modes of the two-ion crystal. cm and rel denote the center of mass and stretch/rocking modes, respectively, and rad, ax are the radial and axial coupled modes. φ is the angle (in our case 40 degrees) between the Raman excitation laser and the two-ion crystal axis. Inserting the expression (6.24) into equation (6.23), we then get

$$F_{\text{dyn}} = e^{-2(k\sigma)^2}, \tag{6.25}$$

where

$$\sigma = \sqrt{(\sigma^{\text{rad}}_{\text{cm}})^2 + \frac{1}{2}(\sigma^{\text{rad}}_{\text{rel}})^2 + \frac{1}{2}(\sigma^{\text{ax}}_{\text{rel}})^2}. \tag{6.26}$$

Each σ corresponds to the mean extent of the atomic wave packet. For instance, we have $\sigma^{\text{rad}}_{\text{cm}} = \sqrt{(2\overline{n}^{\text{rad}}_{\text{cm}} + 1)\langle 0|(r^{\text{rad}}_{\text{cm}})^2|0\rangle}$, here $\langle 0|(r^{\text{rad}}_{\text{cm}})^2|0\rangle$ is the mean extension $\sqrt{\hbar/(2m\omega^{\text{rad}}_{\text{cm}})}$ of the coupled harmonic oscillators in the ground state, and $\overline{n}$ is the mean phonon number in a given mode. m is the atomic mass, and ω the frequency of the oscillator, which we estimated for all modes using the spectroscopy on the quadrupolar transition to be $(\omega^{\text{rad}}_{\text{cm}}, \omega^{\text{ax}}_{\text{rel}}, \omega^{\text{rad}}_{\text{rel}}) = 2\pi(1.5, 0.9, 1.1)$ MHz. Taking the mean phonon number of each mode to be around 12 for a Doppler cooled ion-crystal [66], we get

$$F_{\text{dyn}} = 0.45. \tag{6.27}$$

In the limit of a weak excitation, κF_{dyn} also directly corresponds to the visibility of the two-ion interference. The effect of motion-induced decoherence can be reduced by cooling the radial modes to the motional ground state [66] or by choosing a forward Raman scattering scenario [37]. The difficulty of the last option in our particular setup is that light from the Raman excitation can leak through the detection channel during the excitation.

The effect of the finite coherence times of the individual qubits is included in the coherence factor $e^{-4t/\tau}$. In our experiment, the coherence time of the individual RF qubits is limited mostly by the ambient magnetic field fluctuations. For each atom, we measured it to be 120 μs. The noise seen by both ions when they leave the decoherence-free subspace is mostly correlated [167]. For our experiment, this amounts to a decrease of our coherence on average by factor of about $e^{-4t/\tau} = 0.96$.

Last, the coherence and overall fidelity of the generated entangled state is limited by the imperfect populations of the desired $|ge\rangle$ and $|eg\rangle$ states. This is effectively accounted for in the overall fidelity (6.20) by the factor κ, which we estimated from the populations measurements to be 0.89±0.03. This is in good agreement with the excitation probability $p_e = 0.07 \pm 0.03$ of each ion and the measured dark-counts of our avalanche photodiode of 10 counts/s.

By inserting all the mentioned inefficiencies into the equation (6.20), we get the overall fidelity of our measured state with the maximally entangled state $|\Psi^+\rangle$ to be $F = 0.62$, in good agreement with the measured fidelity of 0.635 ± 0.02.

6.5.3 Phase tunability

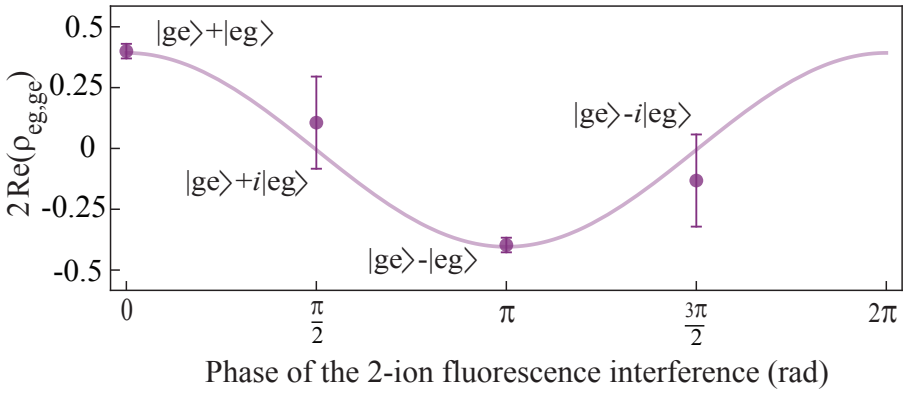

Figure 6.12: Characterization of the entangled state. a) Real part of the coherence between the $|ge\rangle$ and $|eg\rangle$ states as a function of the phase of the optical path difference between the two ions. Measured points are marked by the corresponding entangled states.

An intrinsic feature of the realized entangling protocol is the dependence of the generated entangled state phase on the optical path difference between the two ions. To demonstrate this, we measure the real part of the coherence between the $|ge\rangle$ and $|eg\rangle$ states as a function of the phase factor kd, where $d/2$ corresponds to the ion-mirror distance as depicted in the figure 6.3 and can be adjusted by shifting the piezo-mirror. The experimental procedure for estimation and setting of the entangled state phase is explained in section 6.3.2. Figure 6.12 reveals a large change of the real part of the coherence from positive to negative values when going from the maximum to the minimum of the interference signal, in agreement with the e^{ikd} phase dependence of the entangled state.

6.5.4 Entanglement generation rate

An important feature of the single-photon heralding mechanism is the high entanglement generation rate that can be achieved. With our experimental set-up, the single photon detection scheme indeed yields a higher rate compared to the two-photon scheme proposed by Simon et al. [38, 146]. The probability of preparing an entangled state depends on the probability of the single photon detection and the Raman scattering probabilities [146], which in our case gives a total of $P_{\text{succ}} = 1.1 \times 10^{-4}$ for each trial run. With an experimental duty cycle of 2.3 kHz, this corresponds to 15.4 successful entanglement generation events/minute, which is in good agreement with the experimentally observed 14±1.5 events/minute.

The efficiency for detecting a single Raman-scattered photon in our setup was estimated to be $\eta_D = 8 \times 10^{-4}$. It was derived from the detection probability of a single Raman scattered photon given by the collection efficiency of our lenses (~ 0.04), the single-mode fiber coupling efficiency (~ 0.1) and by the avalanche-photodiode detection efficiency (~ 0.6). Additional factors of 0.5 and 0.66 come from the polarization filtering of the unwanted π-polarized photons and from the probability of decaying back to the $|g\rangle$ state after the Raman pulse excitation, respectively. The actual entanglement rate may thus be estimated. With our single ion excitation probability $p_e = 0.07 \pm 0.03\%$, the overall probability for detecting a single photon from one of the two ions is then $P_{\text{succ}} = 2p_e\eta_D = 1.1 \times 10^{-4}$. For comparison, the heralding entanglement scheme proposed by Simon et al. [38] would give for our experimental setup approximately $P_{\text{succ}} \approx 2\eta_D^2 = 1.3 \times 10^{-6}$, so about two orders of magnitude smaller success probability of entanglement generation in a given experimental trial. For simplicity, we assumed here $p_e = 1$ for the two-photon scheme and an additional factor of two comes from the two possible contributions to coincidence detection events.

6.6 Conclusion

We have demonstrated a fundamentally new protocol for generating heralded entanglement between two ions. This was achieved via the scheme proposed in the seminal work of Cabrillo et al. [37] where two atoms are entangled with the emission and detection of only one photon. Such a single-photon scheme allowed us to reach a rate of entanglement generation of 14 events/minute, more than two orders of magnitude higher than the rate obtainable with protocols relying on a two-photon coincidence events with our experimental parameters. The maximally entangled state $|\Psi^+\rangle$ is produced with a fidelity of 63.5 % limited mostly by residual atomic motion. These results can be improved by cooling all of the involved motional modes close to their ground state [66] or choosing a different excitation direction to minimize residual which-way information. By nearly

collinear alignment of the Raman excitation laser with respect to the detection direction, the residual which-way information stored in the atomic motion can be completely suppressed due to cancellation of the absorption and the emission recoil kicks.

There are some obvious questions regarding the technical difficulties related to phase stability requirements and photon recoil problems of the single-photon entanglement generation scheme. For generation of the entanglement between distant atoms, the paths of the excitation and detection channels need to be interferometrically stable. This issue has been addressed by the community developing fiber links for comparing remote optical clocks. Recently, coherent laser light transfer over more than 900 km has been shown with a precision exceeding the requirements for our scheme [168]. The problem of a which-way information available due to the atomic recoil upon scattering of single photon can be eliminated by changing the geometry of the system. We are convinced that these requirements are practically much easier to achieve than the realization of experimental setups with very high detection efficiencies proposed as a possible solution to the low success rate of the two-photon scheme.

These improvements, together with the experimental results presented, will enable efficient creation and distribution of entanglement between distant sites with well-defined and controllable atomic qubits. Such entanglement generation corresponds to an essential building block of scalable quantum communication [87] and distributed quantum computation [17–19] architectures with single atoms.

7 Conclusion and outlook

7.1 Conclusion

The work presented in this thesis aimed to bring more insight into the fundamental interaction between light and single atoms in free space. We have made several technical improvements, which led to the realization of high-fidelity single-qubit operations on magnetic dipole and electric quadrupole transitions of $^{138}Ba^{+}$. These achievements, together with a relatively high collection efficiency of the optics employed in our ion trapping setups, enabled several experiments that studied both the probabilistic and deterministic ways of quantum information processing with single atoms and photons. We have experimentally studied the influence of atomic motion on the phase coherence of emitted fluorescence, which can in turn be used as an estimator of the atomic temperature itself. Next, we have realized a free-space coupling of a weak coherent beam to a single atom, which enabled us to observe an electromagnetically-induced transparency and the operation of a single atom as an optical mirror of a Fabry-Pérot-like cavity. Finally, we have realized a scheme for entangling distant atoms by single photon scattering and detection.

Coherent manipulations and sideband cooling of $^{138}Ba^{+}$

We have improved the experimental setup by implementing 1.76 μm fiber and 614 nm diode laser systems and their frequency stabilization to optical resonators in order to achieve coherent operations on quadrupole $6S_{1/2} \leftrightarrow 5D_{5/2}$ and sideband cooling. We have realized the electronic setup for driving magnetic dipole transition between the two Zeeman substates of the $6S_{1/2}$ level with frequency splitting of 11.5 MHz. Furthermore, we have realized fast switching and generation of pulse sequences using a programmable pulse generator. These technological advancements enabled us to demonstrate efficient qubit rotations on the optical and RF transitions of $^{138}Ba^{+}$ necessary for further realization of probabilistic quantum networking. Visibilities of Ramsey interference fringes were close to 100 % for both qubit transitions and for short time delays between the two Ramsey pulses. For longer delays the main limitation on coherence was imposed by fluctuations of the ambient magnetic fields at 50 Hz. A possible way to reduce magnetic field fluctuations at the position of the ion could be the utilization of passive magnetic

field shielding as demonstrated in another experimental setup in our group [67], where measurements showed suppression of the magnitude of these fluctuations by more than 40 dB. Another solution, perhaps easier to implement in the existing experimental apparatus, corresponds to an active stabilization of the magnetic field at the position of an ion. We have also demonstrated sideband cooling of a single Barium ion on the $6S_{1/2} \leftrightarrow 5D_{5/2}$ quadrupolar transition close to its motional ground state with cooling times of several milliseconds. The speed and efficiency of the cooling process were mainly limited by the small corresponding Lamb-Dicke parameters.

Interferometric thermometry

We have demonstrated a strong dependence of the interference contrast in our half-cavity setup on the ion's motional amplitude and introduced a new thermometry method based on measurement of the first-order coherence. The achieved single phonon resolution of temperature measurements suggest applications of our method for experiments with Doppler and sub-Doppler cooled ions, where the usual thermometry techniques based on the sideband-resolved spectroscopy are not available.

Free-space atom-light coupling

The main purpose of experiments presented in chapter 5 was investigation of the coupling of a weak near-resonant coherent probe beam to a single Barium ion in a free space and demonstration of related quantum optical phenomena. The coupling was mediated by a single objective covering 4 % of the full solid angle. We have demonstrated direct extinction of the probe field manifested by the suppression of its intensity by 1.3 %. The amount of extinction was mainly limited by the numerical aperture of the employed objective, atomic motion and imperfect spatial mode matching of the probe mode with atomic dipole emission pattern. We hope to dramatically improve the amount of extinction by designing a new experimental setup employing the lenses covering more than 15 % of the full solid angle. Better spatial mode matching of the probe beam with atomic emission pattern can be achieved using spatial light modulators. Next, we demonstrated electromagnetically-induced-transparency (EIT) by observation of inhibition of the extinction by almost 75% for a 650 nm control field tuned to a two-photon resonance with the probe. We demonstrated the operation of a single ion as an optical mirror of a Fabry-Pérot-like cavity by observation of the phase interference between the part of the probe beam reflected from the dielectric mirror and the part reflected from the ion. This experiment enabled us to study quantum-electrodynamics effects in a novel regime where both the modification of the vacuum mode density at the position of an ion and free-space coupling of the probe beam play a role.

Probabilistic entanglement

We have demonstrated a new protocol for generation of heralded entanglement between two ions as proposed in the seminal paper by Cabrillo et al. [37]. Ions were entangled by Raman emission and indistinguishable detection of a single photon. The entangled state $|\Psi^+\rangle$ has been generated with a fidelity of 63.5 % and rate of 14 entanglement events/minute, corresponding to more than two orders of magnitude gain, when compared to the rate obtainable with protocol relying on a two-photon coincidence events with our experimental parameters. The fidelity of the maximally entangled state was limited mostly by residual atomic motion. This could be improved by choosing the excitation direction collinear with the detection direction of emitted Raman photons, which minimizes residual which-way information due to the atomic recoil.

The presented results have direct implications for long distance quantum information processing in both deterministic and probabilistic protocols. Quantum memories, where the quantum state is deterministically exchanged between atoms and light fields form an essential part of quantum repeater architectures [21, 117] and EIT seems to be promising method to achieve this transfer [117]. The demonstration of a distant entanglement generation protocol will enable efficient creation and distribution of entanglement between remote sites with controllable atomic qubits. Realizations of the experiments presented here pave the way towards scalable quantum communication [87] and distributed quantum computation [17–19] architectures with single atoms and photons in a free space.

7.2 Outlook

The experiments presented and technical tools developed in this thesis will enable advanced studies of atom-light interactions and quantum electrodynamics in free space. The efficient collection of resonance fluorescence is the key to all of the experiments presented here. The collection efficiencies are restricted to a few percent by both the geometries of the employed traps and the solid angle of our high-NA optics and further improvements in the existing apparatuses would be difficult. Therefore, many of these experiments would benefit from the realization of a new experimental apparatus including a Paul trap with much better optical access to the emitted fluorescence.

Realizing a similar setup with higher numerical aperture optics would allow for more efficient generation of distant entanglement using the presented single-photon entangling protocol. Presented results of entanglement generation could be realized with greater physical distance between the ions by trapping them in two separate traps, which would much better correspond to the realistic quantum networking conditions. Furthermore, the collinear excitation of the Raman transition with respect to the detection direction, which has potential to strongly improve the fidelity of the generated state, would be much

easier to realize in such a setup.

With small modifications, the realized experimental scheme for entanglement generation could be used as a quantum memory for polarization states of single photons, similar to the experiments reported with atomic ensembles [119]. This memory would have some inherent advantages compared to systems based on optically thick ensembles of neutral atoms, in particular the absence of decoherence due to the diffusion of atoms from the storage region. Using the decoherence free subspaces [169], the storage times could easily exceed several seconds in such setup.

Successful observations of extinction and EIT from a single ion suggest possible experiments, in which a single ion could act as an efficient switch, polarization rotator or phase shifter of a weak coherent beam or a single photon. Using higher NA lenses, a non-demolition measurement of the ion's motion as proposed in [104] should become feasible. Realization of quantum cascaded systems [170], where fluorescence photons generated by a single ion excite the second ion could provide important insight to the process and statistics of single photon absorption by a single ion.

In the presented thermometry experiment we used a simple ion-mirror setup for estimating the amplitude of an ion's thermal motion from the interference contrast of the emitted fluorescence. By preparing a highly non-classical motional state, for example a cat-state, this setup could be employed to investigate the collapse of the motional wavefunction conditioned on the detection of an emitted fluorescence photon.

On the purely technical side, the degree of control of coherent interactions on the realized qubit transitions could be significantly improved by implementing active magnetic field stabilization at the position of the trap. Furthermore, the slow drift of the optical cavity that stabilizes the 1.76 μm laser could be compensated by locking the frequency of the laser to the ion's transition. These improvements would allow the realization of entanglement using the common motional modes of two ions in the same trap by some of the well known techniques, for example using the Mølmer-Sørensen gate [171]. Such deterministic generation of entanglement could be then employed for testing the proposed estimation of the amount of entanglement based on the measurement of interference contrast of spontaneously scattered photons from the two atoms [161], as described in the section 6.4.1.

Besides these possible experimental proposals, there are a number of exciting physical phenomena which can be conveniently investigated using the knowledge and technological improvements developed in this thesis. These include the measurement of the super/sub-radiance effects between two ions, of the quadrature squeezing of the resonance fluorescence, or of the ion's trajectory in phase space for different motional states.

Journal publications

The work presented in this thesis resulted in number of publications in the field of quantum information processing with single atoms and photons in free space:

- "Atom-atom entanglement by single-photon detection",
  L. Slodička, G. Hétet, N. Röck, P. Schindler, M. Hennrich and R. Blatt, Phys. Rev. Lett. **110**, 083603 (2013)

- "Interferometric thermometry of a single sub-Doppler-cooled atom",
  L. Slodička, G. Hétet, N. Röck, S. Gerber, P. Schindler, M. Kumph, M. Hennrich, and R. Blatt, Phys. Rev. A **85**, 043401 (2012)

- "Single Atom as a Mirror of an Optical Cavity",
  G. Hétet, **L. Slodička**, M. Hennrich, and R. Blatt, Phys. Rev. Lett. **107**, 133002 (2011)

- "Electromagnetically Induced Transparency from a Single Atom in Free Space",
  L. Slodička, G. Hétet, S. Gerber, M. Hennrich, and R. Blatt, Phys. Rev. Lett. **105**, 153604 (2010)

In the framework of this thesis, I contributed also to additional publications concerned with studies of atom-light coupling in a free space, quantum feedback and phase locking of the motion of single atoms and measurements of correlation functions of single atom resonance fluorescence:

- "Faraday rotation of a tightly focussed beam from a single trapped atom",
  G. Hétet, **L. Slodička**, N. Röck and R. Blatt, preprint available on the arXiv server: arXiv:1212.0810

- "Shot-noise limited monitoring and phase locking of the motion of a single trapped ion",
  P. Bushev, G. Hétet, **L. Slodička**, D. Rotter, M. A. Wilson, F. Schmidt-Kaler, J. Eschner and R. Blatt, Phys. Rev. Lett. **110**, 133602 (2013)

- "QED with a spherical mirror",
  G. Hétet, **L. Slodička**, A. Glätzle, M. Hennrich, and R. Blatt, Phys. Rev. A **82**, 063812 (2010)

- "Intensity-Field Correlation of Single-Atom Resonance Fluorescence",
  S. Gerber, D. Rotter, **L. Slodička**, J. Eschner, H. J. Carmichael, and R. Blatt, Phys. Rev. Lett. **102**, 183601, (2009)

Bibliography

[1] R. G. Gould, The LASER, light amplification by stimulated emission of radiation, in *The Ann Arbor Conference on Optical Pumping, the University of Michigan*, volume 15, p. 128, 1959.

[2] T. H. Maiman, *Nature* **187**, 493 (1960).

[3] M. Riordan, L. Hoddeson, and C. Herring, *Rev. of Mod. Phys.* **71**, 336 (1999).

[4] M. A. Nielsen and I. L. Chuang, *Quantum computation and quantum information*, Cambridge University Press, 2010.

[5] T. Monz, K. Kim, W. Hänsel, M. Riebe, A. S. Villar, P. Schindler, M. Chwalla, M. Hennrich, and R. Blatt, *Phys. Rev. Lett.* **102**, 40501 (2009).

[6] B. P. Lanyon, M. Barbieri, M. P. Almeida, T. Jennewein, T. C. Ralph, K. J. Resch, G. J. Pryde, J. L. O'Brien, A. Gilchrist, and A. G. White, *Nat. Phys.* **5**, 134 (2008).

[7] P. Schindler, J. T. Barreiro, T. Monz, V. Nebendahl, D. Nigg, M. Chwalla, M. Hennrich, and R. Blatt, *Science* **332**, 1059 (2011).

[8] X.-C. Yao, T.-X. Wang, H.-Z. Chen, W.-B. Gao, A. G. Fowler, R. Raussendorf, Z.-B. Chen, N.-L. Liu, C.-Y. Lu, Y.-J. Deng, Y.-A. Chen, and J.-W. Pan, *Nature* **482**, 489 (2012).

[9] K. Kim, M.-S. Chang, S. Korenblit, R. Islam, E. Edwards, J. Freericks, G.-D. Lin, L.-M. Duan, and C. Monroe, *Nature* **465**, 590 (2010).

[10] B. Lanyon, C. Hempel, D. Nigg, M. Müller, R. Gerritsma, F. Zähringer, P. Schindler, J. Barreiro, M. Rambach, G. Kirchmair, M. Hennrich, P. Zoller, R. Blatt, and C. F. Roos, *Science* **334**, 57 (2011).

[11] B. Lanyon, T. Weinhold, N. Langford, M. Barbieri, D. James, A. Gilchrist, and A. White, *Phys. Rev. Lett.* **99**, 250505 (2007).

[12] L. M. K. Vandersypen, M. Steffen, G. Breyta, C. S. Yannoni, M. H. Sherwood, and I. L. Chuang, *Nature* **414**, 883 (2001).

[13] I. L. Chuang, N. Gershenfeld, and M. Kubinec, *Phys. Rev. Lett.* **80**, 3408 (1998).

[14] L. DiCarlo, J. Chow, J. Gambetta, L. S. Bishop, B. Johnson, D. Schuster, J. Majer, A. Blais, L. Frunzio, S. Girvin, and R. J. Schoelkopf, *Nature* **460**, 240 (2009).

[15] D. Stucki, N. Walenta, F. Vannel, R. Thew, N. Gisin, H. Zbinden, S. Gray, C. Towery, and S. Ten, *New J. Phys.* **11**, 075003 (2009).

[16] R. Ursin, F. Tiefenbacher, T. Schmitt-Manderbach, H. Weier, T. Scheidl, M. Lindenthal, B. Blauensteiner, T. Jennewein, J. Perdigues, P. Trojek, B. Ömer, M. Fürst, M. Meyenburg, J. Rarity, Z. Sodnik, C. Barbieri, H. Weinfurter, and A. Zeilinger, *Nat. Phys.* **3**, 481 (2007).

[17] L. Jiang, J. M. Taylor, A. S. Sørensen, and M. D. Lukin, *Phys. Rev. A* **76**, 062323 (2007).

[18] J. I. Cirac, A. K. Ekert, S. F. Huelga, and C. Macchiavello, *Phys. Rev. A* **59**, 4249 (1999).

[19] D. Gottesman and I. L. Chuang, *Nature* **402**, 390 (1999).

[20] H.-J. Briegel, W. Dür, J. I. Cirac, and P. Zoller, *Phys. Rev. Lett.* **81**, 5932 (1998).

[21] L. Duan, M. Lukin, I. Cirac, and P. Zoller, *Nature* **414**, 413 (2001).

[22] J. I. Cirac, P. Zoller, H. J. Kimble, and H. Mabuchi, *Phys. Rev. Lett.* **78**, 3221 (1997).

[23] H. J. Kimble, *Nature* **453**, 1023 (2008).

[24] M. Brune, P. Nussenzveig, F. Schmidt-Kaler, F. Bernardot, A. Maali, J. M. Raimond, and S. Haroche, *Phys. Rev. Lett.* **72**, 3339 (1994).

[25] P. W. H. Pinkse, T. Fischer, P. Maunz, and G. Rempe, *Nature* **404**, 365 (2000).

[26] C. J. Hood, T. W. Lynn, A. C. Doherty, A. S. Parkins, and H. J. Kimble, *Science* **287**, 1447 (2000).

[27] B. Julsgaard, J. Sherson, J. Cirac, J. Fiurášek, and E. Polzik, *Nature* **432**, 482 (2004).

[28] L. V. Hau, S. E. Harris, Z. Dutton, and C. H. Behroozi, *Nature* **397**, 594 (1999).

[29] D. Phillips, A. Fleischhauer, A. Mair, R. Walsworth, and M. Lukin, *Phys. Rev. Lett.* **86**, 783 (2001).

[30] Y. R. P. Sortais, H. Marion, C. Tuchendler, A. M. Lance, M. Lamare, P. Fournet, C. Armellin, R. Mercier, G. Messin, A. Browaeys, and P. Grangier, *Phys. Rev. A* **75**, 013406 (2007).

[31] M. Sondermann, R. Maiwald, H. Konermann, N. Lindlein, U. Peschel, and G. Leuchs, *Applied Physics B: Lasers and Optics* **89**, 489 (2007).

[32] M. Tey, Z. Chen, S. Aljunid, B. Chng, F. Huber, G. Maslennikov, and C. Kurtsiefer, *Nat. Phys.* **4**, 924 (2008).

[33] G. Zumofen, N. Mojarad, V. Sandoghdar, and M. Agio, *Phys. Rev. Lett.* **101**, 180404 (2008).

[34] I. Gerhardt, G. Wrigge, P. Bushev, G. Zumofen, M. Agio, R. Pfab, and V. Sandoghdar, *Phys. Rev. Lett.* **98**, 33601 (2007).

[35] G. Wrigge, I. Gerhardt, J. Hwang, G. Zumofen, and V. Sandoghdar, *Nat. Phys.* **4**, 60 (2007).

[36] A. N. Vamivakas, M. Atatüre, J. Dreiser, S. T. Yilmaz, A. Badolato, A. K. Swan, B. B. Goldberg, A. Imamoglu, and M. S. Ünlü, *Nano letters* **7**, 2892 (2007).

[37] C. Cabrillo, J. I. Cirac, P. Garcia-Fernandez, and P. Zoller, *Phys. Rev. A* **59**, 1025 (1999).

[38] C. Simon and W. T. M. Irvine, *Phys. Rev. Lett.* **91**, 110405 (2003).

[39] J. Eschner, C. Raab, F. Schmidt-Kaler, and R. Blatt, *Nature* **413**, 495 (2001).

[40] W. Nagourney, J. Sandberg, and H. Dehmelt, *Phys. Rev. Lett.* **56**, 2797 (1986).

[41] W. Neuhauser, M. Hohenstatt, P. Toschek, and H. Dehmelt, *Phys. Rev. Lett.* **41**, 233 (1978).

[42] W. Neuhauser, M. Hohenstatt, P. E. Toschek, and H. Dehmelt, *Phys. Rev. A* **22**, 1137 (1980).

[43] Y. Ralchenko, F. Jou, D. Kelleher, A. Kramida, A. Musgrove, J. Reader, W. Wiese, and K. Olsen, *NIST Atomic Spectra Database, NIST Standard Reference Database* (2006).

[44] A. Steele, L. Churchill, P. Griffin, and M. Chapman, *Phys. Rev. A* **75**, 053404 (2007).

[45] G. Leschhorn, T. Hasegawa, and T. Schaetz, *Applied Physics B: Lasers and Optics* , 1 (2012).

[46] Y. Lin, S. Williams, and B. Odom, *arXiv:1210.0551* (2012).

[47] N. Lewty, B. Chuah, R. Cazan, and M. Barrett, *arXiv:1205.6908* (2012).

[48] G. Shu, C. K. Chou, N. Kurz, M. Dietrich, and B. Blinov, *JOSA B* **28**, 2865 (2011).

[49] J. Sherman, A. Andalkar, W. Nagourney, and E. Fortson, *Phys. Rev. A* **78**, 052514 (2008).

[50] J. Sherman, W. Trimble, S. Metz, W. Nagourney, and N. Fortson, Progress on indium and barium single ion optical frequency standards, in *LEOS Summer Topical Meetings, 2005 Digest of the*, pp. 99–100, IEEE, 2005.

[51] C. Knab-Bernardini, H. Knab, F. Vedel, and G. Werth, *Zeitschrift für Physik D Atoms, Molecules and Clusters* **24**, 339 (1992).

[52] N. Yu, W. Nagourney, and H. Dehmelt, *Phys. Rev. Lett.* **78**, 4898 (1997).

[53] W. Paul, O. Osberghaus, and W. Fischer, *Ein Ionenkäfig*, Forschungsberichte des Wirtschafts und Verkehrsministeriums Nordrhein-Westfalen 415, Westfälischer Verlag, Opladen, 1958.

[54] P. Ghosh, *Ion traps*, Clarendon press, Oxford, 1995.

[55] D. Leibfried, R. Blatt, C. Monroe, and D. Wineland, *Rev. Mod. Phys.* **75**, 281 (2003).

[56] C. Roos, *Controlling the quantum state of trapped ions*, PhD thesis, Universität Innsbruck, 2000.

[57] D. Rotter, *Quantum feedback and quantum correlation measurements with a single Barium ion*, PhD thesis, Universität Innsbruck, 2008.

[58] J. Bolle, *Spektroskopie und nichtklassische Fluoreszenzeigenschaften von einzelnen gespeicherten Barium-Ionen*, PhD thesis, Universität Innsbruck, 1998.

[59] M. Harlander, *Architecture for a scalable ion-trap quantum computer*, PhD thesis, Universität Innsbruck, 2012.

[60] M. Brownnutt, G. Wilpers, P. Gill, R. Thompson, and A. Sinclair, *New J. Phys.* **8**, 232 (2006).

[61] U. Poschinger, A. Walther, M. Hettrich, F. Ziesel, and F. Schmidt-Kaler, *Applied Physics B: Lasers and Optics* , 1 (2012).

[62] C. Raab, J. Bolle, H. Oberst, J. Eschner, F. Schmidt-Kaler, and R. Blatt, *Applied Physics B: Lasers and Optics* **67**, 683 (1998).

[63] P. Schindler, Frequency synthesis and pulse shaping for quantum information processing with trapped ions, Master's thesis, Universität Innsbruck, 2008.

[64] S. Gerber, D. Rotter, M. Hennrich, R. Blatt, F. Rohde, C. Schuck, M. Almendros, R. Gehr, F. Dubin, and J. Eschner, *New J. Phys.* **11**, 013032 (2009).

[65] S. Gerber, D. Rotter, L. Slodička, J. Eschner, H. J. Carmichael, and R. Blatt, *Phys. Rev. Lett.* **102**, 183601 (2009).

[66] L. Slodička, G. Hétet, N. Röck, S. Gerber, P. Schindler, M. Kumph, M. Hennrich, and R. Blatt, *Phys. Rev. A* **85**, 043401 (2012).

[67] T. Monz, *Quantum information processing beyond ten ion-qubits*, PhD thesis, Universität Innsbruck, 2011.

[68] G. Kirchmair, *Quantum non-demolition measurements and quantum simulation*, PhD thesis, Universität Innsbruck, 2010.

[69] M. Chwalla, *Precision spectroscopy with* $^{40}Ca^{+}$ *ions in a Paul trap*, PhD thesis, Universität Innsbruck, 2009.

[70] M. Riebe, *Preparation of entangled states and quantum teleportation with atomic qubits*, PhD thesis, Universität Innsbruck, 2005.

[71] M. Dietrich, *Barium Ions for Quantum Computation*, PhD thesis, University of Washington, 2009.

[72] M. R. Dietrich, N. Kurz, T. Noel, G. Shu, and B. B. Blinov, *Phys. Rev. A* **81**, 052328 (2010).

[73] D. James, *Applied Physics B: Lasers and Optics* **66**, 181 (1998).

[74] S. Gulde, *Experimental realization of quantum gates and the Deutsch-Josza algorithm with trapped $^{40}Ca^{+}$ ions*, PhD thesis, 2003.

[75] N. Röck, Quantum manipulation on the Barium quadrupolar transition, Master's thesis, Universität Innsbruck, 2011.

[76] T. Sauter, W. Neuhauser, R. Blatt, and P. E. Toschek, *Phys. Rev. Lett.* **57**, 1696 (1986).

[77] J. C. Bergquist, R. G. Hulet, W. M. Itano, and D. J. Wineland, *Phys. Rev. Lett.* **57**, 1699 (1986).

[78] R. Loudon, *The quantum theory of light*, Oxford University Press, USA, 2000.

[79] D. J. Wineland and W. M. Itano, *Phys. Rev. A* **20**, 1521 (1979).

[80] N. Ramsey, *Molecular beams*, Oxford University Press, USA, 1990.

[81] C. Tannoudji, G. Grynberg, and J. Dupont-Roe, *Atom-photon interactions*, New York, NY (United States); John Wiley and Sons Inc., 1992.

[82] S. Nussmann, M. Hijlkema, B. Weber, F. Rohde, G. Rempe, and A. Kuhn, *Phys. Rev. Lett.* **95**, 173602 (2005).

[83] I. Dotsenko, W. Alt, M. Khudaverdyan, S. Kuhr, D. Meschede, Y. Miroshnychenko, D. Schrader, and A. Rauschenbeutel, *Phys. Rev. Lett.* **95**, 033002 (2005).

[84] J. Volz, M. Weber, D. Schlenk, W. Rosenfeld, J. Vrana, K. Saucke, C. Kurtsiefer, and H. Weinfurter, *Phys. Rev. Lett.* **96**, 030404 (2006).

[85] H. G. Barros, A. Stute, T. E. Northup, C. Russo, P. O. Schmidt, and R. Blatt, *New J. Phys.* **11**, 103004 (2009).

[86] N. Piro, F. Rohde, C. Schuck, M. Almendros, J. Huwer, J. Ghosh, A. Haase, M. Hennrich, F. Dubin, and J. Eschner, *Nat. Phys.* **7**, 17 (2011).

[87] L. M. Duan and C. Monroe, *Rev. Mod. Phys.* **82**, 1209 (2010).

[88] A. Ourjoumtsev, A. Kubanek, M. Koch, C. Sames, P. W. H. Pinkse, G. Rempe, and K. Murr, *Nature* **474**, 623 (2011).

[89] B. Darquié, M. Jones, J. Dingjan, J. Beugnon, S. Bergamini, Y. Sortais, G. Messin, A. Browaeys, and P. Grangier, *Science* **309**, 454 (2005).

[90] A. Stute, B. Casabone, P. Schindler, T. Monz, P. Schmidt, B. Brandstätter, T. Northup, and R. Blatt, *Nature* **485**, 482 (2012).

[91] F. Dubin, D. Rotter, M. Mukherjee, C. Russo, J. Eschner, and R. Blatt, *Phys. Rev. Lett.* **98**, 183003 (2007).

[92] M. A. Wilson, P. Bushev, J. Eschner, F. Schmidt-Kaler, C. Becher, R. Blatt, and U. Dorner, *Phys. Rev. Lett.* **91**, 213602 (2003).

[93] G. Hétet, L. Slodička, M. Hennrich, and R. Blatt, *Phys. Rev. Lett.* **107**, 133002 (2011).

[94] N. Daniilidis, S. Narayanan, S. Möller, R. Clark, T. Lee, P. Leek, A. Wallraff, S. Schulz, F. Schmidt-Kaler, and H. Häffner, *New J. Phys.* **13**, 013032 (2011).

[95] R. J. Epstein, S. Seidelin, D. Leibfried, J. H. Wesenberg, J. J. Bollinger, J. M. Amini, R. B. Blakestad, J. Britton, J. P. Home, W. M. Itano, J. D. Jost, E. Knill, C. Langer, R. Ozeri, N. Shiga, and D. J. Wineland, *Phys. Rev. A* **76**, 033411 (2007).

[96] F. Reif and F. Reif, *Fundamentals of statistical and thermal physics*, volume 11, McGraw-Hill New York, 1965.

[97] J. C. Bergquist, W. M. Itano, and D. J. Wineland, *Phys. Rev. A* **36**, 428 (1987).

[98] C. Roos, T. Zeiger, H. Rohde, H. C. Nägerl, J. Eschner, D. Leibfried, F. Schmidt-Kaler, and R. Blatt, *Phys. Rev. Lett.* **83**, 4713 (1999).

[99] W. Nagourney, G. Janik, and H. Dehmelt, *Proceedings of the National Academy of Sciences* **80**, 643 (1983).

[100] M. Herrmann, V. Batteiger, S. Knünz, G. Saathoff, T. Udem, and T. W. Hänsch, *Phys. Rev. Lett.* **102**, 013006 (2009).

[101] S. Knünz, M. Herrmann, V. Batteiger, G. Saathoff, T. W. Hänsch, and T. Udem, *Phys. Rev. A* **85**, 023427 (2012).

[102] B. G. Norton, E. W. Streed, M. J. Petrasiunas, A. Jechow, and D. Kielpinski, *New J. Phys.* **13**, 113022 (2011).

[103] P. Bushev, D. Rotter, A. Wilson, F. Dubin, C. Becher, J. Eschner, R. Blatt, V. Steixner, P. Rabl, and P. Zoller, *Phys. Rev. Lett.* **96**, 43003 (2006).

[104] P. Rabl, V. Steixner, and P. Zoller, *Phys. Rev. A* **72**, 043823 (2005).

[105] Q. A. Turchette, Kielpinski, B. E. King, D. Leibfried, D. M. Meekhof, C. J. Myatt, M. A. Rowe, C. A. Sackett, C. S. Wood, W. M. Itano, C. Monroe, and D. J. Wineland, *Phys. Rev. A* **61**, 063418 (2000).

[106] I. Marzoli, J. I. Cirac, R. Blatt, and P. Zoller, *Phys. Rev. A* **49**, 2771 (1994).

[107] J. I. Cirac, L. J. Garay, R. Blatt, A. S. Parkins, and P. Zoller, *Phys. Rev. A* **49**, 421 (1994).

[108] F. Diedrich, J. C. Bergquist, W. M. Itano, and D. J. Wineland, *Phys. Rev. Lett.* **62**, 403 (1989).

[109] C. Tamm, D. Engelke, and V. Bühner, *Phys. Rev. A* **61**, 053405 (2000).

[110] J. Eschner, *Eur. Phys. J. D* **22**, 341 (2003).

[111] D. J. Berkeland, Miller, J. C. J. D. Bergquist, W. M. Itano, and D. J. Wineland, *J. Appl. Phys.* **83**, 5025 (1998).

[112] S. A. Aljunid, M. K. Tey, B. Chng, T. Liew, G. Maslennikov, V. Scarani, and C. Kurtsiefer, *Phys. Rev. Lett.* **103**, 153601 (2009).

[113] J. Hwang, M. Pototschnig, R. Lettow, G. Zumofen, A. Renn, S. Götzinger, and V. Sandoghdar, *Nature* **460**, 76 (2009).

[114] A. Jechow, B. G. Norton, S. Händel, V. Blūms, E. W. Streed, and D. Kielpinski, *Phys. Rev. Lett.* **110**, 113605 (2013).

[115] H. Häffner, C. Roos, and R. Blatt, *Physics Reports* **469**, 155 (2008).

[116] S. Olmschenk, D. N. Matsukevich, P. Maunz, D. Hayes, L.-M. Duan, and C. Monroe, *Science* **323**, 486 (2009).

[117] M. Fleischhauer, A. Imamoğlu, and J. P. Marangos, *Rev. Mod. Phys.* **77**, 633 (2005).

[118] M. D. Eisaman, A. André, F. Massou, M. Fleischhauer, A. S. Zibrov, and M. D. Lukin, *Nature* **438**, 837 (2005).

[119] K. S. Choi, H. Deng, J. Laurat, and H. Kimble, *Nature* **452**, 67 (2008).

[120] A. D. Boozer, A. Boca, R. Miller, T. E. Northup, and H. J. Kimble, *Phys. Rev. Lett.* **98**, 193601 (2007).

[121] A. Kreuter, C. Becher, G. Lancaster, A. Mundt, C. Russo, H. Häffner, C. Roos, J. Eschner, F. Schmidt-Kaler, and R. Blatt, *Phys. Rev. Lett.* **92**, 203002 (2004).

[122] A. A. Abdumalikov Jr, O. Astafiev, A. M. Zagoskin, Y. A. Pashkin, Y. Nakamura, and J. S. Tsai, *Phys. Rev. Lett.* **104**, 193601 (2010).

[123] L. Slodička, G. Hétet, S. Gerber, M. Hennrich, and R. Blatt, *Phys. Rev. Lett.* **105**, 153604 (2010).

[124] P. Kochan and H. J. Carmichael, *Phys. Rev. A* **50**, 1700 (1994).

[125] M. K. Tey, G. Maslennikov, T. C. H. Liew, S. A. Aljunid, F. Huber, B. Chng, Z. Chen, V. Scarani, and C. Kurtsiefer, *New J. Phys.* **11**, 043011 (2009).

[126] S. J. van Enk, *Phys. Rev. A* **69**, 043813 (2004).

[127] A. Imamoğlu and S. E. Harris, *Opt. Lett.* **14**, 1344 (1989).

[128] K. J. Boller, A. Imamoğlu, and S. E. Harris, *Phys. Rev. Lett.* **66**, 2593 (1991).

[129] S. Heugel, A. Villar, M. Sondermann, U. Peschel, and G. Leuchs, *Laser Physics* **20**, 100 (2010).

[130] U. Dorner and P. Zoller, *Phys. Rev. A* **66**, 023816 (2002).

[131] G. Hétet, L. Slodička, A. Glätzle, M. Hennrich, and R. Blatt, *Phys. Rev. A* **82**, 063812 (2010).

[132] M. Mücke, E. Figueroa, J. Bochmann, C. Hahn, K. Murr, S. Ritter, C. Villas-Boas, and G. Rempe, *Nature* **465**, 755 (2010).

[133] T. Kampschulte, W. Alt, S. Brakhane, M. Eckstein, R. Reimann, A. Widera, and D. Meschede, *Phys. Rev. Lett.* **105**, 153603 (2010).

[134] D. Pinotsi and A. Imamoglu, *Phys. Rev. Lett.* **100**, 093603 (2008).

[135] H. P. Specht, C. Nölleke, A. Reiserer, M. Uphoff, E. Figueroa, S. Ritter, and G. Rempe, *Nature* **473**, 190 (2011).

[136] N. Lindlein, R. Maiwald, H. Konermann, M. Sondermann, U. Peschel, and G. Leuchs, *Laser Physics* **17**, 927 (2007).

[137] M. Stobińska, G. Alber, and G. Leuchs, *Europhysics Letters* **86**, 14007 (2009).

[138] Y. Wang, L. Sheridan, and V. Scarani, *ArXiv e-prints* (2010).

[139] A. Ekert and R. Jozsa, *Philosophical Transactions A* **356**, 1769 (1998).

[140] A. K. Ekert, *Phys. Rev. Lett.* **67**, 661 (1991).

[141] C. H. Bennett, G. Brassard, C. Crépeau, R. Jozsa, A. Peres, and W. K. Wootters, *Phys. Rev. Lett.* **70**, 1895 (1993).

[142] P. W. Shor, *Proceedings of the 35th Annual Symposium on the Foundations of Computer Science* , 124 (1994).

[143] C. Chou, H. De Riedmatten, D. Felinto, S. V. Polyakov, S. J. Van Enk, and H. Kimble, *Nature* **438**, 828 (2005).

[144] C. Chou, J. Laurat, H. Deng, K. Choi, H. De Riedmatten, D. Felinto, and H. Kimble, *Science* **316**, 1316 (2007).

[145] D. L. Moehring, P. Maunz, S. Olmschenk, K. C. Younge, D. N. Matsukevich, L. M. Duan, and C. Monroe, *Nature* **449**, 68 (2007).

[146] S. Zippilli, G. A. Olivares-Rentería, G. Morigi, C. Schuck, F. Rohde, and J. Eschner, *New J. Phys.* **10**, 103003 (2008).

[147] L. Luo, D. Hayes, T. A. Manning, D. N. Matsukevich, P. Maunz, S. Olmschenk, J. D. Sterk, and C. Monroe, *Fortschritte der Physik* **57**, 1133 (2009).

[148] S. Ritter, C. Nölleke, C. Hahn, A. Reiserer, A. Neuzner, M. Uphoff, M. Mücke, E. Figueroa, J. Bochmann, and G. Rempe, *Nature* **484**, 195 (2012).

[149] L. Slodička, G. Hétet, N. Röck, P. Schindler, M. Hennrich, and R. Blatt, *Phys. Rev. Lett.* **110**, 083603 (2013).

[150] E. W. Streed, B. G. Norton, A. Jechow, T. J. Weinhold, and D. Kielpinski, *Phys. Rev. Lett.* **106**, 010502 (2011).

[151] E. Streed, A. Jechow, B. Norton, and D. Kielpinski, *Nat. Commun.* **3**, 933 (2012).

[152] S. Olmschenk, D. Hayes, D. Matsukevich, P. Maunz, D. Moehring, and C. Monroe, *International Journal of Quantum Information* **8**, 337 (2010).

[153] R. Maiwald, D. Leibfried, J. Britton, J. Bergquist, G. Leuchs, and D. Wineland, *Nat. Phys.* **5**, 551 (2009).

[154] S. Rist, J. Eschner, M. Hennrich, and G. Morigi, *Phys. Rev. A* **78**, 013808 (2008).

[155] M. Almendros, J. Huwer, N. Piro, F. Rohde, C. Schuck, M. Hennrich, F. Dubin, and J. Eschner, *Phys. Rev. Lett.* **103**, 213601 (2009).

[156] U. Eichmann, J. C. Bergquist, J. J. Bollinger, J. M. Gilligan, W. M. Itano, D. J. Wineland, and M. G. Raizen, *Phys. Rev. Lett.* **70**, 2359 (1993).

[157] W. M. Itano, J. C. Bergquist, J. J. Bollinger, D. J. Wineland, U. Eichmann, and M. G. Raizen, *Phys. Rev. A* **57**, 4176 (1998).

[158] Z. Hradil, *Phys. Rev. A* **55**, 1561 (1997).

[159] M. Paris and J. Rehacek, *Quantum state estimation*, volume 649, Springer, 2004.

[160] H. Häffner, C. Roos, and R. Blatt, *Physics Reports* **469**, 155 (2008).

[161] M. Jakob and J. Bergou, *Optics Communications* **283**, 827 (2010).

[162] R. Wiegner, J. von Zanthier, and G. S. Agarwal, *Phys. Rev. A* **84**, 023805 (2011).

[163] C. A. Sackett, D. Kielpinski, B. E. King, C. Langer, V. Meyer, C. J. Myatt, M. Rowe, Q. A. Turchette, W. M. Itano, D. J. Wineland, et al., *Nature* **404**, 256 (2000).

[164] M. I. Shirokov, *International Journal of Theoretical Physics* **45**, 141 (2006).

[165] D. Kielpinski, V. Meyer, M. A. Rowe, C. A. Sackett, W. M. Itano, C. Monroe, and D. J. Wineland, *Science* **291**, 1013 (2001).

[166] C. F. Roos, G. P. T. Lancaster, M. Riebe, H. Häffner, W. Hänsel, S. Gulde, C. Becher, J. Eschner, F. Schmidt-Kaler, and R. Blatt, *Phys. Rev. Lett.* **92**, 220402 (2004).

[167] T. Monz, P. Schindler, J. T. Barreiro, M. Chwalla, D. Nigg, W. A. Coish, M. Harlander, W. Hänsel, M. Hennrich, and R. Blatt, *Phys. Rev. Lett.* **106**, 130506 (2011).

[168] K. Predehl, G. Grosche, S. Raupach, S. Droste, O. Terra, J. Alnis, T. Legero, T. Hänsch, T. Udem, R. Holzwarth, et al., *Science* **336**, 441 (2012).

[169] T. Monz, K. Kim, A. S. Villar, P. Schindler, M. Chwalla, M. Riebe, C. F. Roos, H. Häffner, W. Hänsel, M. Hennrich, and R. Blatt, *Phys. Rev. Lett.* **103**, 200503 (2009).

[170] H. J. Carmichael, *Phys. Rev. Lett.* **70**, 2273 (1993).

[171] J. Benhelm, G. Kirchmair, C. Roos, and R. Blatt, *Nat. Phys.* **4**, 463 (2008).

Acknowledgements

First I'd like to thank Rainer Blatt for giving me the opportunity to work in his group and study the experimental quantum optics with trapped ion systems. I am thankful and appreciate his guidance and leadership of our ion-trapping group which allowed me to focus almost exclusively on the work in the lab. He once said:"You can do physics and I'll take care of everything else.", which was completely true. Thank you Rainer!

I thank to my closest college and postdoc Gabriel Hétet for showing me his way of doing things in the lab and for all the help in realizing the presented experiments and writing the papers. I enjoyed working together and our discussions about physics and philosophy a lot!

I'd like to thank Markus Hennrich for his help in solving all kinds of physics problems encountered during my studies and for detailed reading of my thesis. Big thanks to all members of the Barium team, Sebastian Gerber, Daniel Higginbottom and Nadia Röck, for the nice time we've had together in the lab! Thanks also to Andreas Stute for our physics discussions, Muir Kumph and Philipp Schindler for their help with electronics, Tracy Northup and Mike Brownnutt for all English corrections.

I am grateful to my colleagues and teachers from the university in Olomouc, especially to Miroslav Ježek for providing me with a good introduction to quantum optics and Jaromír Fiurášek for his help and for encouraging me to start my PhD studies in Innsbruck.

I thank my parents Peter and Helena for their continuous support and encouragement and my best brother Peter for all beautiful adventures in mountains. I'd like to thank Rita for keeping me nicely distracted, for making the live more fun and for all the wonderful cakes!

I am very grateful to God for everything!